

## Multiscale Extended Finite Element Method for the Simulation of Fractured Geological Formations

Xu, F.

**DOI**

[10.4233/uuid:2b7eca2c-3dbd-48f2-8514-147cab28d1a4](https://doi.org/10.4233/uuid:2b7eca2c-3dbd-48f2-8514-147cab28d1a4)

**Publication date**

2024

**Document Version**

Final published version

**Citation (APA)**

Xu, F. (2024). *Multiscale Extended Finite Element Method for the Simulation of Fractured Geological Formations*. [Dissertation (TU Delft), Delft University of Technology]. <https://doi.org/10.4233/uuid:2b7eca2c-3dbd-48f2-8514-147cab28d1a4>

**Important note**

To cite this publication, please use the final published version (if applicable). Please check the document version above.

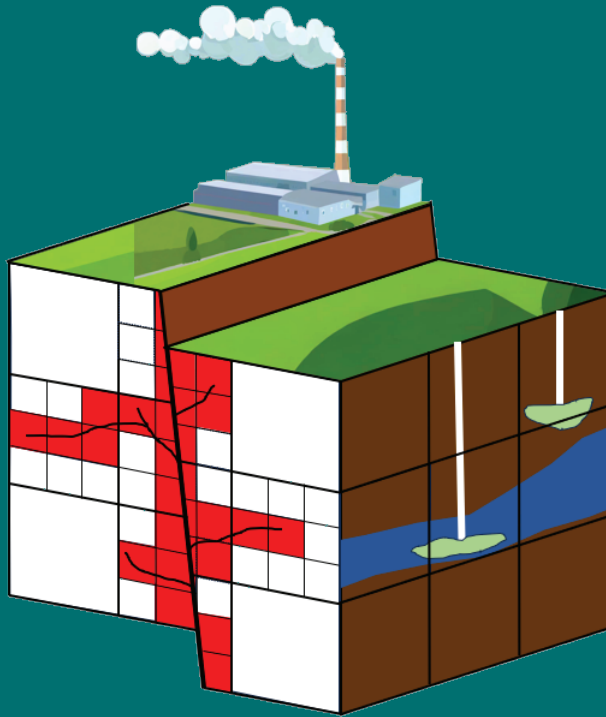
**Copyright**

Other than for strictly personal use, it is not permitted to download, forward or distribute the text or part of it, without the consent of the author(s) and/or copyright holder(s), unless the work is under an open content license such as Creative Commons.

**Takedown policy**

Please contact us and provide details if you believe this document breaches copyrights. We will remove access to the work immediately and investigate your claim.

# Multiscale Extended Finite Element Method for the Simulation of Fractured Geological Formations



Fanxiang Xu 徐凡翔



# MULTISCALE EXTENDED FINITE ELEMENT METHOD FOR THE SIMULATION OF FRACTURED GEOLOGICAL FORMATIONS

## Proefschrift

ter verkrijging van de graad van doctor  
aan de Technische Universiteit Delft,  
op gezag van de Rector Magnificus prof. dr. ir. T.H.J.J. van der Hagen,  
voorzitter van het College voor Promoties,  
in het openbaar te verdedigen op  
woensdag 13 maart 2024 om 15:00 uur

door

**Fanxiang XU**

Master of Science in Applied Earth Science,  
Technische Universiteit Delft, Nederland,  
geboren te Sichuan, China.

Dit proefschrift is goedgekeurd door de promotoren.

Samenstelling promotiecommissie:

Rector Magnificus	voorzitter
Prof. dr. ir. L. J. Sluys	Technische Universiteit Delft, promotor
Prof. dr. ir. H. Hajibeygi	Technische Universiteit Delft, promotor

*Onafhankelijke leden:*

Prof. dr. I. Berre	University of Bergen
Prof. dr. P. J. Vardon	Technische Universiteit Delft
Dr. ir. F. P. van der Meer	Technische Universiteit Delft
Dr. ir. A. Pluymakers	Technische Universiteit Delft
Dr. ir. D. V. Voskov	Technische Universiteit Delft
Prof. dr. S. Geiger	Technische Universiteit Delft, reservelid

This research was carried out within the Delft Advanced Reservoir Simulation group (DARSim) at Delft University of Technology and sponsored by the Chinese Scholarship Council (CSC). We also appreciate Energi Simulation support.



**DARSim**  
Delft Advanced Reservoir Simulation

**energi**  
SIMULATION

*Keywords:* multiscale extended finite element method, geological fractured formation, fractures propagation, deformation of fractured formation  
*Printed by:* Ipskamp printing  
*Front & Back:* Fanxiang Xu

Copyright © 2024, F. Xu ([peterxu1994@gmail.com](mailto:peterxu1994@gmail.com))

ISBN 978-94-6366-827-9

An electronic version of this dissertation is available at  
<http://repository.tudelft.nl/>.

*We can only see a short distance ahead,  
but we can see plenty there that needs to be done.*

Alan Turing

To my mom, dad, sister, brother, niece and my love



# CONTENTS

<b>Preface</b>	<b>vii</b>
<b>Acknowledgements</b>	<b>ix</b>
<b>Summary</b>	<b>xiii</b>
<b>Samenvatting</b>	<b>xv</b>
<b>1 Introduction</b>	<b>1</b>
1.1 Challenges . . . . .	2
1.2 Simulation Methods . . . . .	4
1.3 Research goals . . . . .	5
1.4 Thesis outline . . . . .	6
<b>2 Simulation of Fractured Media at Fine Scale using XFEM Methodologies</b>	<b>7</b>
2.1 Governing Equations . . . . .	7
2.2 Extended Finite Element Method . . . . .	9
2.2.1 Jump enrichment . . . . .	9
2.2.2 Tip Enrichment . . . . .	9
2.2.3 Junction enrichment . . . . .	12
2.2.4 XFEM linear system . . . . .	14
2.3 Fracture Propagation . . . . .	15
2.3.1 Propagation Criterion . . . . .	15
2.4 Level Set Functions . . . . .	17
2.4.1 level set fine-scales for enrichment . . . . .	18
2.4.2 Level Set fine-scales for Fractures Propagation . . . . .	18
2.5 Penalty Method for Compression Fractures . . . . .	20
2.5.1 Contact Law . . . . .	20
2.5.2 Penalty method . . . . .	21
2.5.3 Linear System . . . . .	22
2.6 Conclusions . . . . .	23
<b>3 Multiscale Extended Finite Element Method (MS-XFEM)</b>	<b>25</b>
3.1 Multiscale Simulation Strategy . . . . .	25
3.2 Construction of basis functions for MS-XFEM . . . . .	27
3.3 Algebraic Construction of Basis Functions . . . . .	28
3.4 Iterative strategy . . . . .	30
3.5 Test Cases . . . . .	31
3.5.1 Test case 1: Single fracture in a heterogeneous domain . . . . .	31
3.5.2 Test case 2: heterogeneous reservoir with multiple fractures . . . . .	35
3.5.3 Computational efficiency analysis . . . . .	38

3.6	Conclusions . . . . .	42
<b>4</b>	<b>MS-XFEM for fracture propagation</b>	<b>43</b>
4.1	MS-XFEM on fracture propagation . . . . .	43
4.2	Numerical Test Cases . . . . .	45
4.2.1	Test case 1: homogeneous sandstone with single fracture . . . . .	45
4.2.2	Test case 2: homogeneous sandstone with multiple fractures . . . . .	48
4.3	Conclusion . . . . .	50
<b>5</b>	<b>MS-XFEM for deformation under compression forces</b>	<b>53</b>
5.1	MS-XFEM basis functions for compressive forces . . . . .	53
5.2	MS-XFEM algorithm for compressive forces . . . . .	54
5.3	Test Cases . . . . .	54
5.3.1	Test 1: Edge inclined crack slip . . . . .	54
5.3.2	Test 2: Single inclined crack slip . . . . .	56
5.3.3	Test 3: Multiple crossed cracks slip . . . . .	59
5.3.4	Test 4: Fracture network of heterogeneous formation under compression . . . . .	64
5.4	Conclusions . . . . .	67
<b>6</b>	<b>MS-XFEM for Simulating Mixed-Mode Fracture Propagation</b>	<b>69</b>
6.1	Mixed Mode Fractures Propagation . . . . .	69
6.1.1	Challenges of kinked crack growing paths . . . . .	70
6.1.2	Principles of mixed mode fractures propagation . . . . .	71
6.2	Algorithm for applying MS-XFEM . . . . .	71
6.3	Test Cases . . . . .	71
6.3.1	Wing Crack Propagation in Uni-axial Compression . . . . .	72
6.3.2	Multiple Fractures Propagation under Compression . . . . .	74
6.3.3	Fractures propagation due to lateral traction forces . . . . .	77
6.4	Conclusion . . . . .	81
<b>7</b>	<b>Concluding remarks and future perspectives</b>	<b>83</b>
7.1	MS-XFEM for the simulation of fractures under tensile loading . . . . .	83
7.2	MS-XFEM for the simulation of fractures under compressive loading . . . . .	85
7.3	Future Perspectives . . . . .	86
	<b>References</b>	<b>89</b>
	<b>Curriculum Vitæ</b>	<b>99</b>
	<b>List of Publications</b>	<b>101</b>

# PREFACE

Dear reader,

Perhaps you have stumbled upon this thesis book seeking answers to your own questions or maybe you have chanced upon it randomly, finding intrigue in its contents. Regardless, please accept my gratitude for your presence. To you, this thesis book encapsulates my endeavors as small drops added to the vast ocean of science. Yet, for me, it represents a cinematic snippet of a fraction of my life.

Upon completing my master's studies at Delft University of Technology in the Netherlands, the small local-time stepping model I have achieved inspired me to a PhD in the field of simulations. I found support from my master's thesis advisor, now my PhD mentor, Prof. Hadi Hajibeygi. Under his guidance, I was introduced to Prof. Bert Sluys, who was kind enough to oversee my doctoral journey after assessing my master's thesis. The subsequent sequence of events appeared seamless – securing a scholarship, defending my master's thesis, and embarking on this new PhD odyssey.

In the realm of PhD life, I became more connected to this beautiful city Delft. I resided in the heart of the city, mere steps away from the Nieuwe Kerk. Days commenced with the melodies of church bells and nights were embraced by the city's unique blend of tranquility and vibrancy. Delft, with its nuanced rhythm, proved an ideal haven for harmonizing work and life.

During my PhD years, I had the opportunity to travel to various places. It was a chance for me to see the wonderful artworks and sights that I had only read about in books or seen in movies. Notably, I traversed esteemed destinations such as the Van Gogh museum, the Uffizi gallery and the Eiffel Tower etc. These places revealed to me the vibrant and diverse culture of Europe. Most importantly, these travel experiences added depth to my life.

Reflecting on these five PhD years, the lessons I have gathered extend far beyond academic accomplishments. Life flows unceasingly forward, yet memories remain our cherished companions. Armed with the achievements I have made in academia and the vibrant memories I have collected, I'm prepared for the next chapter of my journey.

*Fanxiang Xu  
Delft, Sep 2023*



# ACKNOWLEDGEMENTS

Completing a challenging PhD journey has been made possible with the help of numerous individuals. I would like to take this moment to express my heartfelt appreciation to all those who have supported me along the way.

I want to start by thanking my supervisor, Prof. Hadi Hajibeygi, from the bottom of my heart. It has been an incredible honor to work with you. Back in my master's years, your reservoir simulation course was truly inspiring. I loved working on those small projects involving fluid flow simulation, and they ignited my passion for numerical simulation. I'm so grateful for the chance you gave me to become your PhD student. During my PhD journey, your guidance and advice were like a guiding light, helping me tackle numerous challenges. Besides your mentorship, you generously provided me with essential hardware, including a high-end laptop, which made completing this thesis project a lot easier. You've been an exceptional mentor, always reminding me how to excel as a professional academic researcher. Thank you very much, Hadi.

Next, I want to express my deep gratitude to my supervisor, Prof. Bert Sluys. I am truly appreciative that you interviewed me and accepted me into the computational mechanics group, even though I had limited knowledge of mechanics at the time. The first day of my PhD, when you introduced me to the world of XFEM, was a pivotal moment that opened the door to my five-year PhD journey. Your willingness to patiently address my basic questions about FEM and your consistent guidance through challenging moments were of immense importance. Above all, I have learned from you the importance of treating everyone with kindness and respect, even amidst your busy schedule. I hope to embody these qualities in my future endeavors. Thank you very much, Bert.

I extend my sincere appreciation to the dedicated staff of the 3mD department: Iris, Jacqueline, Sandra and Jaap. Your kind and professional support played an instrumental role in my journey towards attaining this PhD title. Despite the challenging circumstances of the COVID lock down during my PhD years, your unwavering assistance allowed me to maintain my work from home. I am truly grateful for the annual 3mD summer and winter events, which have left lasting impressions on my heart. Thank you all.

I want to express sincere appreciation to Dr. Nicola Castelletto, Dr. Frans van der Meer, Prof. Kees Vuik, Prof. Giovanni Bertotti, Prof. Nicolas Moës and Prof. Carlos Armando. Dr. Nicola Castelletto, thank you for your assistance during the challenging times when I encountered issues with preconditioned GMRES. Your guidance was pivotal in helping me achieve the desired level of accuracy in this thesis. I want to thank Dr. Frans van der Meer for your assistance when I encountered challenges in implementing stress intensity factor computations within my codes. Then I would like to thank Prof. Kees Vuik for your insightful ideas and recommended research papers when I faced difficulties with convergence. Also, I would like to extend my gratitude to Prof. Giovanni Bertotti for your illuminating explanations on the formation of subsurface fracture networks. Lastly, I would like to acknowledge Prof. Nicolas Moës and Prof. Carlos Armando Duarte for their

enlightening discussions during CFRAC 2023 conference. Your extensive experience in embedded methods has deepened my understanding of oscillations along fracture surfaces, a critical aspect of my research. Thank you all for your suggestions and help.

I would like to seize this moment to express my heartfelt gratitude to my esteemed friends and fellow graduates, Dr. Yaolu Liu, Dr. Kai Li, Dr. Matteo Cusini, Dr. Xiacong Lyu, Dr. Langzi Chang, Dr. Jinyu Tang, Dr. Matei Tene, Dr. Mousa Hosseinimehr, Dr. Yang Wang, Dr. Jiakun Gong, Dr. Mengmeng Gao, Dr. Yi Xia, Dr. Xi Li, Dr. Chenjie Yu, and Dr. Guanguan Yu. At the beginning of my project, I often turned to each of you with what might have seemed like trivial questions such as how to implement this in FEM or how to apply reimbursement, and you graciously and patiently assisted me in resolving numerous challenges. Furthermore, I've gleaned invaluable lessons from your successful PhD journeys. Thank you all for your enduring assistance and the wisdom you've shared.

I want to convey my gratitude to my valued colleagues within the ADMIRE group, Dr. Kishan Ramesh Kumar, Ziliang Zhang, Mengjie Zhao, Willemijn van Rooijen, Dr. Leila Hashemi, Sara Shokrollahzadeh Behbahani, Dr. Yuhang Wang, Dr. Thejas Hulikal Chakrapani, Dr. Artur Castiel Reis de Souza, Dr. Herminio Tasinafo Honorio and Dr. Maartje Boon. Our weekly ADMIRE meetings and the occasional coffee breaks that ensued have been cherished moments. I deeply value the camaraderie we've shared during these gatherings and our journeys to conferences. Thank you all.

Special thanks go to my esteemed colleagues in the Computational Mechanics group: Debashis Wadadar, Nora Kovacs, Dragan Kovacevic, Sijmen Zwarts, Pieter Hofman, Suman Bhattarai, Xinrui Zhang, Lu Ke, Zhe Han, Marina Alves Maia, Joep Storm, Anne Poot, Leon Riccius, Til Gärtner, Dr. Amir Feyezioghani, Dr. Martin Lesueur, Dr. Iuri Rocha, and Dr. Rafid Al-Khoury. While I had the opportunity to get to know some of you only after the onset of the COVID pandemic, I have greatly enjoyed being part of this exceptional team. The enlightening presentations during our CM meetings have been a source of inspiration and intellectual stimulation. I'd like to extend a special thank you to Sijmen Zwarts for your kind assistance in translating my thesis summary and propositions into Dutch, meticulously refining every detail. Thank you all for creating a welcoming and inspiring team atmosphere.

I extend my sincere gratitude to numerous friends who have been an integral part of my journey: Dr. Ze Chang, Dr. Lu Cheng, Dr. Pei He, Dr. Lubin Huo, Pascal Schopping, Xin Liu, Yucheng Liao, Xiuli Wang, Xuhui Liang, Xiaohui Liang, Dr. Bo Li, Chi Jin, Zheng Li, Feng Ma, Rong Yu, Simo Lu, Jian Zheng, Rui Yan, Yuxuan Feng, Shihao Fu and Yubao Zhou. Over these five years, your presence has been the vibrant hue that has illuminated this journey. The shared meals and convivial evenings, often accompanied by good dishes and beer, have given me countless cherished memories. Our enjoyable times together provided a refuge from the stresses of this expedition and will forever hold a special place in my heart. Your unwavering support has been incredibly precious, and I deeply appreciate all that you have done. Thank you all.

Dongyang, my love, whose love has been my ultimate source of strength, guiding me through the challenges of my PhD journey. Just one month before embarking on my PhD in Delft, I had the incredible fortune of meeting you. Although the constraints of my academic pursuit kept me physically apart from you throughout these years, our daily video calls and the precious moments we spent together bridged the distance. Without your

love and support, this PhD journey would have been a desolate and bitter one. I also want to take this opportunity to express my gratitude to our cat, Fei Liu, who added joy to our lives. Thank you, my love, for being my pillar of strength. This achievement is as much yours as it is mine.

Finally, I want to share my deepest gratitude to my family members: my father, mother, brother-in-law, elder sister, and my adorable young niece. Your unwavering support, encouragement, and invaluable suggestions have been the cornerstone of my journey through the rigors of my PhD. To my dad and mom, I owe my very existence and the achievements I stand upon today. Your love have equipped me with the resilience to confront and overcome every challenge in my life. To my sister, brother, and my adorable young niece, your care and guidance have been a guiding light during my PhD years, and your love will forever hold a cherished place in my heart. As I embarked on this academic journey, separated by miles and limited time together, I always felt the warmth of your love surrounding me. To all my beloved family members, thank you for your enduring love and unwavering support.

Fanxiang Xu  
Sep 07, 2023. Delft



# SUMMARY

In the prevailing context of the 21st century, characterized by a predominant reliance on oil and gas, or in the promising future where green energy shapes a human society committed to net-zero emissions, the role of underground fractured formations in energy production and storage remains pivotal and irreplaceable. Geological faults typically act as non-permeable sealing boundaries for reservoirs used in storage, including those for hydrogen and carbon dioxide. In contrast, artificial fractures can serve as highly permeable conduits for fluid flow into wellbores, particularly in applications such as enhanced geothermal reservoirs. In the past decade, the hazardous consequences of failing to predict the geomechanics behaviors of fractured formations have led to a pronounced focus on developing simulation strategies that are both accurate and efficient for fractured formations.

It is challenging to understand formations riddled with fractures. From a computational perspective, the complex fracture networks typically demand a way finer unstructured grid. However, using such an unstructured grid is impractical for real-world applications due to their high computational load. Conversely, coarser grids paired with strategies such as homogenization could result in loss of crucial details. Heterogeneous properties of geological formations that span on large length sizes require the simulation strategies to be scalable, in order to be relevant.

This thesis proposes a novel approach named as multiscale extended finite element method (MS-XFEM) to tackle these challenges. The challenges related to discretization are resolved by applying the extended finite element method (XFEM) which allows for the use of structured grids. This simplified mesh, however, leads to an augmented matrix size due to extra degrees of freedom (DOFs) introduced by enrichments. A multiscale approach is therefore combined with XFEM. The computational process is operated on the larger yet sparser coarse grids and then the coarse scale mesh solutions are interpolated back to fine scale mesh. The novelty of this work is to involve the fractures into basis functions only, thus the coarse scale system is constructed based on a finite element method. More importantly, this construction of basis functions is fully algebraic and can be updated locally and adaptively for the simulation of propagating fractures.

This method has been implemented and tested to prove its efficiency and accuracy. All tests results prove the good qualities of solutions computed from MS-XFEM when compared to fine scale XFEM solutions. Basis functions are constructed successfully with the algebraic method. These tests reveal the potential of the MS-XFEM in simulating real-world subsurface fractured formations.



# SAMENVATTING

In de context van de 21e eeuw, die gekenmerkt wordt door een grote afhankelijkheid van olie en gas, maar ook uitdagingen geeft voor een toekomst waarin groene energie de samenleving helpt om een uitstootvrij bestaan te realiseren, blijft de rol van ondergrondse gefragmenteerde formaties voor energieproductie en opslag cruciaal. Geologische breuken fungeren als niet-doorlaatbare afsluitingen voor reservoirs gebruikt voor opslag van bijvoorbeeld waterstof en kooldioxide. Daarentegen, kunstmatige breuken kunnen juist dienen als zeer doorlaatbare doorgangen voor vloeistofstroming naar boorputten, in het bijzonder voor toepassingen zoals in geothermische reservoirs. Vanwege de grote risico's van het niet kunnen voorspellen van het geomechanische (bezwijk)gedrag, is er in de afgelopen decennia een focus ontstaan op het ontwikkelen van simulatiestrategieën die zowel accuraat als efficiënt zijn voor dergelijke formaties.

Het begrijpen van formaties vol met breuken geeft aanzienlijke uitdagingen. Vanuit een numeriek perspectief vereisen de gecompliceerde breuknetwerken een zeer fijn ongestructureerd grid. Echter, gebruik van zo'n fijn grid is onpraktisch voor realistische toepassingen vanwege de benodigde rekentijd. Daarentegen kan een grover grid in combinatie met strategieën zoals homogenisatie leiden tot verlies van belangrijke details. Heterogene eigenschappen van geologische formaties die zich uitstrekken over grote lengtes vereisen dat de simulatiestrategie schaalbaar is.

Dit proefschrift introduceert een nieuwe aanpak, genaamd de "multiscale extended finite element method" (MS-XFEM), om deze uitdagingen aan te pakken. De uitdagingen gerelateerd aan de discretisatie worden opgelost door de "extended finite element method" (XFEM) toe te passen, die het gebruik van conventionele gestructureerde grids mogelijk maakt. Dit vereenvoudigde grid leidt tot een vergrote matrix als gevolg van extra vrijheidsgraden. Daarom wordt vervolgens een multi-schaal aanpak gecombineerd met XFEM. Het berekeningsproces wordt uitgevoerd op het grotere, maar minder gedetailleerde grid, waarvan de oplossingen worden geïnterpoleerd naar het fijnere grid. De innovatie van dit werk zit in de omschrijving van de scheuren in de basisfuncties, waardoor het grove grid systeem een standaard eindig elementensysteem wordt. Belangrijk is dat de constructie van de basisfuncties volledig algebraïsch is en lokaal kan worden bijgewerkt voor de simulatie van scheurgroei.

De methode is geïmplementeerd en getest om de efficiëntie en nauwkeurigheid aan te tonen. Alle testresultaten bewijzen de goede kwaliteit van oplossingen die zijn berekend met MS-XFEM in vergelijking met oplossingen van de fijne grid XFEM-simulaties. De basisfuncties zijn met succes geconstrueerd met een algebraïsche methode. De testen onderschrijven het potentieel van de MS-XFEM aanpak bij het simuleren van ondergrondse gefragmenteerde formaties in de praktijk.



# 1

## INTRODUCTION

Subsurface fractured formations continue to hold a central position as both the predominant energy source and the primary repository for sequestering carbon dioxide emissions, essential for the realization of a net-zero carbon dioxide emission society. The increasing utilization of renewable energy sources, or at the very least, low-carbon energy alternatives, has been a topic of extensive discourse in recent years. However, underground energy reservoirs, particularly oil and gas, continue to serve as primary energy sources, fueling industries and global transportation networks. According to data from the International Energy Agency (IEA), underground reservoirs held oil and gas accounting for a significant 54.1 % of the world's primary energy supply in 2019, as shown in Fig. 1.1 [1]. While hydrogen currently does not constitute a significant portion of the global energy supply, it nevertheless maintains its status as a notable and promising energy resource for the future. Researchers are directing their efforts towards the storage of hydrogen resources within subterranean porous formation [2–7]. Hydrogen is injected into artificially created underground salt caverns or depleted oil and gas reservoirs for storage. Furthermore, extensive research efforts have been dedicated to the storage of emitted carbon dioxide within underground formations, advancing the pursuit of a society characterized by net-zero carbon dioxide emissions [8–11]. Hence, it is imperative to undertake a comprehensive study and simulate subsurface formations.

Fractures within reservoir formations offer advantages, yet they also introduce inherent risks. Fractures serve as either non-permeable boundaries or highly permeable conduits. They can act as seals for storage reservoir boundaries or facilitate the transportation of fluids, such as oil and gas, towards production wellbores [12]. However, despite their benefits, operations such as injection and production on fractured formations can entail disastrous consequences. The equilibrium state of the stress within fractured geological structures can be disrupted by abrupt changes in the stress field, which can arise from anthropological operations. This can result in the activation, sliding, or propagation of fractures [13–15]. The significant sliding movement along the fracture surfaces can be catastrophic, as it may cause induced earthquakes and impose high risks to the safety of the residents and surface infrastructure, as shown in Fig. 1.2 [16–18]. To mit-

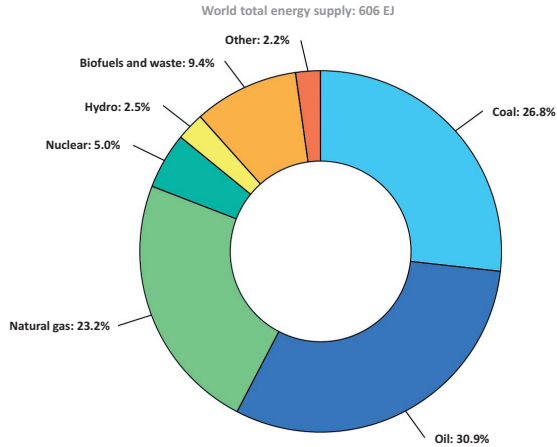


Figure 1.1: Global share of total energy supply by source in 2021. This figure is retrieved from [1].

igate these hazards, the accurate and efficient simulation of evolving fractures within subsurface formations is of paramount importance.



Figure 1.2: A house destroyed due to surface subsidence in Groningen. This figure is retrieved from [19].

## 1.1. CHALLENGES

Substantial challenges persist in the simulation of fractured formations. Heterogeneity of the formation properties (e.g. elasticity coefficients) can span several orders of magnitude. This heterogeneity is prominent at fine-scale (centimeter) resolutions, whereas the reservoirs extend over much larger scales, on the order of kilometers. Classical numerical schemes become too slow to be applied to these systems on the very fine scale level. Upscaling or homogenization is usually effective for the simulation of heterogeneous geological formation [20–27]. However, this simplification leads to the loss of important details, which in turn can lead to significant errors in the final simulation results

and operational conditions design. For example, as depicted in Fig. 1.3(a), a result derived from upscaled permeability fields exhibit loss of intricate features, a predicament elegantly addressed by scalable methodologies like the multiscale approach illustrated in Fig. 1.3(b). The final solution depicted in Fig. 1.3(b) is attained by computing the solution on the coarse mesh, identical to the one shown in Fig. 1.3(a). Subsequently, it is interpolated back to the fine-scale mesh where the heterogeneity map, as depicted in Fig. 1.3(b), is defined. As a result, the multiscale method provides more detailed insights into the heterogeneities. The multiscale method can preserve the heterogeneity of a fractured medium without compromising the accuracy of the simulations, while computing the system generated on the coarser mesh efficiently [28–35]. Thus, it is therefore necessary to develop scalable simulation methods for subsurface underground formations.

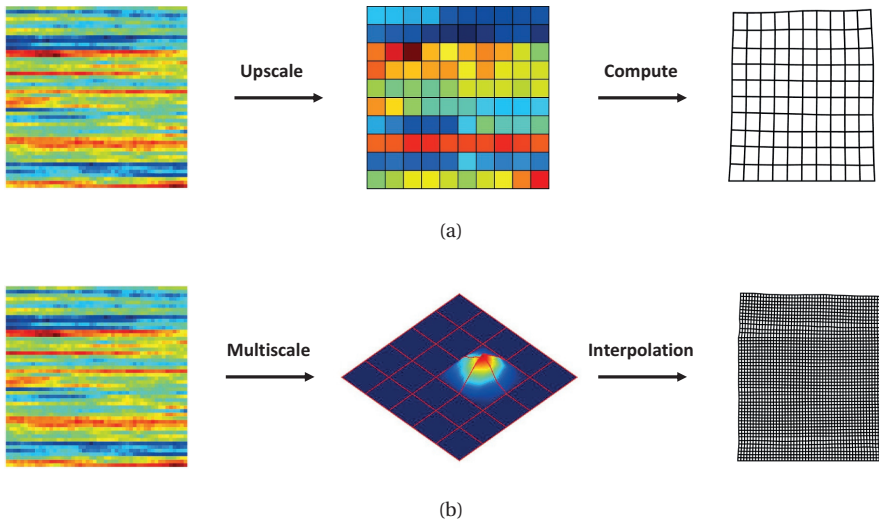


Figure 1.3: Comparison between displacement solutions obtained by (a) upscaling the Young's modulus field and by (b) using the multiscale method (MS).

In addition to the notable heterogeneity of formations, the presence of extensive fractures introduces further complexities to simulation. These fractures introduce discontinuities in mechanical behavior. Research efforts have extensively explored upscaling or homogenization methods concerning the deformation of fractured media [36, 37]. However, these methodologies fall short in capturing details such as severe high stress around fracture tips or dynamic propagation of fractures.

The presence of fractures within computational domains can be treated explicitly by two approaches, namely (1) unstructured grids and (2) immersed or embedded methods. The unstructured grid approach establishes a discrete computational framework where fractures consistently align with element interfaces [38–44]. This allows for convenient treatment of the fractures, however, at the cost of complex mesh geometries. Very fine unstructured meshes are often employed in proximity to fractures to achieve accuracy

but this results in a heavy computational load due to the large size of the resulting linear and nonlinear system of equations. The task of generating complex meshes for three-dimensional (3D) large-scale domains housing multiple fractures further exacerbates this challenge. Additionally, the unstructured grids require updates to accommodate the propagation of fractures, leading to remeshing and the associated computational expense [45, 46]. On the other hand, the embedded approach permits the independent deployment of grids for matrix blocks and fractures. This is achieved by introducing enrichment of the discrete connectivity (for flow) and shape functions (for mechanics) [47–55]. Consequently, the embedded method emerges as a valuable tool to effectively manage intricate subsurface fracture networks.

## 1.2. SIMULATION METHODS

The extended finite element method, or XFEM, is developed to tackle the challenge of complex meshes for subsurface fracture networks. In an embedded method, XFEM enriches the partition of unity (PoU) by introducing extra degrees of freedom (DOFs) at the existing element nodes [56–58]. This permits the application of standard structured grids even within highly complex fractured formations, as shown in Fig. 1.4. There exists sets of enriched functions to capture the different types of discontinuities in the final displacement fields [59–65]. To model the propagation of fractures, level set functions are effectively employed [66, 67]. It is important to note, however, that while this approach mitigates the challenges of complex mesh generation, the large number of extra DOFs stemming from the extensive fracture networks still results in a computational load that is prohibitively high for practical implementation.

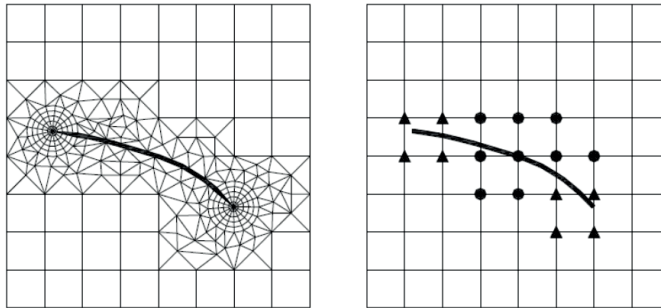


Figure 1.4: (a) unstructured grids used by FEM and (b) structured grids used by XFEM. The triangular and circle markers on (b) represent the enriched mesh nodes. This figure is retrieved from [45].

A multiscale strategy is developed in this thesis to tackle the challenge presented by the existence of highly heterogeneous properties with a high resolution within large-scale formations. Additionally, this multiscale strategy can also resolve the challenge of a large number extra DOFs of XFEM when simulating fractured formations. Within the computational geoscience community, considerable progress has been achieved in the development of multiscale finite element methods (MS-FEM) and multiscale finite volume methods (MS-FVM) [28, 29, 68–76]. The approach proposed by [31] involves con-

structuring basis functions through the approximation of the reduced equilibrium equation along the boundaries of the coarse-scale mesh. However, this work does not address fractured subsurface formations. In presence of fractures that span over different length scales, the adaptive local projection method is recently developed [77, 78]. This method requires the coarse scale mesh solution as the boundary condition to simulate the micro-scale cracks DOFs on a finer scale mesh.

The development of a robust multiscale strategy for deformation of heavily fractured formation, which also allows for convergent systematic error reduction, is of high interest in the geoscience community. In the context of this thesis, a novel multiscale extended finite element method (MS-XFEM) is introduced, providing a promising efficient and scalable approach to simulate highly fractured formations. The MS-XFEM superimposes a coarse mesh onto a given fine-scale mesh. The main idea behind MS-XFEM is to use XFEM to computationally solve for local coarse-scale (multiscale) basis functions. These enriched basis functions should capture fractures and coefficient heterogeneities within coarse elements. The solving strategy of these local coarse-scale basis functions is algebraic as it allows for black-box integration of the method within any existing XFEM simulator. Once the basis functions are solved, they will be clustered in the prolongation matrix  $P$ , which maps the coarse-scale solution to the fine-scale one. Note that there will be no additional multiscale basis functions for fractures and that only 4 multiscale basis functions per element exist for 2D structured grids (8 in 3D) in each direction ( $x$ ,  $y$ , and  $z$ ).

Central to this MS-XFEM approach are its foundational basis functions. Their construction is achieved entirely through algebraic operations on the fine-scale stiffness matrix. The basis functions should be able to capture different types of discontinuities under mixed mode loading involving tension and compression. When fracture propagation occurs, the basis functions can be algebraically updated, relying on the revised fine-scale stiffness matrix. This updated set of basis functions is equally adept at accurately representing extended discontinuities.

The fine scale XFEM system is then mapped to the coarse grid by using the restriction  $R$  matrix, which is defined based on the FEM, as the transpose of basis function matrix  $P$ . The approximate fine-scale solution is finally obtained after mapping the coarse-scale solution to the fine scale grid, by using prolongation matrix  $P$ . This approximate solution is found acceptable, however error control and reduction to any desired level is necessary especially for fracture propagation simulation. As such, the MS-XFEM is integrated within the two-stage iterative solver or paired with preconditioned GMRES [79]. In either of the two strategies, an efficient iterative smoother  $ILLU(0)$  is required to reduce the high frequency errors [80].

### 1.3. RESEARCH GOALS

The main objective of this thesis is to

*Develop an accurate and efficient multiscale extended finite element method framework for simulating the mechanics of subsurface fractured formations.*

To achieve these objectives, the following goals have been achieved:

- Develop a MS-XFEM framework that computes the deformation system on coarse scale grids and interpolates the coarse scale solution back to the fine scale resolution.
- Develop an algebraic method to construct and update basis functions.
- Apply this framework for the simulation of mechanical deformation and fractures propagation in compressed subsurface geological formations.

## 1.4. THESIS OUTLINE

This thesis comprehensively encapsulates the full spectrum of academic accomplishments attained during the course of the PhD program. Chapter 2 presents the governing equations and the extended finite element method, alongside the incorporation of the principles of fracture propagation and the penalty method. Subsequently, in Chapter 3, the basic framework of MS-XFEM is presented with all the necessary details. Test cases are presented to prove the applicability of MS-XFEM for simulating deformation under tensile loading, followed by a thorough investigation of its efficiency and scalability. In Chapter 4, MS-XFEM is extended to simulate fracture propagation under tensile loading. Update of basis functions is explained and shown with two test cases. In Chapter 5, the simulation of static deformation in fractured formations subjected to compressive loading is executed using MS-XFEM. Finally, Chapter 6 explores fracture propagation under mixed-mode loading conditions, closely reflecting real-world scenarios in subsurface formations, enabled by the application of MS-XFEM.

# 2

## SIMULATION OF FRACTURED MEDIA AT FINE SCALE USING XFEM METHODOLOGIES

This chapter serves as an exposition of fundamental theories and principles essential for simulating fractures' contact and slip through the fine-scale extended finite element method. These foundational concepts will subsequently underpin the development of the MS-XFEM. Various types of enrichment functions are systematically introduced, offering a comprehensive understanding of their roles. Furthermore, the chapter elucidates the crucial principles pertaining to fractures' propagation and the application of level set functions in effectively tracking the fractures propagation. Finally, the chapter delves into a detailed description of the penalty method, commonly employed to simulate fractures' contact and frictional slip, thereby providing a robust theoretical foundation for subsequent analyses in the following chapters.

### 2.1. GOVERNING EQUATIONS

Consider the domain  $\Omega$  bounded by  $\Gamma$  as shown in Fig. 2.1. Prescribed displacements  $\bar{u}$  are imposed on  $\Gamma_u$ , while tractions  $\bar{t}$  are imposed on  $\Gamma_t$ . The crack surface  $\Gamma_c$  (lines in 2-D and surfaces in 3-D) is assumed to be traction-free under tensile stress but with contact force  $f_c$  under compressive loading.

The stress equilibrium equations and boundary conditions read as follows

$$\nabla \cdot \sigma + f = 0 \quad \text{in } \Omega, \quad (2.1)$$

$$\sigma \cdot n = \bar{t} \quad \text{on } \Gamma_t, \quad (2.2)$$

$$\sigma \cdot n = f_c \quad \text{on } \Gamma_c, \quad (2.3)$$

$$d = \bar{u} \quad \text{on } \Gamma_u, \quad (2.4)$$

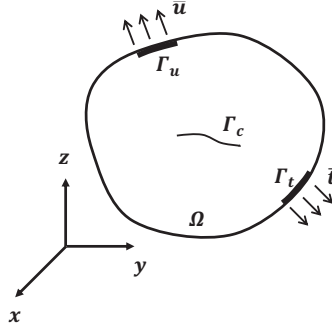


Figure 2.1: An illustration of a fractured domain.

where  $\sigma$  is the stress tensor and  $d$  is the displacement field over the whole domain. Prescribed loads are applied along boundary  $\Gamma_t$  while the prescribed displacements are on  $\Gamma_u$ .  $\vec{n}$  is the normal vector pointing outside the domain boundary. When there is no contact force or cohesive force between the fracture surfaces  $\Gamma_c$ , the value of  $f_c$  is 0. The constitutive law according a linear elasticity assumption reads

$$\sigma = C : \varepsilon = C : \nabla^s d, \quad (2.5)$$

where,  $\nabla^s$  denotes the symmetrical operator.  $C$  is the linear elastic constitutive matrix as

$$C = \begin{bmatrix} \lambda + 2\mu & \lambda & 0 \\ \lambda & \lambda + 2\mu & 0 \\ 0 & 0 & \mu \end{bmatrix}. \quad (2.6)$$

with  $\lambda$  and  $\mu$  denoting the Lamé's parameters [81]. The strain tensor  $\varepsilon$  is expressed as

$$\varepsilon = \nabla^s d = \frac{1}{2} (\nabla d + \nabla^T d), \quad (2.7)$$

where  $\nabla$  denotes the gradient operator,  $\nabla^T$  denotes the transpose gradient operator and  $\nabla^s$  denotes the symmetric gradient operator.

Substituting Eqs. (2.5) and (2.7) in the governing Eq. (2.1) results in a 2nd order Partial Differential Equation (PDE) for displacement field  $d$

$$\nabla \cdot (C : \nabla^s d) + f = 0. \quad (2.8)$$

The space of the displacement field  $U$  is equal to  $\bar{u}$  on  $\Gamma_u$  and discontinuous on  $\Gamma_c$ . The test function is then defined as

$$d_0 = \{v \in U : v = 0 \text{ on } \Gamma_u, \ v \text{ discontinuous on } \Gamma_c\}. \quad (2.9)$$

The weak form of Eq. (2.8) is given as

$$\int_{\Omega} \varepsilon(v) : \sigma d\Omega = \int_{\Gamma_t} v \cdot \bar{t} d\Gamma_t + \int_{\Omega} v \cdot f d\Omega \quad \forall v \in U. \quad (2.10)$$

## 2.2. EXTENDED FINITE ELEMENT METHOD

Unlike the classical FEM, where unstructured grids are employed when fractures exist, the XFEM can be effectively implemented using structured grids. XFEM introduces enrichment functions to the nodes that are affected by fractures, as shown in Fig. 2.2.

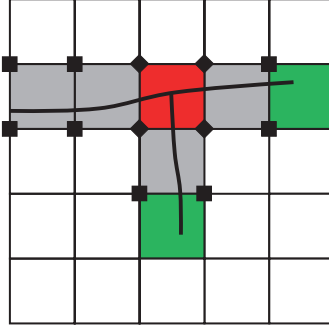


Figure 2.2: An illustration of enrichment mechanism of XFEM. The black square nodes denote the jump enriched nodes. The black diamond nodes represent the cross enriched nodes. Grey colored elements are the elements that are cut through by fractures. Green colored elements are the elements that contain fractures tips. The red element represents an element intersected by fractures in a crosswise manner.

In XFEM, three types of enrichments are normally introduced to the classic shape functions to represent discontinuities. Below, a brief description of these three enrichment functions is provided.

### 2.2.1. JUMP ENRICHMENT

The jump enrichment represents the discontinuity in the displacement field across the fracture. The jump enrichment is often chosen as a step function, which can be expressed as

$$H(x) = \begin{cases} 1 & \text{on } \Omega^+ \\ -1 & \text{on } \Omega^- \end{cases}. \quad (2.11)$$

Note that the zone  $\Omega^+$  and the zone  $\Omega^-$  are determined based on the normal vector  $n$  pointing out of the fracture. The jump function is plotted in Fig. 2.3. Each jump enriched node will have two extra DOFs (in 2D). The definition of extra DOFs will be introduced in section 2.2.4.

### 2.2.2. TIP ENRICHMENT

The tip enrichment function captures the discontinuity of the displacement field near the fracture tip. Based on the state-of-the-art XFEM, two types of tip enrichment functions are typically applied. The first type, denoted by  $F_I$ , is based on the auxiliary dis-

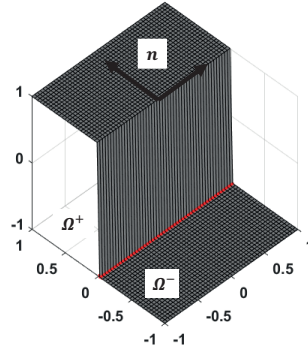


Figure 2.3: An illustration of jump function. The fracture is from coordinate  $[-1, 0]$  to  $[1, 0]$  and plotted as red color segment.

placement field near the fracture tip [59].  $F_I$  contains a group of four functions as

$$F_I(r, \theta) = \left\{ \sqrt{r} \sin\left(\frac{\theta}{2}\right), \sqrt{r} \cos\left(\frac{\theta}{2}\right), \sqrt{r} \sin\left(\frac{\theta}{2}\right) \sin(\theta), \sqrt{r} \cos\left(\frac{\theta}{2}\right) \sin\left(\frac{\theta}{2}\right) \right\}. \quad (2.12)$$

Here,  $\theta$  ranges from  $[-\pi, \pi]$ , which is defined based on the local polar coordinates of a point with respect to the fracture tip. An illustration of  $F_I$  is shown in Fig. 2.4. Each of the four functions will have two extra DOFs thus each tip enriched node will have in total 8 extra DOFs in 2D and 16 extra DOFs in 3D.

Another type of tip enrichment is more consistent with the jump enrichment [82]. This local-zone tip enrichment function covers the area that is only affected by the fracture segment that partially cut the element, as shown in the Fig. 2.5 from original work.

In this thesis, it is important to note that the elements are not in triangular shape; instead, they possess a rectangular configuration. Therefore, this type of tip enrichment necessitates some adjustments to be considered in this study. As depicted in Fig. 2.7, an example of local-zone tip enrichment for a rectangular element is showcased. The boundary that is cut by the fracture is firstly determined, which is the boundary  $AD$ . Note that now only nodes  $A$  and  $D$  will be affected by this local-zone tip enrichment functions. Subsequently, a segment  $EF$ , parallel to  $AD$  and encompassing the fracture tip  $T$ , is delineated. Notably, only Gauss points situated within the grey-shaded rectangular area  $AFED$  will exhibit non-zero values for the local tip enrichment functions.

The local-zone tip enrichment function is determined as follows. The area  $AFED$  will be transferred to the reference rectangle  $A'F'E'D'$ . The Gauss point with its coordinates as  $[\xi, \eta]$  in the original element  $ABCD$  will be transferred to the Gauss point that belongs to the reference rectangle  $A'F'E'D'$  with coordinates  $[\xi', \eta']$ . The local-zone tip enrichment function of Gauss point  $[\xi, \eta]$  is then computed as

$$T(\xi, \eta) = N_{x_n}^*(\xi', \eta') \cdot (H(\xi, \eta) - H(x_n)), \quad (2.13)$$

where  $N_{x_n}^*(\xi', \eta')$  represents the standard shape functions on Gauss point  $[\xi', \eta']$  inside the reference rectangle  $A'F'E'D'$ .  $x_n$  are the jump enriched nodes of the element  $ABCD$ ,

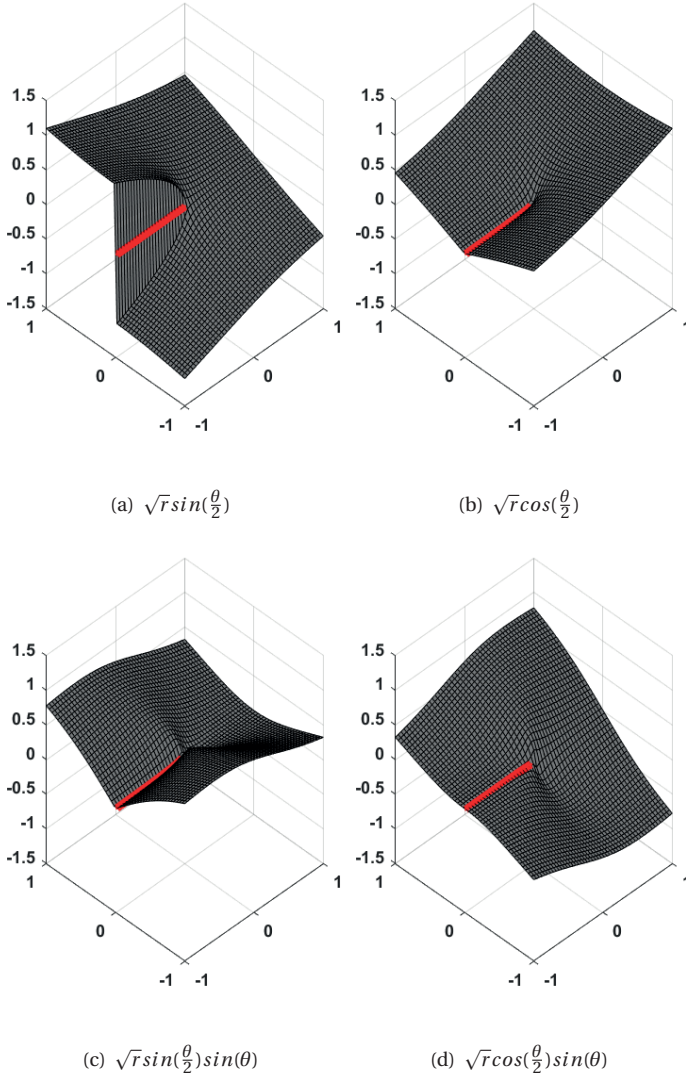


Figure 2.4: An illustration of four tip enrichment functions in an element. The red segment represents the fracture from  $[-1,0]$  to  $[0,0]$ .

i.e.,  $AD$ .  $H(\xi, \eta)$  is the jump enrichment function on Gauss point  $[\xi, \eta]$  inside the original element  $ABCD$  and  $H(x_n)$  are the jump enrichment function values on the enriched nodes  $AD$ . Fig. 2.7 shows an example of the local-zone tip enrichment function. Given that this local-zone tip enrichment function operates as a form of jump enrichment, it is noteworthy that no additional degrees of freedom (DOFs) are allocated to nodes  $B$  and  $C$ . In contrast to the earlier tip enrichment functions depicted in Fig. 2.4,

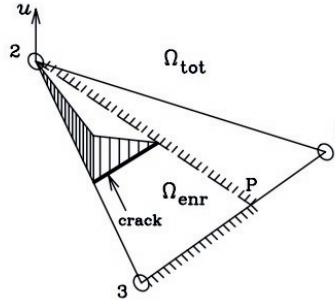


Figure 2.5: An illustration of the new tip enrichment framework. The figure is derived from [82].

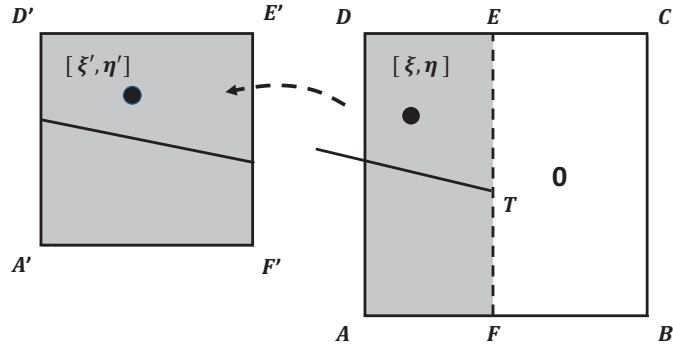


Figure 2.6: An illustration of the modified local-zone tip enrichment function. This modified local-zone tip enrichment function only affects in the gray colored zone  $AFED$ .  $A'F'E'D'$  is then transferred reference rectangle of  $AFED$ .

this local-zone tip enrichment function introduces minimal extra DOFs to the entire system while effectively capturing the discontinuity surrounding the fracture tip.

### 2.2.3. JUNCTION ENRICHMENT

In a multiple fractures simulation, deformation of crossing fractures need to be modeled as well. To simulate this configuration with XFEM, a junction enrichment, or the crossing enrichment, is applied [65]. There are two situations of crossing considered: T-shape crossing and X-shape crossing. The T-shape enrichment is the commonly seen scenario in underground fracture networks which is illustrated in Fig. 2.8 (a). The crack with its tip joined with another crack's main path is called the minor crack and the other crack is called the main crack. For any Gauss point in the T-shape crossed element there is one jump function addressed due to the major crack. If this Gauss point is on the negative side of the main crack, i.e., the jump function value due to main crack  $H_I(x)$  is negative,

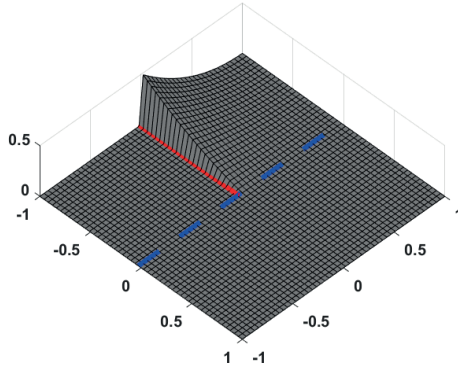


Figure 2.7: An illustration of the local-zone tip enrichment function for an element that contains the fracture tip on coordinates  $[0, 0]$ . The red segment represents a fracture from  $[-1, 0]$  to  $[0, 0]$  and the blue dashed segment represents the segment  $EF$  in Fig. 2.6.

the junction enrichment function value is 0. If this point is on the positive side of the main crack, i.e., the jump function value due to main crack  $H_I(x)$  is positive, the junction enrichment function value is equal to the jump enrichment function value due to the minor crack  $H_{II}(x)$ . Thus T-shape function  $J(x)$  is given by

$$J(x) = \begin{cases} H_{II}(x) & H_I(x) > 0 \\ 0 & H_I(x) < 0 \end{cases} \quad (2.14)$$

Another type of crossing is X-shape crossing as shown in Fig. 2.8 (b). To enrich this,

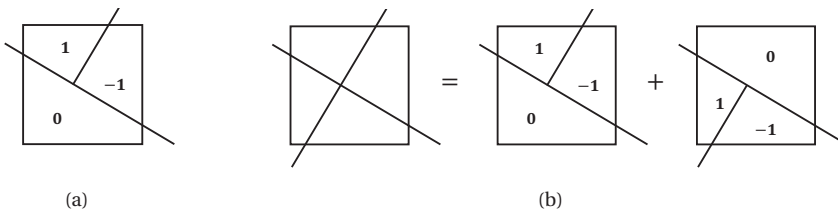


Figure 2.8: Two types of the junction enrichment functions (a) T-shape junction enrichment functions. (b) X-shape junction enrichment divided into two T-shape enrichment functions.

usually the minor crack is decomposed into two minor DOFs. Thus, two sets of T-shape functions are introduced to each of the X-shape enriched node. Note that for either T-shape or X-shape junction enrichment, there will always be a jump enrichment added to each junction enriched node due to the main crack.

### 2.2.4. XFEM LINEAR SYSTEM

XFEM approximates the displacement field  $d$  at fine-scale resolution  $h$  by  $d^h$  which is defined as

$$d \approx d^h = \sum_{i \in N_I} u_i N_i + \sum_{j \in N_E} a_j N_j (S(x) - S(x_c)), \quad (2.15)$$

where  $N_I$  represents all the nodes in the domain while  $N_E$  denotes the group of enriched nodes.  $N_i$  and  $N_j$  represent the FEM bilinear shape functions of node  $i$  and  $j$  and  $S$  represents the enrichment functions including the jump function  $H$ , the junction enrichment functions  $J$  and the local-zone tip enrichment functions  $T$ .  $x_c$  represents the enriched mesh nodes,  $u$  denotes the standard DOFs associated to the classical finite element method and  $a$  denotes the extra DOFs associated to the enriched nodes. The resulting linear system entails the nodal displacement unknowns  $u$ , as well as the enriched extra DOFs  $a$  per fracture (and fault). The augmented XFEM linear system  $K^h d^h = f^h$ , therefore, reads

$$\underbrace{\begin{bmatrix} K_{uu} & K_{ua} \\ K_{au} & K_{aa} \end{bmatrix}}_{K^h} \underbrace{\begin{bmatrix} u \\ a \end{bmatrix}}_{d^h} = \underbrace{\begin{bmatrix} f_u \\ f_a \end{bmatrix}}_{f^h}. \quad (2.16)$$

The strain tensor  $\varepsilon$  of Eq. (2.7) is then expressed as

$$\varepsilon = B^{st} u + B^{en} a, \quad (2.17)$$

in which the standard strain matrix  $B^{st}$  is defined as derivatives of standard shape functions  $N^{st}$  as

$$B^{st} = \begin{bmatrix} \partial N_i^{st} / \partial x & 0 & \dots \\ 0 & \partial N_i^{st} / \partial y & \dots \\ \partial N_i^{st} / \partial y & \partial N_i^{st} / \partial x & \dots \end{bmatrix} \quad \forall i \in N_I. \quad (2.18)$$

The enrichment functions used in this thesis are all in the style of step functions and their derivatives are 0. The enriched strain matrix  $B^{en}$  is defined as derivatives of enriched shape functions as

$$B^{en} = \begin{bmatrix} \partial N_i(S(x) - S(x_c)) / \partial x & 0 & \dots \\ 0 & \partial N_i(S(x) - S(x_c)) / \partial y & \dots \\ \partial N_i(S(x) - S(x_c)) / \partial y & \partial N_i(S(x) - S(x_c)) / \partial x & \dots \end{bmatrix} \quad \forall i \in N_E. \quad (2.19)$$

Thus the detailed stiffness matrix  $K^h$  of Eq. (2.16) is written as

$$K^h = \begin{bmatrix} \int_{\Omega} (B^{st})^T C B^{st} d\Omega & \int_{\Omega} (B^{st})^T C B^{en} d\Omega \\ \int_{\Omega} (B^{en})^T C B^{st} d\Omega & \int_{\Omega} (B^{en})^T C B^{en} d\Omega \end{bmatrix}. \quad (2.20)$$

The right-hand side  $f^h$  is expressed as

$$f^h = \begin{bmatrix} \int_{\Gamma} (N^{st})^T \cdot \bar{t} d\Gamma + \int_{\Omega} (N^{st})^T \cdot f d\Omega \\ \int_{\Gamma} (N^{en})^T \cdot \bar{t} d\Gamma + \int_{\Omega} (N^{en})^T \cdot f d\Omega \end{bmatrix}. \quad (2.21)$$

## 2.3. FRACTURE PROPAGATION

### 2.3.1. PROPAGATION CRITERION

The fracture increment in this thesis is defined as a user-defined input for convenience; however, this increment can also be defined based on other strategies, such as the energy release criterion. To determine whether or not a fracture tip should grow, Griffith's theory [83] states that the fracture tip will grow if the energy release rate,  $G$ , is larger than or equal to the critical energy release rate,  $G_c$ . This is expressed as

$$G \geq G_c, \quad (2.22)$$

where  $G$  is defined as the rate of energy decreased per unit fracture surface area increased. Eq. (2.22) can also be written in terms of the stress intensity factor  $K$  as

$$K \geq K_c, \quad (2.23)$$

where  $K_c$  is called the fracture toughness. Unlike propagation of a single fracture, the impact of the increment of one fracture tip to another needs to be considered as well in a multiple fractures propagation problem. Some fracture tips will grow and they are grouped as competitive tips  $n_{comp}$ . These tips must strictly follow Eq. (2.23). But not all of them can grow since the whole fractured system tend to form a stable crack pattern with minimum energy dissipation [84]. The unstable configuration of fractures path is defined as

$$\left( \frac{\partial G_i}{\partial l_j} - \frac{\partial G_{c,i}}{\partial l_j} \right) \geq 0 \quad \forall i, j \in n_{comp}, \quad (2.24)$$

where  $\partial G_i / \partial l_j$  is the derivative of energy release rate of crack tip  $i$  with respect to crack tip  $j$  increment.  $\partial G_{c,i} / \partial l_j$  is the derivative of critical energy release rate of crack tip  $i$  with respect to crack tip  $j$  increment. At the beginning of each fracture growth step, the matrix  $\partial G / \partial l$  needs to be constructed to check whether the chosen growing path meets the criterion described by Eq. (2.24). The double virtual incremental method is applied to construct the matrix  $\partial G / \partial l$  [84]. In the double virtual incremental method, it is assumed that the growth of the tips would only affect a small region near the fractures' tips. The virtual fracture tip  $i$  increment,  $l_i$ , is approximated using virtual displacement function  $\Theta_i$ . The virtual fracture tip  $j$  increment,  $l_j$ , is approximated using the virtual displacement function  $\Pi_j$ . These functions are shown in Fig. 2.9. Note that the radius of the non-zero gradient zone of function  $\Pi$  is normally twice the radius of the none-zero gradient zone of function  $\Theta$ .

The virtual displacement field  $\tilde{d}_j$  is constructed in order to compute  $\partial G_i / \partial l_j$ . To compute this virtual displacement field, a virtual force vector  $\tilde{f}_{\Pi_j}$  around the fracture tip  $j$  is defined as

$$\tilde{f}_{\Pi_j} = \int B^T (C \tilde{B}_{\Pi_j} d - \sigma \operatorname{div}(\Pi_j)) d\Omega + \int \tilde{B}_{\Pi_j}^T \sigma d\Omega, \quad (2.25)$$

where  $C$  is the linear elastic constitutive matrix.  $B$  matrix represents the strain-displacement matrix that contains the standard part of Eq. 2.18 and enriched part of Eq. 2.19. The matrix  $\tilde{B}_{\Pi_j}$  is assembled similar to the construction of the  $B$  matrix. Each component of

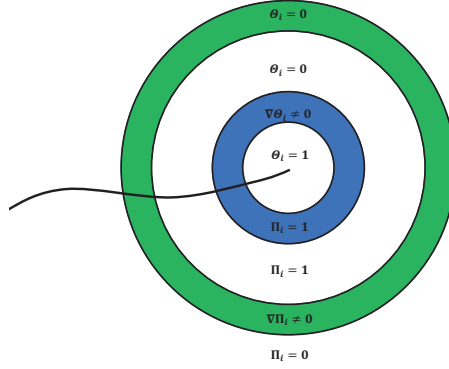


Figure 2.9: An illustration of the virtual displacement functions  $\Theta$  and  $\Pi$  and their gradients.

$\tilde{B}_{\Pi_j}$  is constructed by multiplying the gradient of function  $\Pi$ . Details can be found in [85]. The virtual displacement field  $\tilde{d}_j$  is given by

$$\tilde{d}_j = \left(K^h\right)^{-1} \tilde{f}_{\Pi_j}. \quad (2.26)$$

The derivative of the energy release rate at fracture tip  $i$  corresponding to incremental of fracture tip  $j$  increment is computed using

$$\frac{\partial G_i}{\partial l_j} = d^T \left[ \int (B^T C \tilde{B}_{\Theta_i} + \tilde{B}_{\Theta_i}^T C B - B^T C B) d\Omega \right] \tilde{d}_j^T. \quad (2.27)$$

The construction of  $\tilde{B}_{\Theta_i}$  is carried out by multiplying  $B$  with the gradient of function  $\Theta$ . The matrix  $\partial G/\partial l$  is constructed by assembling the terms  $\partial G_i/\partial l_j$ . The maximum subdeterminant of matrix  $\partial G/\partial l$  provides the set of fracture tips that would grow in the current time step, defined as  $N_{grow}$ , which read

$$N_{grow} = \underbrace{\max}_{\forall i, j \in n_{comp}} \left( \det \left( \frac{\partial G_i}{\partial l_j} \right) \geq 0 \right). \quad (2.28)$$

If the maximum subdeterminant value is negative, no fracture tips will grow.

### PROPAGATION SPEED AND ANGLE

The fracture increment in this thesis is defined as a user-defined input. In this thesis, it is normally defined as 2 to 3 times the mesh size. The angle of propagation can be quantified using different theories. As a commonly used theory, the maximum principal stress theory is used to predict the direction of fracture propagation as

$$\theta = 2 \arctan \left( \frac{1}{4} \left( \frac{K_I}{K_{II}} \pm \sqrt{\left( \frac{K_I}{K_{II}} \right)^2 + 8} \right) \right), \quad (2.29)$$

where  $K_I$  is the stress intensity factor (SIF) for mode I fracture which means the opening mode fracture and  $K_{II}$  is the stress intensity factor for mode II fracture which represents the sliding mode fracture. In this thesis, the computation of Stress Intensity Factors (SIFs) follows the same procedure presented in the paper by Moes et al [59]. This method works well with non-cohesive tensile fracture but sometimes has problems with an embedded method such as XFEM. This will be illustrated in the chapter 6.

Another method used to determine the propagation angle is the weighted spatial average method [62]. In this method, all stress vectors at all Gauss points inside a circular sector window ahead of the fracture tip are averaged, as shown in Fig. 2.10.

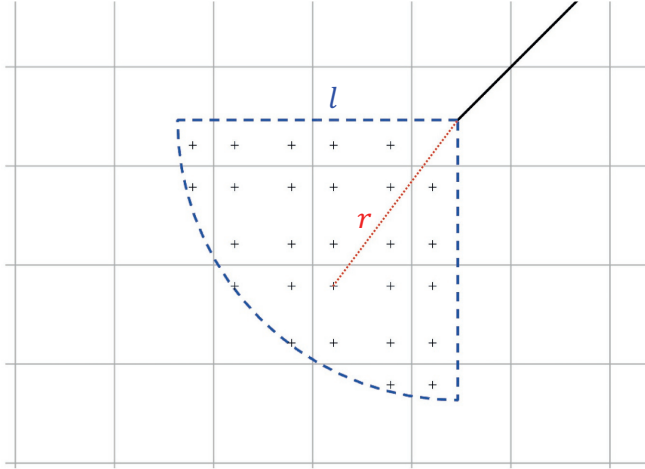


Figure 2.10: A sketch of circular sector window. All stress vectors belong to the Gauss points marked with 'plus' signs in the figure are used for weighted spatial average of stress vectors.

The stress vector's weight at each Gauss point, which contributes to the averaged stress vector, reads

$$w = \frac{1}{(2\pi)^{\frac{3}{2}} l^3} \exp\left(-\frac{r^2}{2l^2}\right), \quad (2.30)$$

where,  $l$  is the radius of the window that is normally 3 to 4 times the mesh size and  $r$  is the distance of each Gauss point to the fracture tip. After obtaining the spatial averaged stress vector, the propagation angle is then calculated as the direction perpendicular to the maximum principle stress direction of this averaged stress vector.

## 2.4. LEVEL SET FUNCTIONS

Level set functions are often applied to represent the geometry of discontinuities [66, 67]. Level set functions are usually defined as signed distance functions. Two level set functions are applied in this thesis, as shown in Fig. 2.11 (a). The first function,  $\psi$ , represents the signed distance from any point to the main crack path. It is defined as

$$\psi(x, t) = \pm \min_{x^{\Gamma_c} \in \Gamma_c} \|(x - x^{\Gamma_c})\|, \quad (2.31)$$

where  $\Gamma_c$  represents the crack or discontinuity interface and  $x^{\Gamma_c}$  represents any point on the crack surface  $\Gamma_c$ . Thus  $\phi$  is zero at the fracture interface. The second fine-scale,  $\phi$ , is defined as the signed distance to the tangential line  $\xi$  crossing the crack tip, defined as

$$\phi_i(x, t) = \pm \min_{x^\xi \in \xi, i} \|(x - x^\xi)\| \quad i = 1, 2, \quad (2.32)$$

where  $\xi$  represents the zero valued interface for fine-scale  $\phi$  and  $x^\xi$  represents points on the crack surface  $\xi$ . Normally, there will be two  $\phi$  functions, each indicating one of the two tips for each crack. To combine them into one function, the maximum value of  $[\phi_1, \phi_2]$  is selected as the  $\phi$  value for any point in the domain, i.e.,

$$\phi(x, t) = \max(\phi_1, \phi_2). \quad (2.33)$$

#### 2.4.1. LEVEL SET FINE-SCALES FOR ENRICHMENT

With the assistance of level set fine-scales it is straightforward to determine the enrichment types for nodes. For each element, the level set fine-scale values will be computed on the four nodes (2D domain) connected to this element, as shown in Fig. 2.11 (b). If this element is cut through by fractures, meaning that the zero-valued interface of function  $\psi$  crosses the element, there will be some nodes located on the positive zone of fine-scale  $\psi$  while the rest are located on the negative zone. All four nodes should have negative values of  $\phi$  fine-scale. The criterion is expressed as

$$\max(\psi) \cdot \min(\psi) < 0, \max(\phi) < 0. \quad (2.34)$$

Thus all four nodes connected to this element are enriched by a jump fine-scale. If this element contains the fracture tip, the zero valued interface of fine-scale  $\phi$  cuts through the element. Some of the nodes are located on the positive values of fine-scale  $\phi$  while the rest are located on the negative zone. Also the zero valued interface of fine-scale  $\psi$  will cross the element that contains fractures tips thus the criterion of Eq. (2.34) is still required in here. The criterion to determine if this element contains the tip is expressed as

$$\max(\psi) \cdot \min(\psi) < 0, \max(\phi) \cdot \min(\phi) < 0. \quad (2.35)$$

As for the cross enriched element, if certain element meets the criterion of Eq. (2.34) for multiple fractures, a geometrical check will be performed inside that element. If two fractures cross each other inside this element the cross enrichment is applied to all four nodes connected to this element.

#### 2.4.2. LEVEL SET FINE-SCALES FOR FRACTURES PROPAGATION

The propagation of fractures also represent the geometric extensions of discontinuities, which can be tracked by updating level set fine-scales. The angle to update the level set fine-scales is computed using Eq. (2.29). The incremental crack length is also explicitly known as user-defined input and its value is denoted as  $\|\mathbf{F}\|$ . The growth of the tip is then traced by updating the zero valued interface of fine-scale  $\phi$  with propagation speed

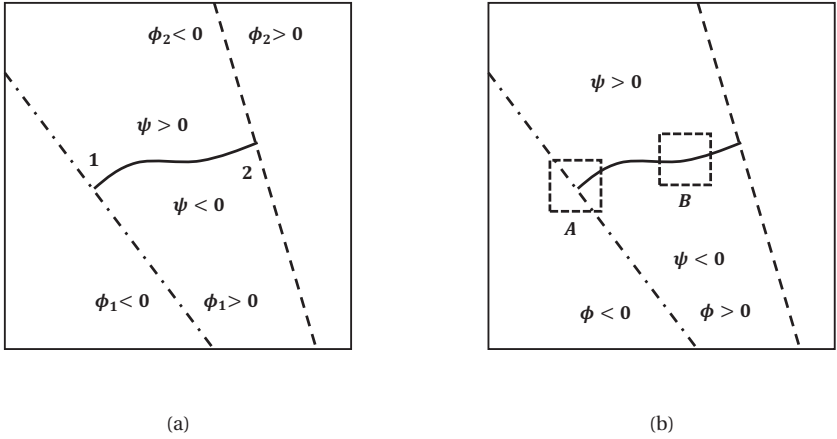


Figure 2.11: (a) level set fine-scales sketch (b) level set fine-scales values distribution on the four nodes connected to the element that contains the fracture tip (element A) or the element that cuts through by the fracture (element B).

$$\mathbf{F} = (F_x, F_y).$$

The current fine-scales  $\phi$  at time step,  $\phi^t$ , are rotated with angle  $\theta$  as shown in Fig. 2.12. The fine-scale  $(\phi^t)'$  represents the rotated fine-scale  $\phi^t$ . Next, the fine-scale  $\phi^{t+1}$  is updated via

$$\phi^{t+1} = (\phi^t)' - \|\mathbf{F}\|. \quad (2.36)$$

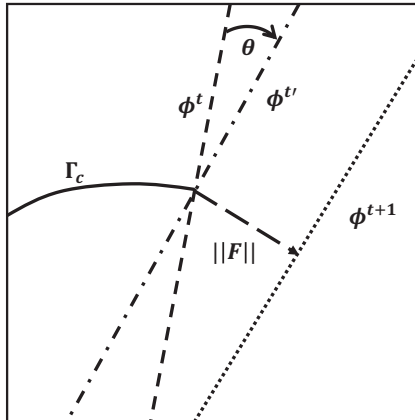


Figure 2.12: An illustration of updating the level set fine-scales.

After updating fine-scales  $\phi$ , the fine-scale  $\psi$  is recomputed to obtain  $\psi^{t+1}$ . Details can

be found in the literature [67]. Updating the level set fine-scale values is not needed for all elements in the computational domain. The level set fine-scales update can be limited to the elements, or to a narrow band, in which the fracture tips will propagate.

## 2.5. PENALTY METHOD FOR COMPRESSION FRACTURES

The penalty method is frequently integrated with XFEM for the purpose of modeling contact problems. This approach introduces a penalty term into the problem's formulation that penalizes the violation of contact constraints. In the context of contact problems, these constraints are expressed as non-penetration conditions, which prevent the penetration of two bodies, and frictional conditions, which consider the development of tangential forces between the contacting bodies.

### 2.5.1. CONTACT LAW

As illustrated in Fig. 2.13, compressive displacements  $\bar{u}$  imposed on  $\Gamma_u$  and traction  $\bar{t}$  imposed on  $\Gamma_t$  make the discontinuity surface  $\Gamma_c$  self contact and thus the contact forces  $f_c$  in between two sides of fractures surfaces are not 0.

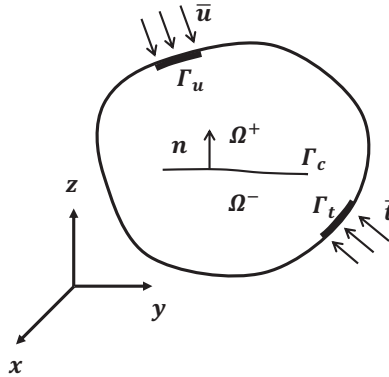


Figure 2.13: An illustration of the fractured domain under compressive loading setup.

The weak form of the stress equilibrium equation with contact forces in between fractures surfaces reads

$$\int_{\Omega} \epsilon(v) : \sigma d\Omega + \int_{\Gamma_c} f_c \cdot \llbracket v \rrbracket d\Gamma_c = \int_{\Gamma_t} v \cdot \bar{t} d\Gamma_t + \int_{\Omega} v \cdot f d\Omega \quad \forall v \in U, \quad (2.37)$$

where  $\Omega^+$  and  $\Omega^-$  are the two bodies separated by fracture  $\Gamma_c$ . The displacement difference  $\llbracket d \rrbracket$  between two sides of fracture  $\Gamma_c$  is defined as

$$\llbracket d \rrbracket = d_+ - d_- \quad (2.38)$$

where  $d_+$  and  $d_-$  are the displacements of fracture surfaces that belong to  $\Omega^+$  and  $\Omega^-$ , respectively. In XFEM, the displacement difference can be expressed as

$$\llbracket d \rrbracket = \llbracket N \rrbracket d = \begin{bmatrix} (N_+^{st} - N_-^{st})u \\ (N_+^{en} - N_-^{en})\bar{a} \end{bmatrix} = \begin{bmatrix} 0 \\ (N_+^{en} - N_-^{en})\bar{a} \end{bmatrix}. \quad (2.39)$$

Note that the standard shape fine-scales, denoted as  $N^{st}$ , exhibit continuity throughout, resulting in a difference of 0 between the two sides of the fracture surfaces.

The gap fine-scale is then described as

$$g_N = n_{\Gamma_c} \otimes n_{\Gamma_c} \llbracket u \rrbracket, \quad (2.40)$$

and

$$g_T = (I - n_{\Gamma_c} \otimes n_{\Gamma_c}) \llbracket u \rrbracket, \quad (2.41)$$

where, the  $n_{\Gamma_c}$  is the normal direction of fracture  $\Gamma_c$  and  $I$  is the identity matrix. During the simulation of contact and sliding, strict non-penetration between the two sides of the fractures is enforced. This means that  $g_N \geq 0$ . When  $g_N > 0$ , the contact force is 0. When the two side of fractures contact each other, or  $g_N = 0$ , the contact force  $f_c < 0$ . The contact law is thus described as

$$g_N \geq 0, \quad f_c \leq 0, \quad g_N f_c = 0. \quad (2.42)$$

This statement represents the Kuhn-Tucker conditions for the self contact model [86]. In the self-contact problem, the behavior of the two sides of the fractures, whether they slide or remain in contact, depends on both external loading and the material-specific frictional coefficient  $\mu_f$ . This state of sliding or sticking is determined using Coulomb's law of friction, i.e.,

$$\|f_{cT}\| - \mu_f \|f_{cN}\| \leq \begin{cases} = 0 & \text{slip} \\ < 0 & \text{stick.} \end{cases} \quad (2.43)$$

where,  $f_{cN}$  represents the normal contact force and  $f_{cT}$  represents the tangential contact force. The expressions of  $f_{cT}$  and  $f_{cN}$  are defined in section 2.5.2.

### 2.5.2. PENALTY METHOD

To enforce the contact constraints, a penalty term is introduced, involving the addition of a penalty coefficient to these constraints. The penalty coefficient is a sufficiently large positive number, guaranteeing the satisfaction of the contact constraints. In practice, the penalty method operates by penalizing the displacement and rotation of the nodes that violate these contact constraints. This approach effectively stiffens the structure near the contact interface, enabling precise modeling of contact behavior. The normal contact force acting on the fracture is expressed as

$$f_{cN} = C_N g_N, \quad (2.44)$$

where,  $C_N$  represents the penalty parameter along the normal direction of the fracture, ensuring the prevention of penetration. The tangential contact force  $f_{cT}$  is expressed as

$$\dot{f}_{cT} = C_T (\dot{g}_T - \dot{S} \frac{f_{cT}}{\|f_{cT}\|}), \quad (2.45)$$

where,  $C_T$  denotes the penalty parameter along the normal direction of the fracture, while  $\dot{S}$  represents the slip rate along the fracture. Under the "stick" condition,  $\dot{S}$  equals 0, resulting in a tangential contact force of  $C_T g_T$ . Conversely, when the "slip" condition occurs, a return mapping method is employed to calculate the tangential direction contact force [64, 87]. The return mapping method operates as follows: at iteration  $\nu + 1$ , after obtaining the incremental tangential displacement jump  $\Delta g_T^{\nu+1}$ , the normal displacement jump  $g_N^{\nu+1}$  and the tangential contact force  $f_{cT}^\nu$  from last iteration  $\nu$ , the predicted updated tangential contact force is calculated as

$$f_{cT}^{pr} = f_{cT}^\nu + C_T \Delta g_T^{\nu+1}. \quad (2.46)$$

If this predicted value adheres to Coulomb's criterion, as expressed by

$$\|f_{cT}^{pr}\| - \mu_f \|C_N g_N^{\nu+1}\| \leq 0 \quad (2.47)$$

which is accepted as the tangential contact force at this iteration  $f_{cT}^{\nu+1}$ . Otherwise, if the criterion is not met, it is corrected to reflect the fact that the fracture is indeed in slip mode. The corrected tangential contact force is equal to the sliding frictional force

$$\|f_{cT}^{\nu+1}\| = \mu_f \|C_N g_N^{\nu+1}\|. \quad (2.48)$$

### 2.5.3. LINEAR SYSTEM

The linear matrix system of Eq. (2.37) has one additional term compared to the linear system from Eq. (2.10), which means only one more term needs to be added to matrix  $K$  in Eq. (2.20) as

$$K^p = \begin{bmatrix} K_{uu} & K_{ua} \\ K_{au} & K_{aa} + K_{con} \end{bmatrix}, \quad (2.49)$$

where the contact matrix  $K_{con}$  is expressed as

$$K_{con} = \int_{\Gamma_c} ([N^{en}])^T \frac{\partial f_c}{\partial a} d\Gamma_c = \int_{\Gamma_c} [N^{en}]^T D [N^{en}] d\Gamma_c. \quad (2.50)$$

The term  $[N^{en}]$  is expressed as

$$[N^{en}] = (N_+^{en} - N_-^{en}). \quad (2.51)$$

The  $D$  matrix contains the penalty parameters in both normal and tangential directions. Depending on the stick or slip state, the matrix  $D$  can be different. In slip state, the tangential force is equal to the sliding frictional force in Eq. 2.48 thus in slip state the  $D$  matrix is

$$D = C_N \cdot (n_{\Gamma_c} \otimes n_{\Gamma_c}) + \frac{f_{cT}^{\nu+1}}{\Delta g_T^{\nu+1}} \cdot (I - n_{\Gamma_c} \otimes n_{\Gamma_c}), \quad (2.52)$$

in which the  $n_{\Gamma_c} \otimes n_{\Gamma_c}$  term represents the projection matrix that projects the vector to the normal direction of fracture  $\Gamma_c$ . In stick state,  $D$  matrix is

$$D = C_N \cdot (n_{\Gamma_c} \otimes n_{\Gamma_c}) + C_T \cdot (I - n_{\Gamma_c} \otimes n_{\Gamma_c}), \quad (2.53)$$

## 2.6. CONCLUSIONS

where  $I - n_{\Gamma_c} \otimes n_{\Gamma_c}$  represents the projection matrix that projects the vector to the tangential direction of fracture  $\Gamma_c$ .

The return mapping strategy requires an iterative solver. The linear system

$$(K^p)^i \Delta d^{i+1} = r^i \quad (2.54)$$

is iteratively solved until convergence is reached. Matrix  $K^p$  undergoes updates in accordance with the stick-slip conditions observed at the Gauss points on the fractures. The right hand side  $r$  in Eq. 2.54 is expressed as

$$r = \begin{bmatrix} \int_{\Gamma} (N^{st})^T \cdot \bar{t} d\Gamma + \int_{\Omega} (N^{st})^T \cdot f d\Omega - \int_{\Omega} (B^{st})^T \cdot \sigma d\Omega \\ \int_{\Gamma} (N^{en})^T \cdot \bar{t} d\Gamma + \int_{\Omega} (N^{en})^T \cdot f d\Omega - \int_{\Omega} (B^{st})^T \cdot \sigma d\Omega - \int_{\Gamma_c} ([N^{en}])^T \cdot f_c d\Gamma_c \end{bmatrix}. \quad (2.55)$$

The matrices  $K_{con}$  and  $f_c$  are determined through integration across the Gauss points situated along the fracture segments. For reference, Figure 2.14 illustrates the positions of Gauss points along the fracture in three scenarios: within the element crossing the crack, within the element containing the kinked fracture point, and within the element housing the fracture tip.

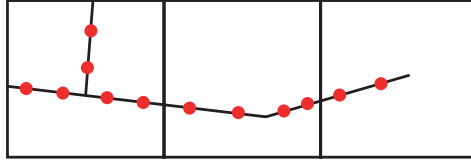


Figure 2.14: An illustration of Gauss points positions along the fracture.

## 2.6. CONCLUSIONS

In this chapter, the problem formulations for fractured media and the corresponding fine-scale simulation strategies are introduced. The details of various types of enrichments at fine-scale, along with a comprehensive explanation of the linear system of XFEM, are provided. The principles governing fracture propagation, including the determination of propagation angles and the utilization of level sets at fine-scale with XFEM, are outlined. The application of the penalty method, coupled with XFEM, is fully explained to prevent penetration between fracture surfaces. While these strategies offer precise solutions for highly fractured formations, they incur a high computational cost. This challenge is addressed in the subsequent chapter through the introduction of MS-XFEM.



# 3

## MULTISCALE EXTENDED FINITE ELEMENT METHOD (MS-XFEM)

This chapter is devoted to the central theme of this thesis: the Multiscale Extended Finite Element Method (MS-XFEM). The basis functions are constructed by solving local XFEM problems. Building upon this localized solving approach, this chapter provides a comprehensive exposition of an algebraic strategy to formulate and implement the MS-XFEM. Remarkably, these basis functions accurately capture the fractures by involving the extra DOFs and allow for construction of the FEM-based coarse-scale system. An exploration of the incorporation of an iterative strategy into MS-XFEM follows, aimed at mitigating errors in final solutions to any desired tolerance. A series of practical test cases is introduced to showcase the application of MS-XFEM, focusing on simulating static deformations featuring multiple fractures. In these cases, visual representations are provided to highlight the successful integration of discontinuities into the basis functions. Additionally, a thorough examination of the method's scalability and efficiency is conducted through rigorous analyses.

### 3.1. MULTISCALE SIMULATION STRATEGY

In accordance with the discussions presented in Chapter 1 and Chapter 2, it is evident that classical XFEM, a widely used technique in fracture mechanics, exhibits limitations when applied to the simulation of highly fractured subsurface formations. The inherent drawback of classical XFEM becomes pronounced as the mesh is refined due to the excessive number of fractures. This refinement leads to a substantial increase in the number of extra DOFs, thereby expanding the size of the linear system to a point where computational efficiency becomes a significant challenge. Consequently, to address this issue and achieve a balanced trade-off between computational efficiency and solution

---

This chapter is based on the publication: Xu, F., Hajibeygi, H., & Sluys, L. J. (2021). Multiscale extended finite element method for deformable fractured porous media. *Journal of Computational Physics*, 436, 110287. [88]

accuracy, this work incorporates a multiscale strategy in conjunction with XFEM. In this section, a multiscale strategy will be explained. The fine scale solution  $d^h$  can be approximated with the solution field  $d^{lh}$  by a multiscale formulation

$$d^h \approx d^{lh} = P d^H, \quad (3.1)$$

where  $P$  is the matrix of basis functions (i.e., prolongation operator) and  $d^H$  are the nodal displacements at the coarse scale mesh  $\Omega^H$ . Prolongation operator  $P$  has the dimension of  $N^h \times N^H$ .  $N^h$  is the size of the fine-scale enriched XFEM system including the extra DOFs and  $N^H$  is the size of the coarse mesh. All extra DOFs and enrichment functions are included in matrix  $P$  instead of vector  $d^H$ . This is crucial in significantly improving the computational efficiency in these large-scale heterogeneous systems.

MS-XFEM solves the linear system of equations on the coarse mesh, imposed on a given fine-scale mesh, as shown in Fig. 3.1. The coarsening ratio is defined as the ratio between the coarse mesh size and fine-scale mesh size, which is  $4 \times 4$  for the example shown in Fig. 3.1.

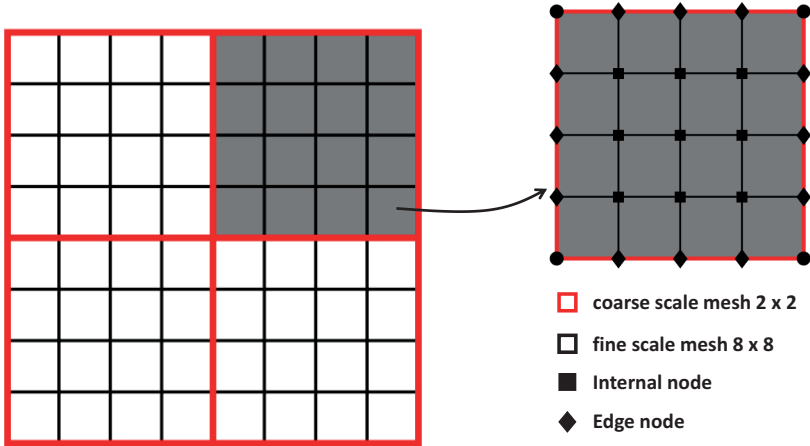


Figure 3.1: Illustration of the multiscale mesh imposed on a given fine-scale mesh, with a coarsening ratio of  $4 \times 4$ . The fine scale mesh nodes in each coarse scale element can be categorized as internal nodes, edge nodes and vertex nodes.

To construct the coarse-scale system of equations and solve for  $d^H$ , the fine-scale linear system ( $K^h d^h = f^h$ ) is restricted to the coarse-scale via

$$\underbrace{(R K^h P)}_{K^H} d^H = R f^h. \quad (3.2)$$

Here,  $R$  is the restriction operator with size  $N^H \times N^h$ , defined as the transpose of basis function operator

$$R = P^T. \quad (3.3)$$

This results in the coarse-scale system matrix  $K^H$  size of  $N^H \times N^H$ . Once the coarse-scale system is solved on  $K^H$  space for  $d^H$ , one can compute the approximate fine-scale

solution using Eq. (3.1). Overall, the multiscale procedure can be summarised as finding an approximate solution  $d^{lh}$  according to

$$d^{lh} \approx d^{lh} = P d^H = P(R K^h P)^{-1} R f^h. \quad (3.4)$$

In here, the term  $P(R K^h P)^{-1} R$  is called the multiscale operator  $M_{MS}^{-1}$ . Next, the prolongation operator  $P$ , i.e., the basis functions are explained in detail. Once  $P$  is known, all terms in Eq. (3.4) are defined.

### 3.2. CONSTRUCTION OF BASIS FUNCTIONS FOR MS-XFEM

To obtain the basis functions, in each coarse element the local XFEM problem needs to be solved. The local equilibrium equation is expressed as

$$\nabla \cdot (C : (\nabla^S N_i^H)) = 0 \quad \text{in } \Omega^H. \quad (3.5)$$

A reduced-dimensional equilibrium equation is also solved and its solution is used as the boundary solutions for Eq. 3.5, i.e.,

$$\nabla_{\parallel} \cdot (C_r : (\nabla_{\parallel}^S N_i^H)) = 0 \quad \text{on } \Gamma^H. \quad (3.6)$$

Here,  $\Gamma^H$  denotes the boundary of the coarse element  $\Omega^H$ . In addition,  $\nabla_{\parallel}^S$  denotes the reduced dimensional divergence and symmetrical gradient operators, which act parallel to the direction of the local domain boundary. Moreover,  $C_r$  is the reduced-dimensional (here, 1D) average elasticity tensor along the boundary of the coarse element. More precisely, for boundaries parallel to the x-direction, the only nonzero entries are  $C_r^x(1, 1) = \bar{\lambda}$  and  $C_r^x(3, 3) = \bar{\mu}$ ; while its nonzero entries for the boundaries parallel to y-direction are  $C_r^y(2, 2) = \bar{\lambda}$  and  $C_r^y(3, 3) = \bar{\mu}$ . Here,  $\bar{\lambda}$  and  $\bar{\mu}$  are averaged elasticity properties of the adjacent 2D elements belonging to the 1D boundary edges.

For 2D geometries, the reduced-dimensional boundary condition can be approximated using the 1D (rod) deformation model along the edges of coarse element. The local deformation in response to horizontal and vertical unity nodal displacements will be in general two-dimensional. Therefore, the prolongation matrix  $P$  will have off-block-diagonal entries (i.e.,  $P_{xy} \neq 0$  and  $P_{yx} \neq 0$ ) and reads

$$P = \begin{bmatrix} P_{xx} & P_{xy} \\ P_{yx} & P_{yy} \end{bmatrix}. \quad (3.7)$$

Fig. 3.2 shows an example of a local system to be solved for basis functions belonging to the right bottom node in x and y directions. Note that the Dirichlet value of 1 is set at the right bottom node for each directional basis functions, while all other 3 coarse mesh nodes are set to 0. Furthermore, as shown in Fig. 3.2, the boundary problem is solved for both edges which have the right bottom node at one of their end values. More precisely, e.g., to find the basis function in x-direction, the value of  $u_x = 1$  is set at the right bottom node. This causes extension of the horizontal boundary and bending of the vertical boundary. The sub-block matrices  $P_{xx}$  and  $P_{xy}$  refer to the deformation along x-axis and y-axis, respectively, in response to the unit horizontal displacement at the bottom coarse

node, as shown in Fig. 3.2 (a). Similarly,  $P_{yy}$  and  $P_{yx}$  refer to the deformation along y-axis and x-axis, respectively, in response to the unit vertical displacement at the right bottom coarse node, as shown in Fig. 3.2 (b).

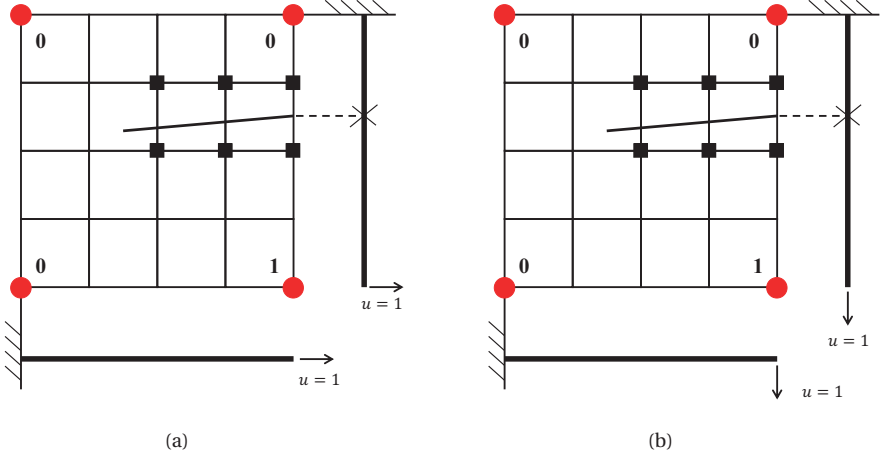


Figure 3.2: Illustration of the multiscale local basis functions constructed using XFEM for the node  $H$  in (a) x direction and (b) y direction.

Once the boundary values are found, the internal cells are solved subjected to Dirichlet values. An illustration of a basis function obtained using this algorithm is presented in Fig. 3.3. Note that the illustrated basis function captures the fracture because of the XFEM enrichment procedure.

The basis function  $N_i^H$  will be stored in column  $i$  of the prolongation operator  $P$ . Once all basis functions are found, the operator  $P$  is also known and one can proceed with the multiscale procedure as explained before.

### 3.3. ALGEBRAIC CONSTRUCTION OF BASIS FUNCTIONS

Construction of basis functions can be done by the algebraic method. To do this, the stiffness matrix needs to be reordered. The reordered system allows solving Eq. (3.6) firstly, which is composed by only boundary terms, and then the equilibrium equation Eq. (3.5) is solved. In Fig. 3.1, it is shown that all nodes in any coarse element can be split into three groups: internal, edge and vertex nodes. The fine-scale stiffness matrix  $K^h$  is permuted using the permutation operator  $T$  as

$$\begin{bmatrix} K_{II} & K_{IE} & K_{IV} \\ K_{EI} & K_{EE} & K_{EV} \\ K_{VI} & K_{VE} & K_{VV} \end{bmatrix} \begin{bmatrix} d_I \\ d_E \\ d_V \end{bmatrix} = \begin{bmatrix} f_I \\ f_E \\ f_V \end{bmatrix}. \quad (3.8)$$

Here,  $I$  represents the internal nodes,  $E$  represents the edge nodes and  $V$  represents

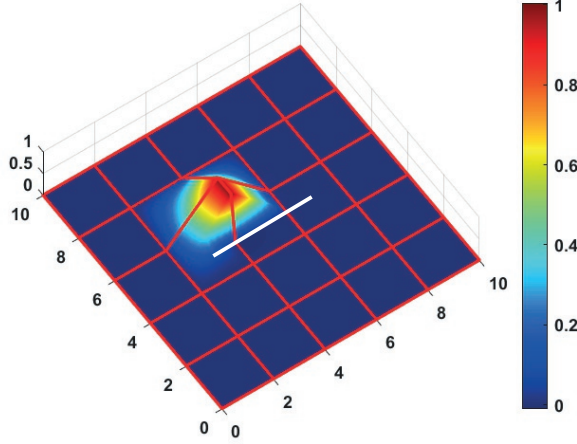


Figure 3.3: Illustration of a basis function that captures the discontinuity of a fracture. Model size is  $10[m] \times 10[m]$ . Red lines represent a  $5 \times 5$  coarse scale mesh. White segment represents the fracture extending from (3,5) to (7,5). The shown basis function belongs to the coarse node located at the coordinate (4,6).

the vertex nodes. The coarse-scale solutions can be computed based on the solutions on the vertex nodes. The functions that interpolate the solution between the vertex nodes through the edge and internal nodes are then the necessary basis functions. The reduced-dimensional boundary condition Eq. (3.6) is now being imposed by a 1D XFEM discrete system in the 2D XFEM problem. This causes the entry  $K_{EI}$  to vanish, as the connectivity between the edge and internal nodes for the edge elements is assumed to disappear. These 1D edge equations can then be expressed as

$$K_{EE}^R d_E + K_{EV}^R d_V = 0. \quad (3.9)$$

Since the solutions at vertex nodes will be obtained from the coarse-scale system, the reordered fine-scale matrix can now be reduced to

$$\begin{bmatrix} K_{II} & K_{IE} & K_{IV} \\ 0 & K_{EE}^R & K_{EV}^R \\ 0 & 0 & K^H \end{bmatrix} \begin{bmatrix} d'_I \\ d'_E \\ d'_V \end{bmatrix} = \begin{bmatrix} 0 \\ 0 \\ f^H \end{bmatrix}. \quad (3.10)$$

where the  $d'_I$ ,  $d'_E$  and  $d'_V$  are the approximated displacements solutions for the internal nodes, edge nodes and vertex nodes. Note that the equations for basis functions do not consider source terms in their right-hand-side while these are transferred to the coarse scale system. Given the coarse nodes solutions  $d'_V$ , one can obtain the solution at the edge via

$$d'_E = -(K_{EE}^R)^{-1} K_{EV}^R d'_V = \mathbf{P}_{EV} d'_V. \quad (3.11)$$

Similarly, the solution at the internal cells reads

$$\begin{aligned} d'_I &= -K_{II}^{-1} (K_{IE} d'_E + K_{IV} d'_V) \\ &= -K_{II}^{-1} (-K_{IE} (K_{EE}^R)^{-1} K_{EV}^R + K_{IV}) d'_V = \mathbf{P}_{IV} d'_V. \end{aligned} \quad (3.12)$$

Note that,  $\mathbf{P}_{EV}$  and  $\mathbf{P}_{IV}$  are the sub-matrices of the prolongation operator. The prolongation matrix is defined as follows

$$\mathbf{d}' = \begin{bmatrix} d'_I \\ d'_E \\ d'_V \end{bmatrix} = \underbrace{\begin{bmatrix} P_{IV} \\ P_{EV} \\ I_{VV} \end{bmatrix}}_{\mathbf{P}} d'_V. \quad (3.13)$$

Here,  $I_{VV}$  is the diagonal identity matrix with a size equal to the number of vertex nodes. After defining the prolongation operator algebraically, based on the entries of the 2D XFEM (for internal nodes) and 1D XFEM (for edge nodes), one can determine the multi-scale solution.

### 3.4. ITERATIVE STRATEGY

An iterative strategy is paired with MS-XFEM to improve the quality of the final solution to the desired level. In this section, the two stage iterative strategy is applied. In the first stage the low frequency errors are reduced by using multiscale operator  $M_{MS}^{-1}$ . In the second stage, a fine scale smoother,  $ILLU(0)$  for this thesis, is applied to reduce the high frequency error [80]. Note that the fine scale smoother can be applied multiple times in the second stage. The algorithm for this two stage iterative strategy is shown in the algorithm. 1.

---

#### Algorithm 1 Algorithm of two stage MS-XFEM iterative strategy

---

Construct  $M_{MS}^{-1}$  and  $M_{ILLU(0)}^{-1}$

**while**  $\|r^{v+1}\| \geq \tau$  **do**

    First stage:

        Update  $d^{v0} = d^n + M_{MS}^{-1} \cdot r^n$

        Update  $r^{v0} = f^h - K^h \cdot d^{v0}$

    Second stage:

        Initialization:  $d^v \leftarrow d^{v0}$ ,  $r^v \leftarrow r^{v0}$

**for**  $v = 1 \rightarrow n_s$  **do**

            Update  $d^{v+1} = d^v + M_{ILLU(0)}^{-1} \cdot r^v$

            Update  $r^{v+1} = f^h - K^h \cdot d^{v+1}$

**end for**

**end while**

---

## 3.5. TEST CASES

### 3.5.1. TEST CASE 1: SINGLE FRACTURE IN A HETEROGENEOUS DOMAIN

In this test case, a square 2D domain of  $L \times L$  with  $L = 10$  [m] is considered, which contains a single horizontal fracture, as shown in Fig. 3.4. The fine-scale mesh consists of  $40 \times 40$  elements, while the MS-XFEM contains only  $5 \times 5$  coarse grids. This results in a coarsening ratio of  $8 \times 8$ . The heterogeneous Young's modulus distribution is shown in Fig. 3.5 and the Poisson's ratio is constant 0.2 everywhere. The fracture tips coordinates are shown in Fig. 3.4. The Dirichlet boundary condition is set at the south face. All nodes at the bottom boundary are fixed in x and y directions. The north boundary is under distributed upward load with  $q = 5 \times 10^5$  [N/m] magnitude. The east and west boundaries are set as stress-free.

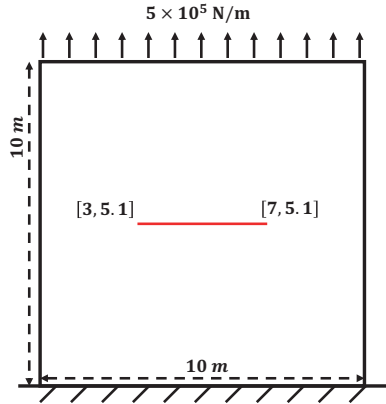


Figure 3.4: Test case 1: illustration of the model setup.

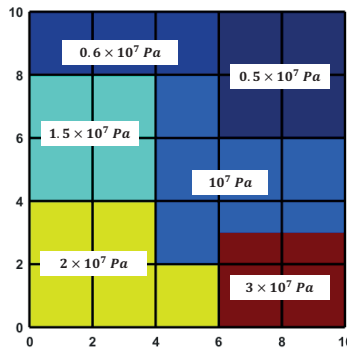


Figure 3.5: Test case 1: heterogeneous Young's modulus distribution. The black lines represent the coarse mesh.

Results are shown in Fig. 3.6. It is clear that the results of MS-XFEM on only 5 grid cells without iterative strategy is in reasonable agreement with that of the fine-scale XFEM solver using a  $40 \times 40$  mesh. Note that no extra DOFs involved in the MS-XFEM solving procedure.

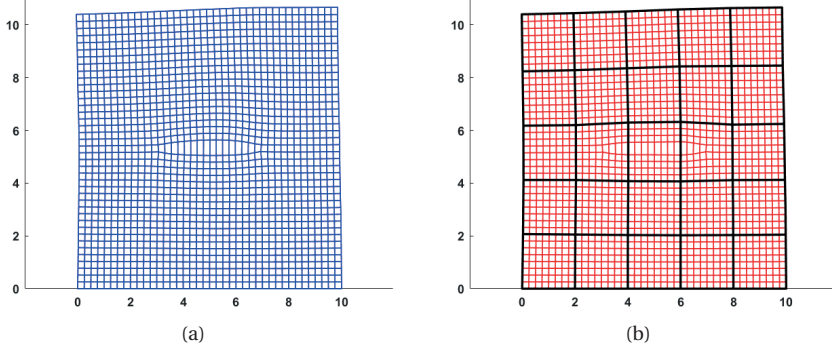


Figure 3.6: Test Case 1: displacement field for a heterogeneous fractured domain using (a) fine scale XFEM and (b) MS-XFEM without using iterative strategy. Black lines represent the coarse scale mesh.

The error in displacement field between fine-scale XFEM in Fig. 3.6 (a) and MS-XFEM solutions without iterative strategy 3.6 (b) is plotted in Fig. 3.7. Note that the zones of high errors are mainly near the fracture.

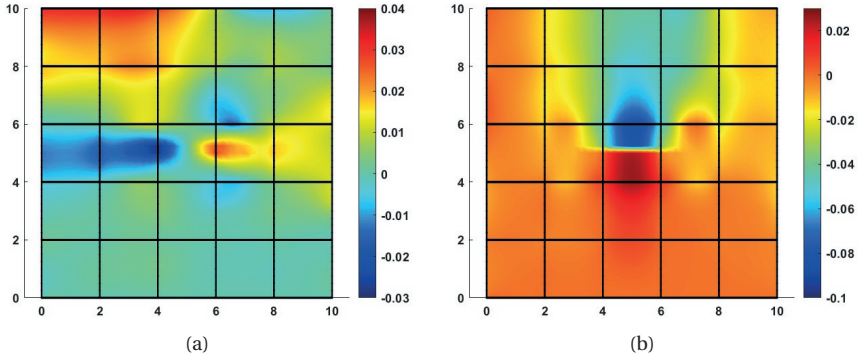


Figure 3.7: Test Case 1: displacement difference between fine scale XFEM and MS-XFEM in (a) x direction (b) y direction. Black lines represent coarse scale mesh.

The stress field  $\sigma_{yy}$ , obtained from the displacement field, is also plotted in Fig. 3.8 (a) and (b), respectively, for fine-scale XFEM and MS-XFEM without iterative strategy. Considering the fine scale XFEM solution and MS-XFEM solution without improvement by iterative strategy, it can be observed that there is still difference between Fig. 3.8 (a) and (b). A basis function for a fractured local domain is illustrated in Fig. 3.9. Note that the discontinuity is captured well by the basis functions.

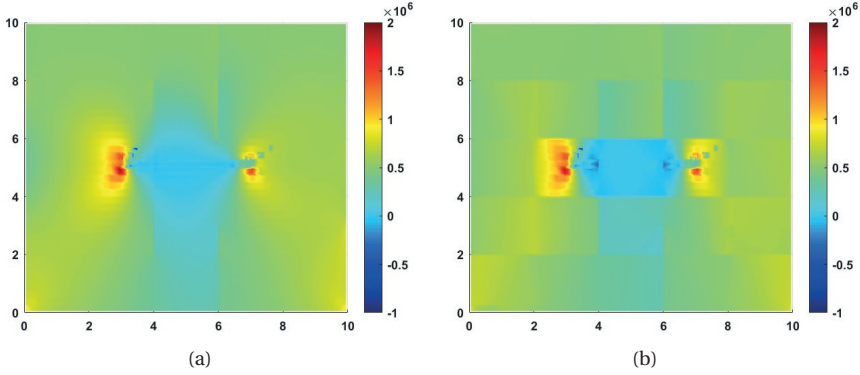


Figure 3.8: Test Case 1: stress fields computed by displacement fields of (a) fine scale XFEM and (b) MS-XFEM without iterative strategy.

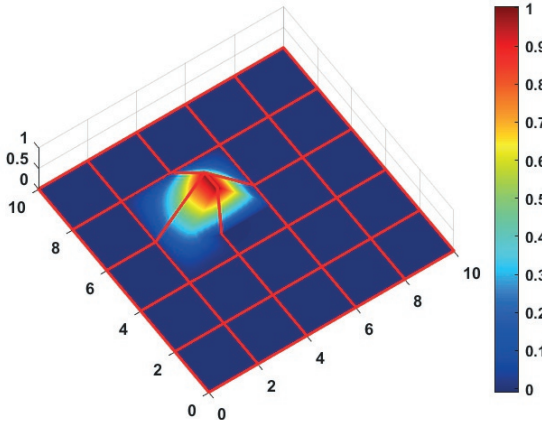


Figure 3.9: Test case 1: basis functions  $P_{xx}$  of single fracture test case. Single discontinuity is captured by axial equilibrium and transverse equilibrium solutions. This basis function is centered at coordinate (4, 6).

The coarsening ratio indicates the number of fine scale elements in each coarse element. The effect of the coarsening ratio is shown in Fig. 3.10. To do this study, the fine-scale mesh is kept constant, while the coarsening ratio is changed. This results in different coarse-scale system sizes to solve for the same fine-scale system. The normalized error  $e$  in this figure is computed as

$$e_i = \frac{\|d_{MS} - d_f\|_2}{N} \quad \forall i \in x, y, \quad (3.14)$$

where  $N$  is the number of fine-scale mesh nodes.  $d_{MS}$  and  $d_f$  denote the MS-XFEM displacement field without iterative strategy and fine-scale displacement field, respectively.

The MS-XFEM errors are due to the local boundary conditions used to calculate the ba-

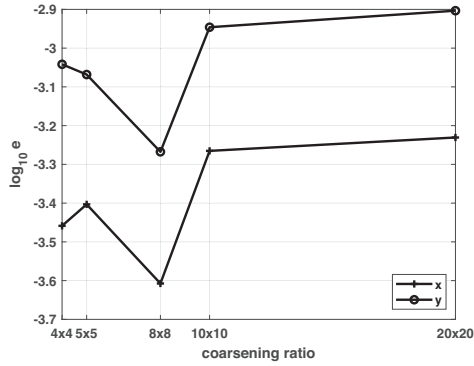


Figure 3.10: Test case 1: change of normalized errors with different coarsening ratios.

sis functions, and also because no enrichment functions are imposed at coarse scale. This means that for heterogeneous domains, there can be a finer resolution for coarse elements at which the local boundary conditions impose more errors compared with coarser resolutions. In spite of this, Fig. 3.10 shows, for this example, a decaying trend of the error with respect to the finer coarse mesh.

As discussed in section 3.4, one can pair the MS-XFEM with an iterative strategy in which the error is reduced to any desired level. To improve the results presented in Figure 3.6(b), a manual selection of only 5 outer iterations is employed for smoothing, and within the second stage of each outer loop, the fine-scale smoother is iteratively applied 5 times. Figure 3.11 illustrates a notable reduction in the error of the multiscale solution. Also as shown in Fig. 3.12, the stress fields of MS-XFEM and fine-scale XFEM match well after pairing the iterative strategy with MS-XFEM.

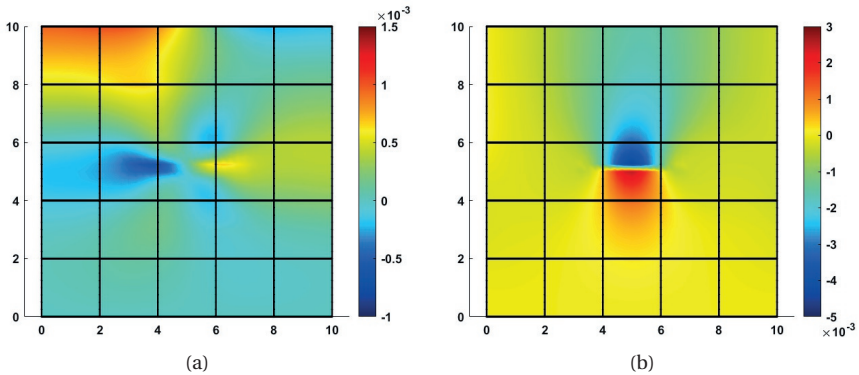


Figure 3.11: Test Case 1: displacement difference between fine scale XFEM and MS-XFEM with iterative strategy in (a) x direction (b) y direction. Black lines represent coarse scale mesh. 5 outer loops are employed, and within the second stage of each outer loop, fine-scale smoother is applied 5 times.

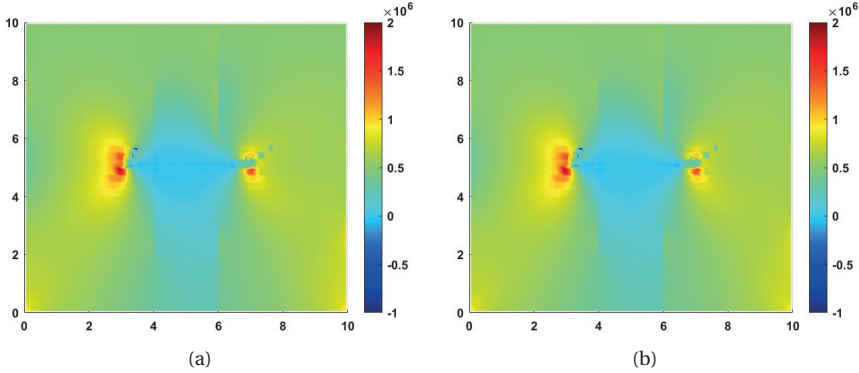


Figure 3.12: Test Case 1: stress fields computed by displacement fields of (a) fine scale XFEM and (b) MS-XFEM with iterative strategy. 5 outer loops are employed, and within the second stage of each outer loop, fine-scale smoother is applied 5 times.

The convergence history of the MS-XFEM with iterative strategy is shown in Fig. 3.13. The blue circle represents the normalized error of the result without the iterative strategy, which is the result shown in Fig. 3.6(b). The red circle represents the normalized error of the result after 5 iterations with 5 times smoother in each iteration, which is the result shown in Fig. 3.11. Different smoothing steps values  $n_s$  can be used per iteration. Clearly, one can reduce the multiscale errors to machine accuracy by applying MS-XFEM iterations. In particular, for practical applications, one can stop iterations after a few iteration counts, once the error norm falls below a certain tolerance  $\tau$ , considering the level of uncertainty within the parameters of the problem, i.e.,

$$e \leq \tau \tag{3.15}$$

here,  $\tau$  is chosen as  $10^{-10}$  to confirm that convergence can be achieved to machine accuracy. Figure 3.13 shows the convergence history for different smoothing step counts  $n_s$  per iteration.

### 3.5.2. TEST CASE 2: HETEROGENEOUS RESERVOIR WITH MULTIPLE FRACTURES

The second test case is set to model deformation in a heterogeneous reservoir with more fractures. The heterogeneous material properties of this test case are the same as those in test case 1. The fine scale mesh is again set as  $40 \times 40$  and the coarse mesh is  $5 \times 5$ . The upscale ratio is  $8 \times 8$ . Here, more fractures are considered. In addition, compared to test case 1, at the east and west boundaries distributed loads are also applied, as shown in Fig. 3.14

Simulation results for both fine-scale XFEM and MS-XFEM are shown in Fig. 3.15. It is clear that the MS-XFEM (without any iterations) result is different from than the fine-scale one in the zones of large deformations. However, considering the MS-XFEM solu-

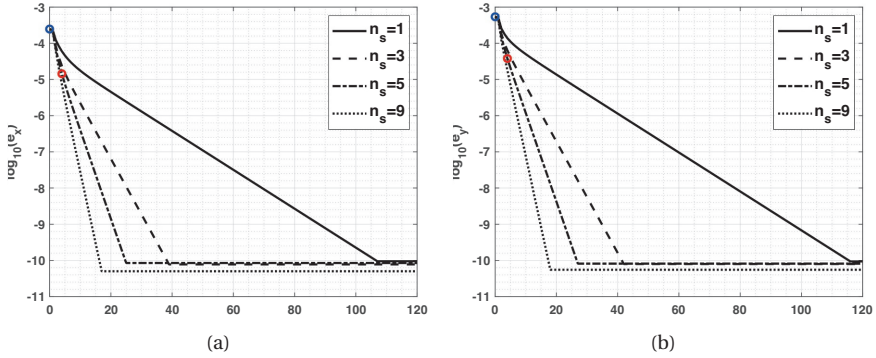


Figure 3.13: Test Case 1: iteration history of MS-XFEM procedure with different number of smoothing per step. Errors for displacement in (a) x and (b) y directions are shown. The blue and the red circles represent the normalized errors corresponding to the results shown in Fig. 3.6 (b) and Fig. 3.11, respectively.

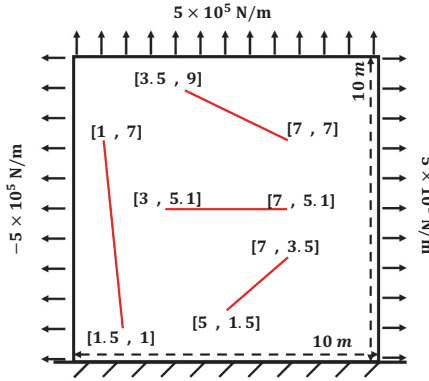


Figure 3.14: Test case 2: Multiple fractures within a heterogeneous reservoir under tension stress across three boundaries.

tion is obtained by using only  $5 \times 5$  grids without any extra DOFs, it is still an acceptable result.

The iterative strategy is applied to reduce errors. Fig. 3.16(c) and (d) present improved results compared to Fig. 3.16(a) and (b), after 10 iterations with 5 times fine-scale smoother applied in each iteration. The large deformation of the most left fracture still requires more iterations, however, the differences around the other three fractures have been decreased significantly. Note  $ILU(0)$  is used as the second stage smoother.

Stress fields for all three cases of fine-scale XFEM, MS-XFEM without iterative strategy and MS-XFEM with iterative strategy are shown in Fig. 3.17. The result of MS-XFEM with iterative strategy shown in Fig. 3.17(c) is computed based on the solutions shown in Fig. 3.16 (c) and (d). It is clear that with iterative strategy, multiscale stress distributions match with the fine-scale one.

An example of basis functions for this test case is shown in Fig. 3.18. It illustrates how

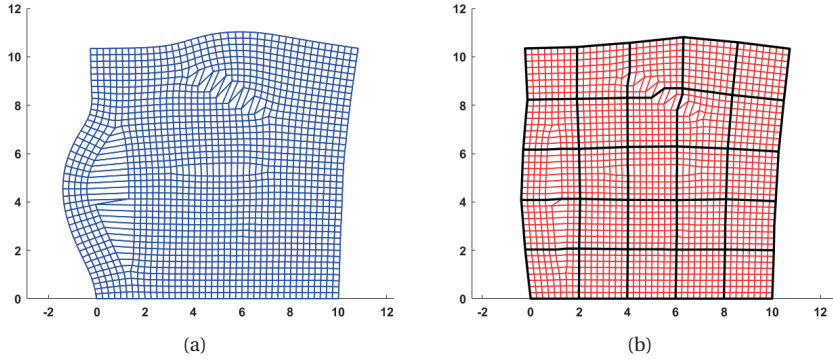


Figure 3.15: Test Case 2: displacement field for a heterogeneous fractured domain using (a) fine scale XFEM and (b) MS-XFEM without using iterative strategy. Black lines represent the coarse scale mesh.

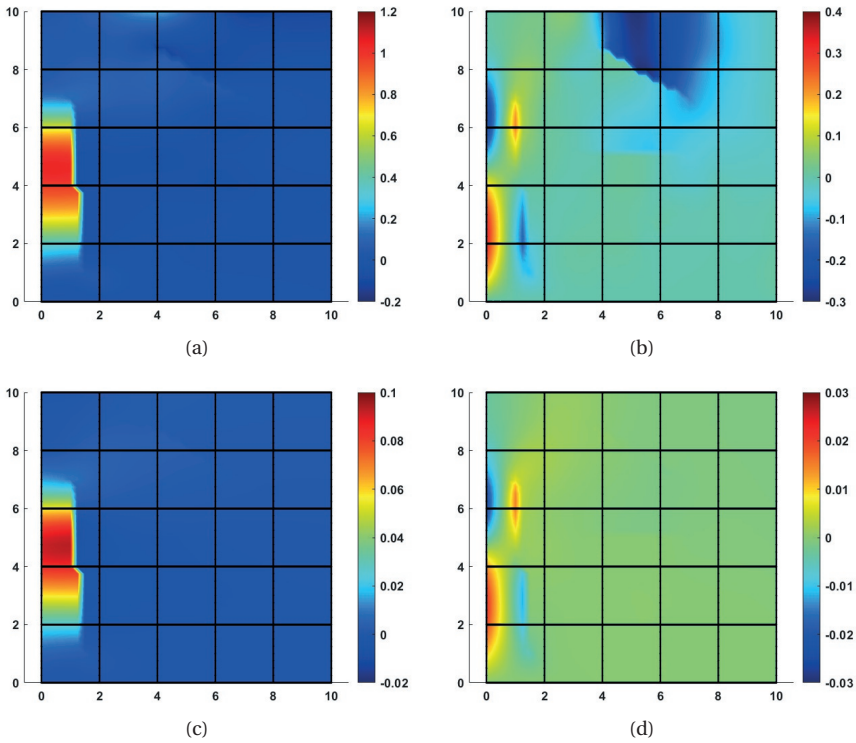


Figure 3.16: Test Case 2: displacement difference between fine scale XFEM and MS-XFEM in (a) x direction (b) y direction (c) x direction after 10 iterations (d) y direction after 10 iterations. 5 rounds of fine scale smoother are used in each iteration to compute solutions in (c) and (d). Black lines represent the coarse mesh.

two fractures are captured by the local basis functions.

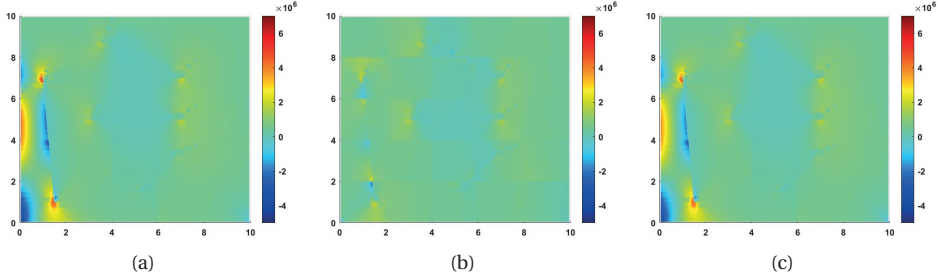


Figure 3.17: Test Case 2: stress field  $\sigma_{yy}$  comparison between (a) fine scale XFEM and (b) MS-XFEM (c) MS-XFEM after 10 iterations with 5 rounds of fine scale smoother applied in each iteration.

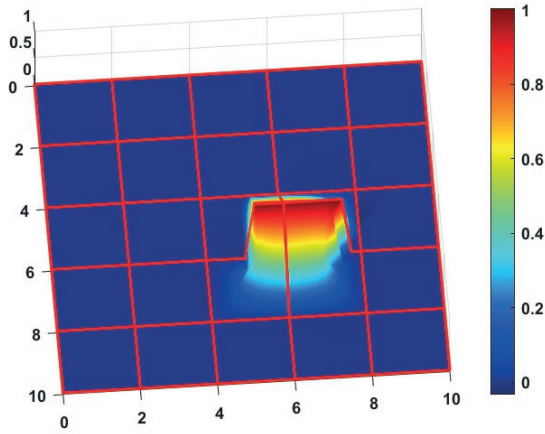


Figure 3.18: Test case 2: basis functions  $P_{xx}$  of multiple fractures test case. Multiple discontinuities are captured by axial equilibrium and transverse equilibrium solutions. This basis function is centered at coordinate (6,6).

The convergence history is shown in Fig. 3.19. The higher number of smoother applied in each iteration would result in faster convergence. However, it comes with additional computational costs. Similar as the extensive studies for multiscale simulation of flow in porous media, for deformation simulation, a CPU-based study should be performed in order to obtain the optimum combination of coarse-grid resolution, type and count of smoothing steps.

### 3.5.3. COMPUTATIONAL EFFICIENCY ANALYSIS

To provide an estimate of the computational efficiency of the proposed MS-XFEM strategy, compared with a fine-scale XFEM, an operator-cost-based analysis is presented be-

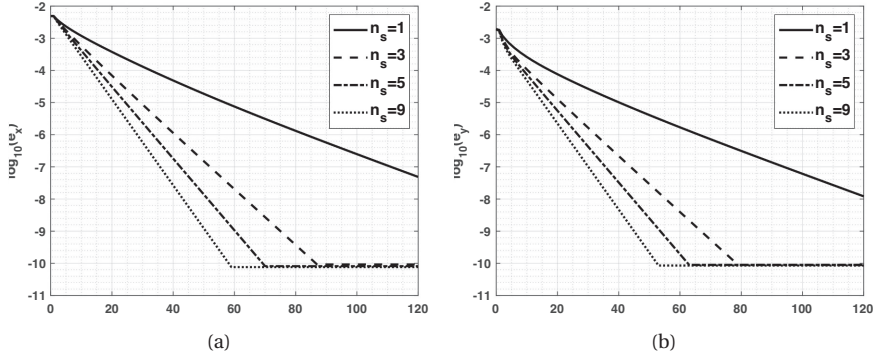


Figure 3.19: Test Case 2: convergence history of MS-XFEM procedure with different number of smoothing per step. Errors for displacement in (a)  $x$  and (b)  $y$  directions are shown.

low. Then, a scalability test with respect to the performance of error reduction strategy with increasing density of the fractures is also studied and presented.

### COMPUTATIONAL COST ANALYSIS

The approximate operation-based approach builds on the assumption that solving a linear system of size  $\zeta$  costs  $O(\zeta^m)$  operations, i.e.,  $C = \alpha\zeta^m$ , where  $C$  is the cost function. As such, the approximate cost function for a fine-scale XFEM system (i.e.,  $C_f$ ) with  $N_f$  nodes is

$$C_f = \alpha(2N_f + \psi)^m. \quad (3.16)$$

Here,  $\psi$  represents the number of extra DOFs due to XFEM enrichment. Also, since there are  $x$  and  $y$  displacement directions for each node, a factor 2 is used.

MS-XFEM provides an approximate solution to the fine-scale system in a procedure that includes three main steps: (1) calculate basis function, (2) solve coarse scale system, and (3) iteratively improve the results. Consider a coarsening ratio of  $\Gamma$ , thus, the coarse grid size  $N_c$  is

$$N_c = \frac{N_f}{\Gamma}. \quad (3.17)$$

If one assumes  $\gamma$  number of extra DOFs per each basis function, the basis functions for each coarse node of one coarse element costs

$$C_{basis} = 2 \times \alpha(\Gamma + \gamma)^m, \quad (3.18)$$

where factor 2 represents twice the computation of basis functions in  $x$  and  $y$  direction, as shown in Fig. 3.2. The coarse scale system entails no extra DOFs due to enrichment. As such, its cost  $C_c$  can be approximated as

$$C_c = \alpha(2N_c)^m = \alpha\left(2 \times \frac{N_f}{\Gamma}\right)^m. \quad (3.19)$$

Again, factor 2 is for the 2D (x,y) unknowns. The cost of the linear smoother  $ILLU(0)$  is approximated by setting  $m = 1$  and a constant is  $\beta$ , i.e.,

$$C_{smooth} = n_s \times (\beta \times (2N_f))^1, \quad (3.20)$$

where  $n_s$  is the number of smoothing steps per iteration. If no iterative strategy is applied, then, the MS-XFEM computational cost  $C_{MS}$  can be approximated as

$$C_{MS} = N_c(2\alpha(\Gamma + \gamma)^m) + \alpha(2N_c)^m, \quad (3.21)$$

If the iterative strategy is applied  $N_{it}$  times, then the MS-XFEM computational cost  $C_{MSi}$  can be approximated as

$$C_{MSi} = C_{MS} + N_{it} \left( \underbrace{\alpha(2N_c)^m}_{C_c} + \underbrace{n_s(\beta \times (2N_f))}_{C_{smooth}} \right). \quad (3.22)$$

Note that if  $N_{it} = 0$ , the cost function  $C_{MSi}$  becomes identical to  $C_{MS}$ . The cost ratio  $\phi$  is now introduced as the cost ratio between MS-XFEM and fine-scale XFEM, i.e.,

$$\phi = \frac{C_{MSi}}{C_f}. \quad (3.23)$$

To provide a better sense, two tests with different fine scale grid numbers of  $N_f = 10^4$  and  $N_f = 10^8$  are considered. For the case with  $N_f = 10^4$ , coarsening ratios of  $\Gamma \in \{2 \times 2, 5 \times 5, 10 \times 10, 20 \times 20, 50 \times 50\}$  are considered, while for the case with  $N_f = 10^8$ ,  $\Gamma \in \{10 \times 10, 20 \times 20, 50 \times 50, 100 \times 100, 1000 \times 1000\}$  are employed. It is assumed that  $\alpha/\beta = 1$ , meaning the scalability factor of the smoother is close to a linear solver. In addition,  $m = 1.3$  as the exponent of linear solver computational complexity. The same factor was used in literature [89]. Furthermore, extra DOFs due to enrichment are considered to be 10% of fine-scale grid cells, i.e.,  $\psi = 0.1N_f$ . The basis functions are then considered to have these extra DOFs equally distributed, which leads to  $\gamma \approx \frac{\psi}{N_c}$ . With these settings, one can study the overall approximate cost ratio of the proposed MS-XFEM, based on an operational-based analysis. For the MS-XFEM with no iterative strategy, MS-XFEM with  $N_{it} = 2$  and  $N_{it} = 5$  are considered. For both cases where the iterative strategy is applied in MS-XFEM, the number of smoothing steps per iteration ( $n_s$ ) is set to 8. The cost ratio  $\phi$  for all tests are plotted in Fig. 3.20.

From Fig. 3.20, it is clear that the MS-XFEM provides a significant speedup compared with the fine-scale XFEM when the problem size is large. Also, from the presented operational-based analyses, one can consider an optimum coarsening ratio, in which the multiscale procedure would perform optimal. Note that, similar as for multiphase flow simulations, a CPU-based analysis is needed to draw a more conclusive statement about the real speedup of the MS-XFEM in the future.

### SCALABILITY TEST

In this test the effect of the density of fractures on the convergence rate of the MS-XFEM is investigated. This is specially relevant to geoscientific applications. A fixed domain

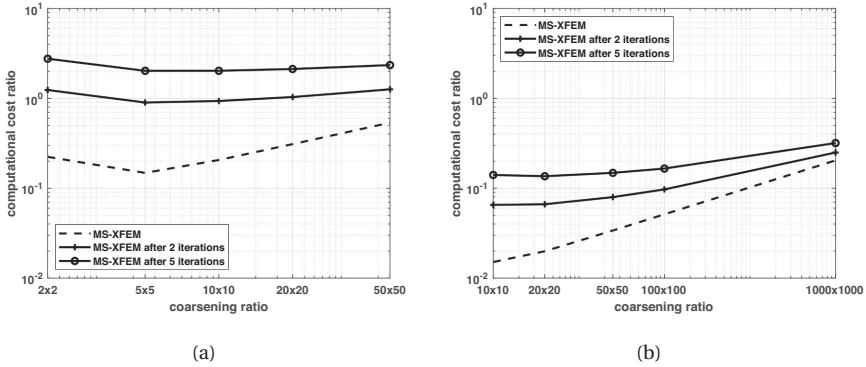


Figure 3.20: Cost ratios for different coarsening ratios and different iteration numbers for fine-scale grid of (a)  $N_f = 10^4$  and (b)  $N_f = 10^8$ . The extra DOFs due to XFEM enrichment is  $\psi = 0.1N_f$  is  $10^7$ . For both cases the number of smoothing steps per iteration is set to  $n_s = 8$ .

size of 10 [m]  $\times$  10 [m] is considered. Fine and coarse grids are  $40 \times 40$  and 5, respectively. As shown in Fig. 3.21, starting from phase F1 to phase F7 one fracture is added in the domain. For convenience, a homogeneous Young's modulus of  $E = 10^7$  [Pa] and a Poisson's ratio of 0.2 are considered. The boundary conditions are the same as in test case 2.

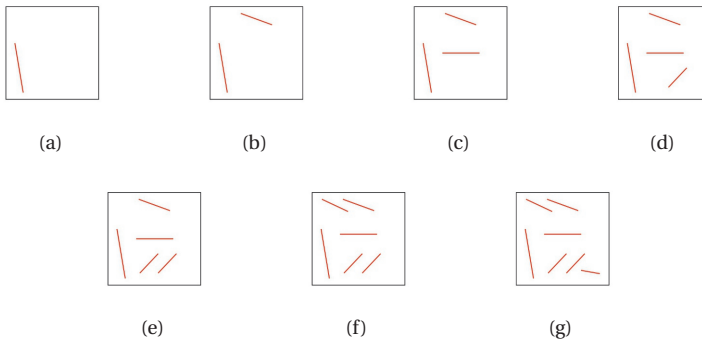


Figure 3.21: Illustration of the increasing fracture density from phase F1 to F7, with extra DOFs of 94, 132, 192, 262, 300, 366, 404, respectively, for F1 to F7.

As it can be seen in Fig. 3.22, the convergence rate of the developed MS-XFEM is not much affected by the increasing fracture density. This is because there are no extra DOFs on the coarse scale in computational process of MS-XFEM. This proof-of-concept analysis indicates the applicability of the devised method for real-field applications.

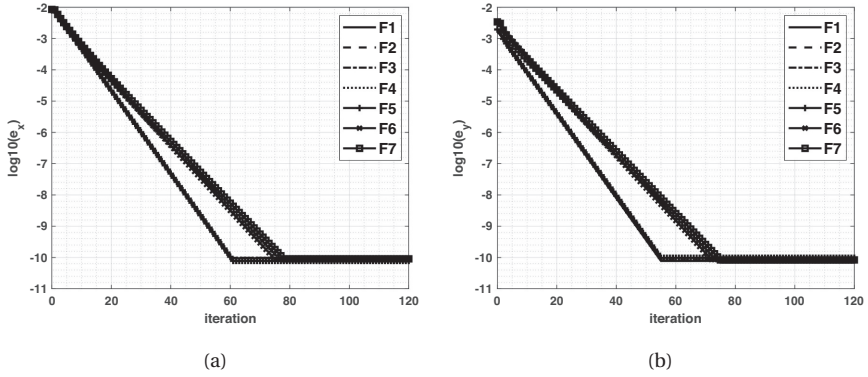


Figure 3.22: Iteration history of MS-XFEM procedure with different numbers of extra DOFs per step for displacement in x (a) and y (b) directions. F1 to F7 phases represent the increasing fracture density as shown in Fig. 3.21.

### 3.6. CONCLUSIONS

A multiscale procedure for XFEM is proposed to model deformations of geological heterogeneous fractured fields. The method resolves the discontinuities through local multiscale basis functions, which are computed using XFEM subjected to local boundary conditions. The coarse-scale system is obtained by using the basis functions, algebraically, which does not have extra DOFs, in contrast to the local basis function systems. This procedure makes the MS-XFEM very efficient. Also, by combining it with a fine-scale smoother, an iterative MS-XFEM procedure has been developed, which allows to reduce the error to any desired level of accuracy. Through an iterative procedure, only the coarse-scale system and smoothing steps are repeated.

Two heterogeneous test cases were studied as proof-of-concept, to investigate the performance of the MS-XFEM. It was shown that MS-XFEM results in acceptable solutions, when no iterations are imposed. By applying iterations, one can further improve the results. For practical applications, when parameters are uncertain, only a few iterations can be applied to maintain (and control) the MS-XFEM quality of the solution. The operational-based computational speedup indicated that the developed multiscale procedure is promising for real-field applications. Nevertheless, the MS-XFEM framework introduced in this chapter requires additional validation against analytical solutions, such as Sneddon's problem for fracture deformation [90].

# 4

## MS-XFEM FOR FRACTURE PROPAGATION

This chapter extends the application of MS-XFEM to simulate fractures' growth in highly fractured formations. Criteria for simulating propagating fractures are introduced in both Section 2.3 and Section 2.4. The growing fracture tips are tracked by updating basis functions, which are generated based on a revised fine-scale stiffness matrix in an algebraic manner. Consequently, basis functions are updated exclusively within the local domains where fracture geometry changes in each time step. Importantly, this process does not introduce any extra DOFs to the coarse-scale system. To ensure the accuracy of final results, preconditioned GMRES is employed to iteratively improve the quality of the final solution. Test cases are presented to illustrate applicability of the developed method.

### 4.1. MS-XFEM ON FRACTURE PROPAGATION

The propagation of fracture tips will change the geometries of fine-scale discontinuities and these changes should be captured by the basis functions in MS-XFEM, as shown in Fig. 4.1. To be able to use MS-XFEM to simulate the fracture propagation, basis functions need to be updated during each growth step. Note that it is not necessary to update the basis functions matrix globally since the fracture tips growth only affect the local coarse elements that contain the growing fracture tips or will contain the fracture tips after a propagation step [92].

Update of basis functions is straightforward with the algebraic method. In each growth step, the basis functions matrix is updated locally only on those coarse elements that are affected by the growing fracture tips. This is done by extracting the terms of the updated

---

This chapter is based on the publication: Xu, F., Hajibeygi, H., & Sluys, L. J. (2023). Adaptive multiscale extended finite element method (MS-XFEM) for the simulation of multiple fractures propagation in geological formations. *Journal of Computational Physics*, 486, 112114. [91]

$K_f$  matrix and reconstructing the local basis functions matrix  $P_l$  and reassemble  $P_l$  into global  $P$  matrix. Preconditioned GMRES [79] is used here to control the error and reduce it to a desired tolerance. A fine smoother  $\mathbf{M}_{sm}^{-1}$  (usually chosen as  $ILLU(0)$ ) is paired with the multiscale operator  $\mathbf{M}_{MS}^{-1}$ . The preconditioner used here involves the multiscale operator and the fine scale smoothing operator following

$$\mathbf{M}^{-1} = \mathbf{M}_{MS}^{-1} + \mathbf{M}_{sm}^{-1}(I - K^h \mathbf{M}_{MS}^{-1}). \quad (4.1)$$

The system in Eq.(3.4) is then iteratively solved using preconditioned GMRES until the error is reduced to the desired tolerance. Algorithm. 2 shows the procedure how to use MS-XFEM to simulate fractures propagation. When multiple fractures grow and cross

---

**Algorithm 2** Algorithm of MS-XFEM in fracture growth

---

**while** Set of growing tips,  $N_{grow}$ , is not empty **do**  
  Update stiffness matrix  $K^h$   
  Update  $\mathbf{P}$  locally  
  Update the MS-XFEM solutions:  $d_{MS}^h$  iteratively  
  Compute the  $N_{grow}$  using double virtual incremental method  
  Compute the growing angle  $\theta$   
  Update level sets functions:  $\psi^t \rightarrow \psi^{t+1}$ ,  $\phi^t \rightarrow \phi^{t+1}$   
  Update fracture tip positions and enrichment  
**end while**

---

each other, it is reasonable to apply adaptive local refinement around the crossing points or the fracture tips. This will improve the quality of the MS-XFEM results. A strategy such as ADM (adaptive dynamic multilevel) is a good option to be applied [93]. Currently, these are not used in this thesis.

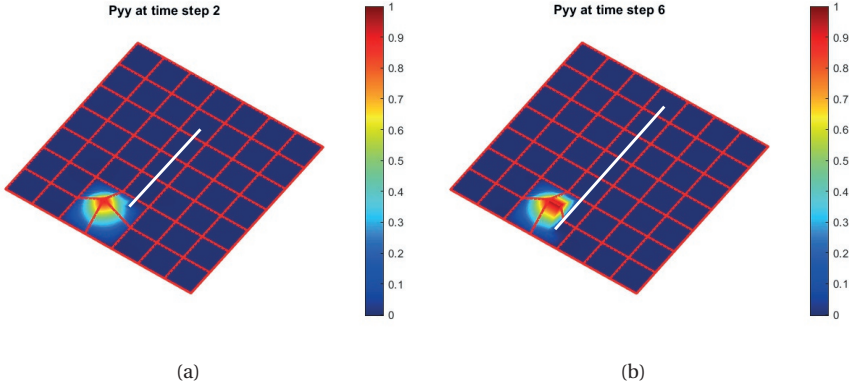


Figure 4.1: An example of updating the basis functions that captures the fracture growth from (a) step 2 to (b) step 6. The white segment represents the fracture.

## 4.2. NUMERICAL TEST CASES

In this section two test cases have been performed to investigate the applicability of the MS-XFEM in simulation of single and multiple fractures propagation. For all test cases, a square 2D domain of  $10 \text{ [m]} \times 10 \text{ [m]}$  is considered. The material of both test cases is homogeneous sandstone with a Young's modulus  $E = 25 \text{ [GPa]}$  and Poisson's ratio of 0.2. The fracture toughness of sandstone  $K_c = 1.4 \times 10^6 \text{ [Pa} \cdot \text{m}^{-\frac{1}{2}}]$  [94, 95]. The fine scale mesh is set as  $49 \times 49$  and the coarse mesh is  $7 \times 7$  for both test cases in this chapter. This results in a coarsening ratio of  $7 \times 7$  in both x and y directions.

Both test cases are simulated using the MS-XFEM and are compared with the fine scale results to check accuracy. To illustrate the importance of the iterative strategy on quality control, the result computed without using the iterative strategy is shown. Also the result computed using preconditioned GMRES is shown. The criterion to stop the iterations is set when the norm of the residual  $\|r^n\|_2$  at the current time step  $t^n$  is less than  $\tau$  of the original residual norm  $\|r^0\|_2$

$$\frac{\|r^n\|_2}{\|r^0\|_2} \leq \tau. \quad (4.2)$$

The tolerance input is affecting the number of iterations required to reach convergence. In this paper, two different tolerance values,  $\tau = 10^{-8}$  and  $\tau = 10^{-2}$ , are applied. It is essential to observe how much improvement the iterative strategy can bring since this strategy will add extra computational burden. Normally there is no doubt that a tolerance of  $\tau = 10^{-8}$  would give very accurate MS-XFEM solutions but it is also valuable to analyze whether less accurate solutions ( $\tau = 10^{-2}$ ) are acceptable since this less accurate solution has less computational burden.

### 4.2.1. TEST CASE 1: HOMOGENEOUS SANDSTONE WITH SINGLE FRACTURE

A single horizontal fracture test case as shown in Fig. 4.2 is simulated. The fracture tip coordinates are shown in Fig. 4.2. The Dirichlet boundary conditions are applied at the bottom. The left-bottom corner is fixed in both x and y directions while the rest of the nodes at the bottom boundary are fixed only in y direction. At the top boundary, a distributed upward loading  $q = 10^9 \text{ [N/m]}$  is applied. The left and right boundaries are set as stress free. The total time that the fractures are allowed to grow is 7 [s], and each time step is 1 [s]. In each step the length of the fracture increment is constant 0.4 [m].

Results for the displacement field without iterative strategy (Fig. 4.3(a)) and with the iterative strategy using an accuracy tolerance of  $\tau = 10^{-2}$  (Fig. 4.3(b)) at the end of time step 4 are shown. The result for tolerance  $\tau = 10^{-8}$  is not shown since it is nearly identical to the fine scale solution. Both MS-XFEM results (red color lines represent the coarse  $7 \times 7$  mesh) are plotted on top of the fine scale XFEM result (blue color using the  $49 \times 49$  mesh) in order to compare them.

Without the assistance of preconditioned GMRES, there is an obvious difference between the MS-XFEM solution compared to the fine scale solution in Fig. 4.3 (a). The maximum difference between the displacements solutions is 0.22 [m]. This result properly captures the opening of the fracture. The MS-XFEM result with error tolerance  $\tau = 10^{-2}$  is very close to the fine scale XFEM result. The number of iterations required for

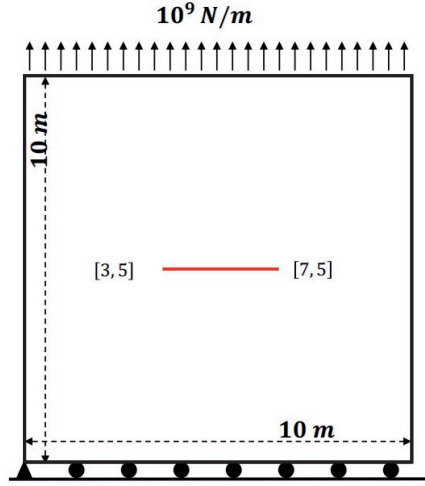


Figure 4.2: Test case 1: illustration of the model setup.

Fig. 4.3 (b) is 11 while the iterations for obtaining the solution with tolerance  $\tau = 10^{-8}$  is 34 which implies more computational costs.

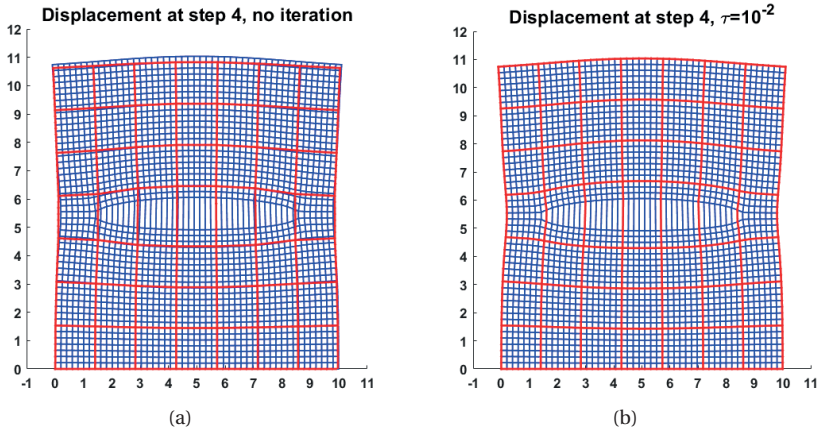


Figure 4.3: Test Case 1: displacement field at time step 4 using (a) no iterative strategy and (b) tolerance  $\tau = 10^{-2}$  with 11 iterations to reach convergence. Red lines represent the coarse scale mesh with MS-XFEM displacement field plotted on coarse scale grid. Blue lines represent the fine scale mesh with fine scale solution plotted on fine scale grid.

The crack path from initial step to final step is tracked and at time step 4 and 6 the crack patterns are plotted in Fig. 4.4. The crack angle is computed using Eq. (2.29). The two crack paths are computed using the MS-XFEM displacement solutions that are

computed without iterative strategy and with the iterative strategy using the tolerance of  $\tau = 10^{-2}$ . These two crack paths are both compared with the crack path computed based on the fine scale displacement field. Note that the crack paths predicted using fine scale XFEM solutions are plotted in blue color. It is clear that even the original MS-XFEM without iterative improvement still yields an accurate crack path considering that this is a pure mode *I* problem with a single fracture. For complicated fracture systems, as for the next test case, this may not be the case.

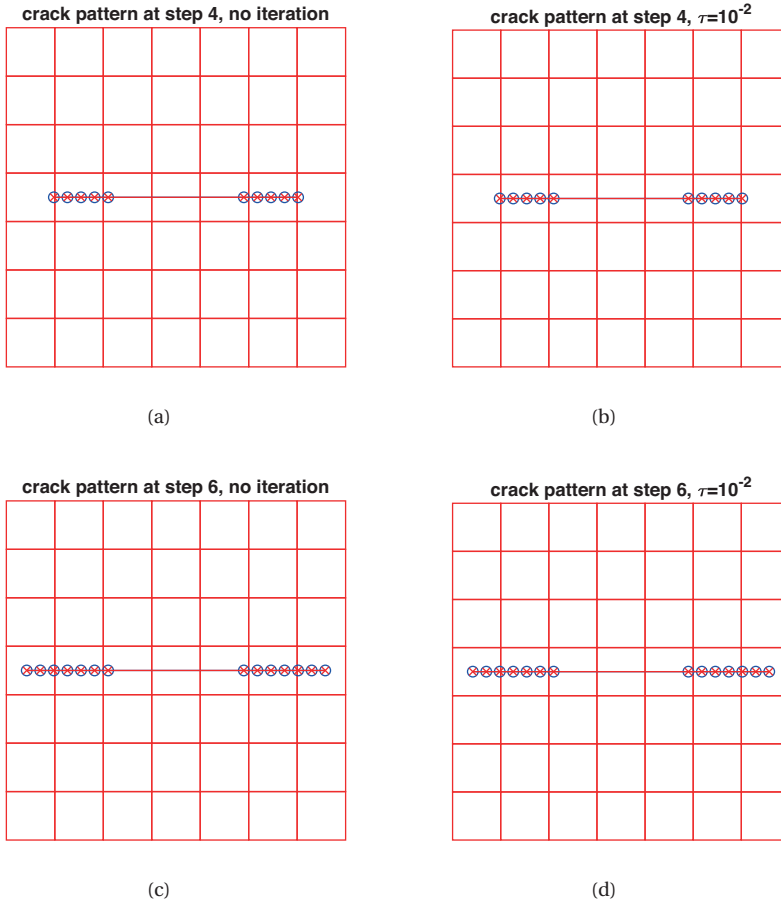


Figure 4.4: Test case 1: fracture propagation path at step 4 (top) and 6 (bottom). Red lines represent the coarse scale mesh. Blue segments and blue circles represent the fine scale fracture path while red segments and red crosses represent the path predicted using MS-XFEM. The left column includes the paths predicted using MS-XFEM without iterations. The right column includes the paths predicted using MS-XFEM with tolerance of  $10^{-2}$ .

The convergence characteristics at step 2, 4 and 6 using preconditioned GMRES are shown in Fig. 4.5. The number of extra DOFs involved in these three steps are: 112,

144 and 176, respectively. The number of iterations to reach convergence with respect to a tolerance of  $10^{-8}$  of these three steps are: 32, 34 and 36. Thus the iterations required to reach convergence is slightly increasing with the growth of fractures. This is reasonable since growing fractures increase the number of extra DOFs.

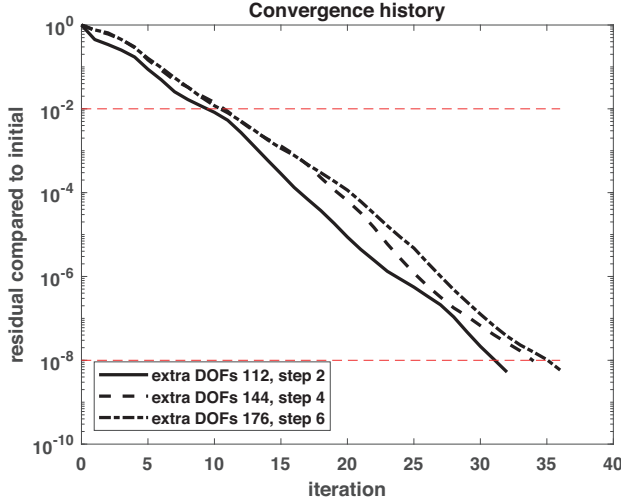


Figure 4.5: Test case 1: convergence history at step 2, 4 and 6 using preconditioned GMRES. The corresponding extra DOFs are: 112, 144 and 176. The number of iterations to reach convergence is increasing as the fracture is growing.

#### 4.2.2. TEST CASE 2: HOMOGENEOUS SANDSTONE WITH MULTIPLE FRACTURES

A second test case is used to test the application of MS-XFEM in the simulation of multiple fractures propagation. The fractures setup is shown in Fig. 4.6. The fractures are rotated around its center point (marked with red circle). The coordinates of center points of each fracture and the rotation angles are shown in brackets. The four fractures been labeled with a number from 1 to 4. The initial length of each fracture is 1 [m]. The total time that a fracture can grow is set as 17 [s] and each time step size is 1 [s]. The fracture increment is set as 0.4 [m] per time step with grid size of 0.2 [m]  $\times$  0.2 [m]. The Dirichlet boundary conditions are applied at the bottom. The bottom center point is fixed in both  $x$  and  $y$  directions while the rest of the nodes along the bottom boundary are fixed in  $y$  direction. At the top a distributed upward loading  $q = 10^7$  [N/m] is applied. The left and right boundaries are set as stress free.

If no GMRES is used to control the error level of final solutions, the MS-XFEM fails to predict the crack path as shown in Fig. 4.7. This suggests that the errors accumulated in highly fractured systems will become too significant to ignore them and thus the iterative strategy is necessary to be paired with MS-XFEM. In the following, only the test case

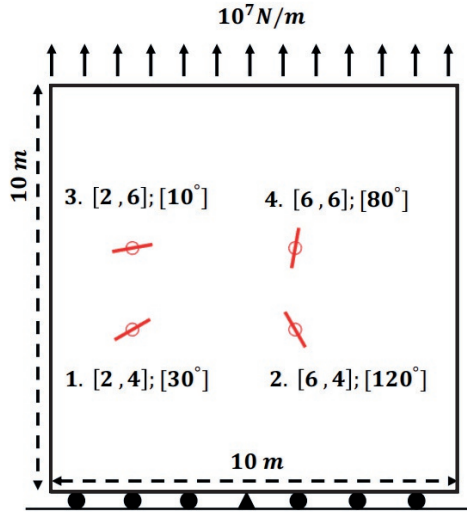


Figure 4.6: Test case 2: Multiple fractures within a homogeneous sandstone sample under tension.

using GMRES with tolerance of  $\tau = 10^{-2}$  is studied. Note that  $\tau = 10^{-2}$  is much bigger than the machine accuracy and it is set to iterate only a few times to maintain high efficiency of the method.

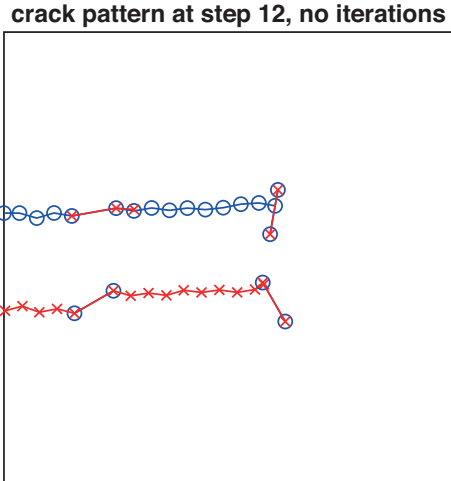


Figure 4.7: Test case 2: crack pattern predicted at step 12. The blue curve represents the crack path predicted using only the fine scale solution and the red curves represent the incorrect crack paths predicted using the MS-XFEM solution.

The propagation crack path at step 4, 10 and 15 are shown in the upper row of Fig. 4.8. It is clear that not all tips will grow considering the global minimum energy release by Eq. (2.28). Since the preconditioned GMRES is applied, displacement field solutions from MS-XFEM are close to the fine scale XFEM solution, which is shown in the bottom row of Fig. 4.8. However, there is a still small difference between the predicted crack pattern in step 15, which is shown in the top right part of Fig. 4.8 (c). This is due to the tolerance  $\tau = 10^{-2}$  given in here. When the tolerance is set as small as  $\tau = 10^{-8}$ , the accuracy of the MS-XFEM result is very high as shown in Fig. 4.9. But the number of iterations required to reach  $\tau = 10^{-8}$  is 53 while it only requires 28 iterations to reach  $\tau = 10^{-2}$ . Considering the less computational burden, the result of Fig. 4.8 (c) is still considered as a good prediction.

The stress plots are shown in the lower row of Fig. 4.8, which partly reveals why some tips grow and others do not. The sequence of propagating crack tips is as follows. First, both the two tips of fracture 3 grow since the maximum stress is located around both tips of fracture 3, as shown in Fig. 4.8 (d). At step 9, the left tip of fracture 3 reaches at the left edge of domain. Then the right tip of fracture 3 propagates since the maximum stress surrounds this tip as shown in 4.8 (e). At step 12, the right tip of the fracture 3 grows and joins fracture 4. After that, the top fracture tip of fracture 4 continues to grow, which is represented in Fig. 4.8 (f) since the top fracture tip is located in the peak stress area.

The convergence characteristics, recorded using preconditioned GMRES, are shown in Fig. 4.10. In this figure, the convergence at step 4, 10 and 15 are plotted. The number of extra DOFs for each of these steps, respectively, are: 136, 192 and 248. The number of iterations required to reach convergence with respect to the tolerance of  $10^{-8}$  are: 38, 46 and 53, respectively. Clearly, the number of iterations required to reach convergence is increasing as the fractures grow.

### 4.3. CONCLUSION

An adaptive multiscale method for XFEM, referred to as MS-XFEM, is introduced to model the propagation of multiple fractures within geological formations. As fractures expand, they propagate and may merge, resulting in the development of discontinuities. The basis functions within MS-XFEM are designed to effectively account for this extension and junction of fine-scale fractures. These basis functions undergo algebraic updates that align with changes in the fine-scale stiffness matrix, adjusted in response to fracture growth. This feature equips MS-XFEM with the right tools for simulating fracture propagation. Employing preconditioned GMRES ensures the accuracy of the displacement field results, guaranteeing the accurate prediction of fracture growth in subsequent steps. Test case results demonstrate that MS-XFEM, in conjunction with preconditioned GMRES, effectively traces the paths of fracture growth, even with a moderate error tolerance. This indicates the successful adaptation of the basis functions to capture changes in these fractures. Further validation work against analytical solutions is necessary to enhance the effectiveness of this MS-XFEM framework in simulating fracture propagation [96, 97].

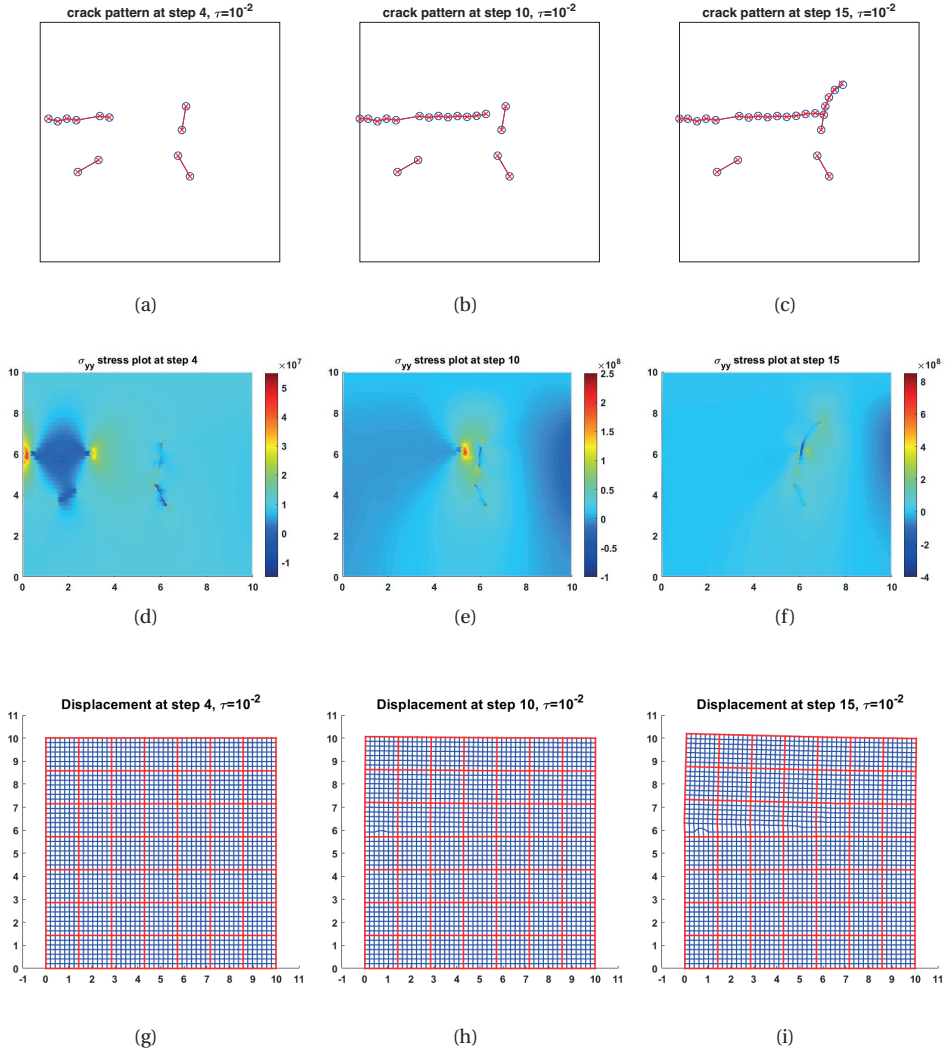


Figure 4.8: Test case 2: crack paths growing history at step 4, 10 and 15. Upper row includes crack patterns predicted. Red segments and crosses represent crack paths predicted using MS-XFEM result and blue segments and circles represent the crack paths predicted using fine scale XFEM result. The middle row includes the stress plot of  $\sigma_{yy}$  at these steps. The bottom row includes the displacement field solutions by fine scale XFEM (blue) and MS-XFEM (red).

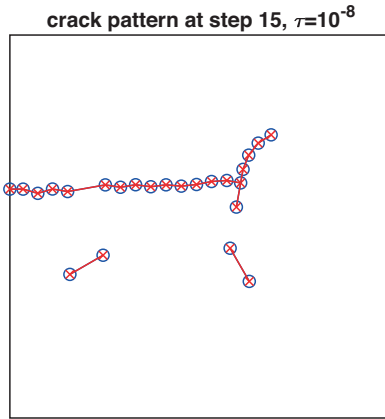


Figure 4.9: Test case 2: crack pattern predicted at step 15 using tolerance value of  $10^{-8}$ . The blue curve represents the crack path predicted using only the fine scale solution and the red curves represent the correct crack paths predicted using MS-XFEM solution. 53 iterations required to reach this accuracy while only 28 iterations required to reach  $\tau = 10^{-2}$ .

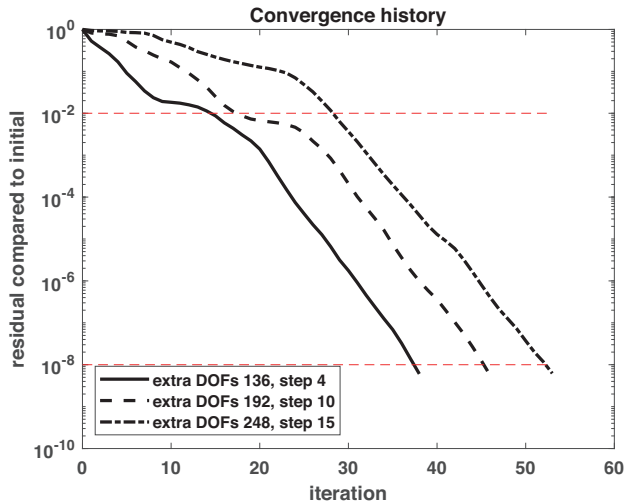


Figure 4.10: Test case 2: convergence history using preconditioned GMRES. The number of extra DOFs at steps 4, 10 and 15, respectively, are: 136, 192 and 248. The number of iterations to reach convergence increase with the growth of fractures.

# 5

## MS-XFEM FOR DEFORMATION UNDER COMPRESSION FORCES

This chapter extends the application of MS-XFEM to simulate the contact and frictional behavior of fractures subjected to external compressive loading. The penalty method is employed to prevent overlap between the two sides of fractures. The stick-slip condition along the tangential direction of fractures is determined using Coulomb's law of friction. Within MS-XFEM, basis functions are generated based on the fine-scale stiffness matrix, excluding the penalty matrix to avoid unnecessary computational overhead. The algebraic construction strategy for the basis function matrix remains consistent with the one detailed in Chapter 3. Test cases provide empirical evidence of the MS-XFEM's capacity to accurately and efficiently simulate fractures' contact and frictional sliding behavior.

### 5.1. MS-XFEM BASIS FUNCTIONS FOR COMPRESSIVE FORCES

In this thesis, for the simulation of self-contact fractures, the construction of basis functions is determined to rely on the fine-scale stiffness matrix without the inclusion of the penalty matrix. It might seem intuitive to base the basis functions on the  $K^P$  matrix as presented in Eq. (2.49). However, the iterative updating of  $K^P$  due to changes in the stick-slip conditions implies a corresponding iterative update of the basis function values. This would introduce additional computational expenses. A computationally more efficient approach is to construct the basis functions in a manner consistent with the algebraic method introduced in Chapter 3, which involves operating on the original fine-scale  $K^h$  matrix instead of  $K^P$ . Consequently, the coarse-scale stiffness matrix  $K_C$  is constructed by

$$K_C = R \cdot K^P \cdot P, \quad (5.1)$$

where,  $K^P$  is the stiffness matrix that contains the contact matrix  $K_{con}$ .

In contrast to pure mode I loading, which causes fractures to open, compression loading leads to a continuity of displacements in normal direction of fractures. However, this

does not imply that the basis functions associated with the fractured coarse elements should be continuous. For instance, slip events along fractures still indicate a discontinuity along the two sides of the fractures. Therefore, the original basis functions remain physically meaningful and applicable in this context.

## 5.2. MS-XFEM ALGORITHM FOR COMPRESSIVE FORCES

The algorithm for applying MS-XFEM for the simulation of contact and frictional slip of fractures is shown in algorithm. 3. Two standard convergence conditions are involved in this thesis. The first convergence condition is the residual control condition

$$\frac{\|r^{\nu+1}\|}{\|r_0\|} \leq \tau_r, \quad (5.2)$$

and the second one is the displacement incremental control criterion

$$\frac{\|\Delta d^{\nu+1}\|}{\|d^\nu\|} \leq \tau_d. \quad (5.3)$$

The result is considered acceptable if either of these two criteria is met.

---

**Algorithm 3** Algorithm for applying MS-XFEM to the simulation of contact and frictional sliding of fractures

---

Construct fine scale  $K^h$  and basis functions  $P$  for iteration  $\nu$

**while**  $\frac{\|r^{\nu+1}\|}{\|r_0\|} \geq \tau_r$  or  $\frac{\|\Delta d^{\nu+1}\|}{\|d^\nu\|} \geq \tau_d$  **do**

    Update  $K^{\nu\nu} = K^h + K_c^\nu$

    Solve using MS-XFEM with preconditioned GMRES until convergence

    Update  $d^{\nu+1} = d^\nu + \Delta d^{\nu+1}$

    Update  $r^{\nu+1} = f^h - f_c - K^h \cdot d^{\nu+1}$

    Update stick and slip conditions at each Gauss point

**end while**

---

## 5.3. TEST CASES

In this section, three test cases demonstrating the applicability of MS-XFEM for simulating fractures under compressive loading are presented. Two convergence tolerance values,  $\tau_r$  and  $\tau_d$ , are set as  $10^{-6}$  and  $10^{-3}$ , respectively.

### 5.3.1. TEST 1: EDGE INCLINED CRACK SLIP

In this test case, a fully cracked domain of size 2 [m]  $\times$  4 [m] is considered. The fine scale mesh is set as  $50 \times 100$  and the coarse mesh is set as  $5 \times 10$ . The material is homogeneous with Young's modulus  $E = 10^5$  [Pa] and Poisson's ratio  $\nu = 0.3$ . Coordinates of the fracture are shown in Fig. 5.1. The frictional coefficient reads  $\mu_f = 0.1$ . The penalty parameters

are set as  $C_N = C_T = 10^7$  [N/m<sup>3</sup>]. The top boundary is under the downward Dirichlet boundary condition of  $-0.1$  [m] while the bottom boundary is fixed in both the  $x$  and  $y$  directions. The left and right boundaries are stress free boundaries.

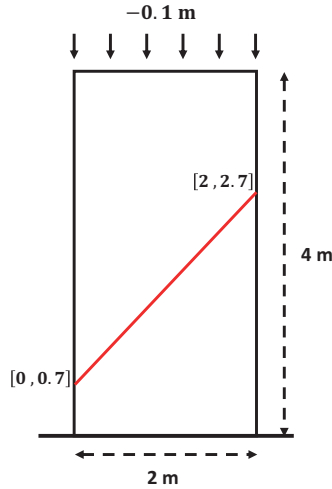


Figure 5.1: Test case 1: illustration of the model setup.

For this test case, the slip value  $d_s$  is a constant value of  $0.1\sqrt{2}$ , or 0.1414 [98]. The simulated slip profile of using MS-XFEM without GMRES is very close to this value, which is shown in Fig. 5.2. This demonstrates the correctness of constructing basis functions without a penalty matrix. This result demonstrates the potential of MS-XFEM to generate the high quality results.

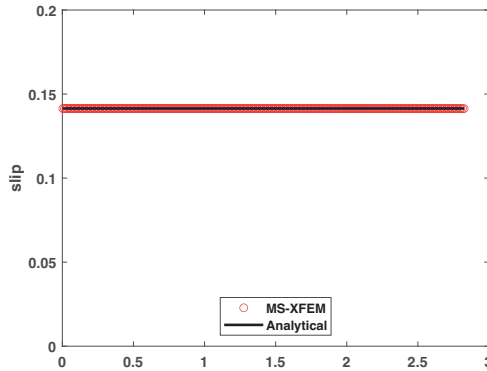


Figure 5.2: Test case 1: slip profile computed by analytical method (black curve) and MS-XFEM method without using GMRES (red curve with circle markers).

The displacements fields simulated using MS-XFEM (without GMRES) is close to the one simulated using fine scale XFEM, as shown in Fig. 5.3.

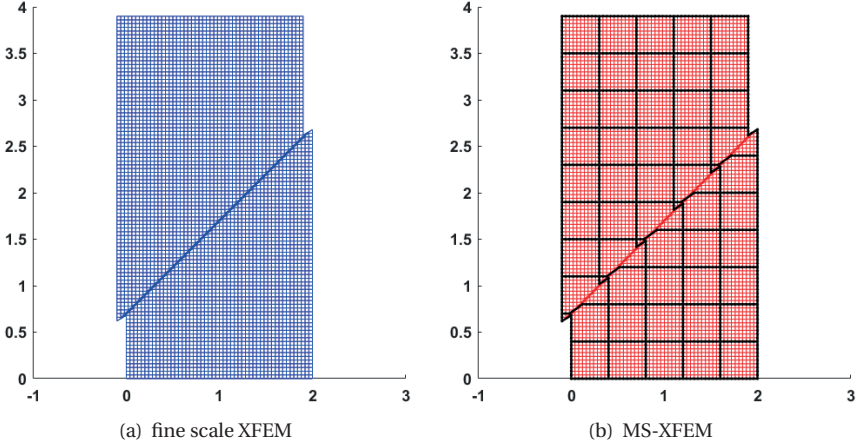


Figure 5.3: Test case 1: displacement field computed using (a) fine scale XFEM and (b) MS-XFEM (without GMRES). The black lines in (b) represent the coarse scale mesh. These two results are nearly identical.

### 5.3.2. TEST 2: SINGLE INCLINED CRACK SLIP

In this test case, a square domain of size  $10 [m] \times 10 [m]$  that contains a single inclined crack is studied. The material is homogeneous with Young's modulus  $E = 25 [GPa]$  and Poisson's ratio  $\nu = 0.25$ . The center point of the fracture is located at point  $[5, 5]$  and the total length of the fracture is  $2 [m]$ . The fracture exhibits a  $20$  degrees inclination with respect to the  $y$  direction. The frictional angle is  $\varphi = 30$  degrees thus the frictional coefficient  $\mu_f = 0.577$ . The penalty parameters are set as  $C_T = C_N = 25 \times 10^{11} [N/m^3]$ . The top boundary is subjected to a distributed load of  $10 [MPa]$  in the downward direction, while the bottom boundary is under a distributed load of  $10 [MPa]$  in the upward direction. All other boundaries are considered stress-free.

The analytical profile for an unbounded domain is given by

$$d_{slip} = \frac{4f_{CT}^a(1-\nu^2)}{E} \sqrt{l^2 - (\eta - l)^2}, \quad (5.4)$$

in which  $l$  is the half length of fracture that is  $1 [m]$  here [99, 100]. This analytical solution is provided only as a guideline of what the slip profile for an unbounded domain should look like. Note that we do not expect to converge to this solution, as it is a solution to a different problem than our numerical bound test case. Moreover,  $\eta$  is the coordinate along the fracture, so  $0 \leq \eta \leq 2 [m]$ , and  $f_{CT}^a$  is the analytical tangential force according

$$f_{CT}^a = \sigma \sin(\alpha) \cos(\alpha) - \sigma \sin^2(\alpha) \tan(\varphi). \quad (5.5)$$

Here,  $\sigma$  is the external loading force which is  $10 [MPa]$ .  $\alpha$  is the angle between inclined fracture and  $y$  direction which is  $20^\circ$ , and  $\tan(\varphi) \approx 0.577$  is the frictional coefficient.

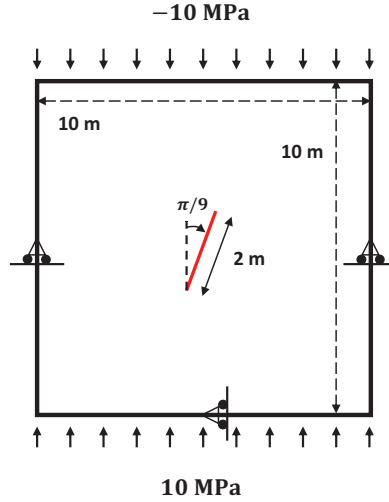


Figure 5.4: Test case 2: illustration of the model setup.

#### SENSITIVITY OF FINE SCALE RESULT

The slip profile computed with fine scale XFEM using the penalty method is sensitive to the mesh resolutions. In Fig. 5.5, slip profiles computed with a fine scale mesh of  $[50 \times 50]$ ,  $[80 \times 80]$  and  $[100 \times 100]$  are plotted. Also as a guideline, the slip profile for an unbounded domain as expressed in Eq.(5.4) is shown. Note that the XFEM slip profiles entail some oscillations which are known to be due to the misalignment of the crack and the Cartesian structured grid. Additionally, it is essential to highlight the presence of oscillations in the slip profile along the fracture and a dip of slip profile around the center of the fracture. The dipping of the slip profile toward the center of the fracture can be attributed to the well-known oscillations along the fracture resulted by XFEM. As an embedded method, XFEM exhibits oscillations along the interface within the element, often necessitating the utilization of higher-order shape functions. This dipping around the center point of the fracture requires further investigation, although it is not the main objective of this thesis, and, as such, detailed exploration has not been extensively pursued. In literature [100, 101], the penalty method is shown to result in slip profiles which have smaller values than the analytical guideline. This is consistent to what is observed in Fig. 5.5 while the unavoidable oscillations introduced by XFEM contribute to a more pronounced discrepancy between the XFEM-generated slip profile and the analytical counterpart.

#### COMPARISON BETWEEN FINE SCALE XFEM AND MS-XFEM

If the slip profile simulated with MS-XFEM closely matches or is identical to the one obtained through direct fine scale XFEM simulation, it is reasonable to assume that with a finer mesh resolution applied to MS-XFEM, the corresponding MS-XFEM result will

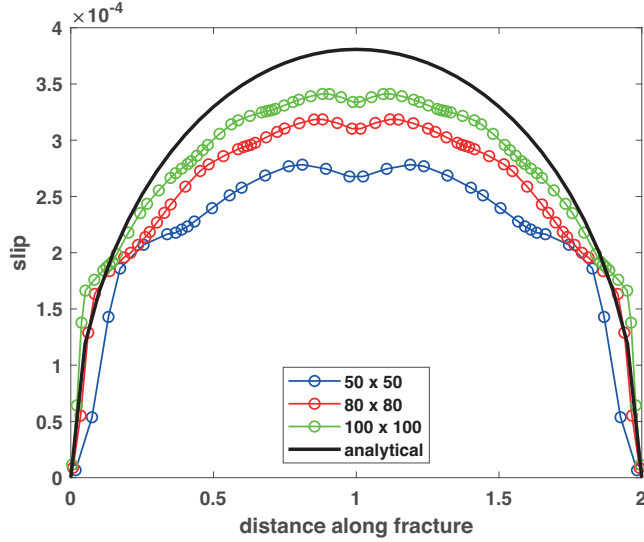


Figure 5.5: Test Case 2: XFEM solutions with mesh resolutions of  $[50 \times 50]$ ,  $[80 \times 80]$ , and  $[100 \times 100]$ . As a guideline, the analytical solution described by Eq. (5.4) to the unbounded domain is also provided.

approximate the analytical solution. Thus, in this test case, the slip profile simulated using MS-XFEM is compared to the fine scale XFEM slip profile. The fine scale mesh resolution is  $[80 \times 80]$  and its slip profile is already plotted in Fig. 5.5. The coarse mesh resolution is set as  $[5 \times 5]$  and the coarse mesh setup is plotted in Fig. 5.6.

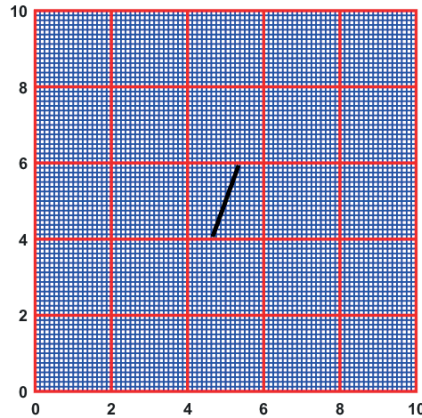


Figure 5.6: Test Case 2: coarse scale mesh (red) and fine scale mesh (blue). The fracture (black) is in one of the coarse scale element.

The slip profiles are plotted and compared in Fig. 5.7 (a) and (b). From Fig. 5.7 (a), it

is clear that there is a significant error involved in the slip profile simulated with MS-XFEM without GMRES. This error is significantly reduced when preconditioned GMRES is applied as shown in Fig. 5.7 (b). Note that the tolerance of GMRES used here is  $10^{-2}$  instead of  $10^{-6}$ . This shows that MS-XFEM with preconditioned GMRES converges to the fine scale XFEM result.

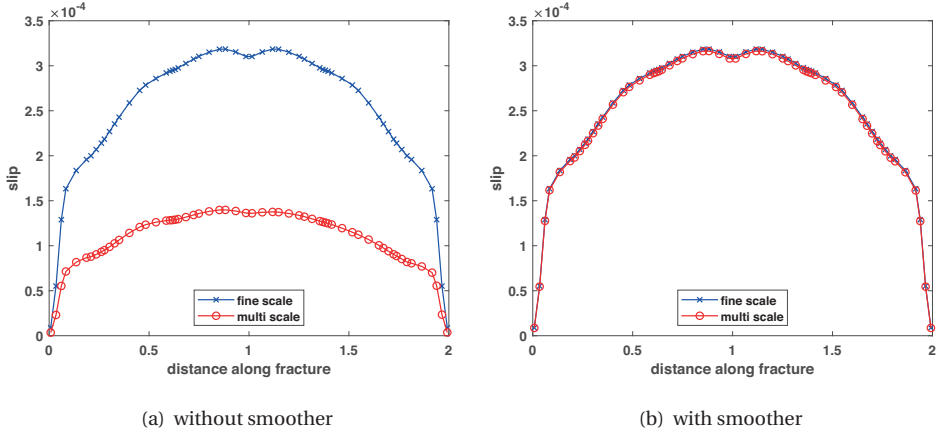


Figure 5.7: Test case 2: comparison between slip profiles by fine scale XFEM and (a) MS-XFEM (without iteration) and (b) MS-XFEM (with iterative multiscale strategy.). The blue curve represents the slip profile by fine scale XFEM and red curve represents the slip profile by MS-XFEM.

**5.3.3. TEST 3: MULTIPLE CROSSED CRACKS SLIP**

In this test case, a domain of size 10 [m] × 10 [m] that contains six cracks crossing each other is studied. The setup is shown in Fig. 5.8. The fine scale mesh is set as 50 × 50. The material of this domain is homogeneous with Young’s modulus  $E = 10^6$  [Pa] and Poisson’s ratio  $\nu = 0.3$ . The frictional coefficient  $\mu_f = 0.1$ . The penalty parameters are set as  $C_T = C_N = 10^8$  [N/m<sup>3</sup>]. The coordinates of all six fractures tips are shown in Table. 5.1. The top boundary is subjected to a downward Dirichlet boundary condition of  $-1$  [m].

	Left Tip	Right Tip
Fracture 1	[ 2.6 , 4.2 ]	[ 4.1 , 6.8 ]
Fracture 2	[ 2.2 , 5.6 ]	[ 4.0 , 4.6 ]
Fracture 3	[ 6.5 , 7.9 ]	[ 7.1 , 7.1 ]
Fracture 4	[ 6.4 , 5.2 ]	[ 7.4 , 8.0 ]
Fracture 5	[ 6.1 , 3.3 ]	[ 8.1 , 2.9 ]
Fracture 6	[ 5.4 , 2.1 ]	[ 8.0 , 3.6 ]

Table 5.1: Test case 3: fractures tips coordinates.

The bottom left corner is fixed in  $x$  and  $y$  direction, while the remaining nodes are con-

strained only in  $y$  direction. The left and right boundaries are considered as stress-free boundaries.

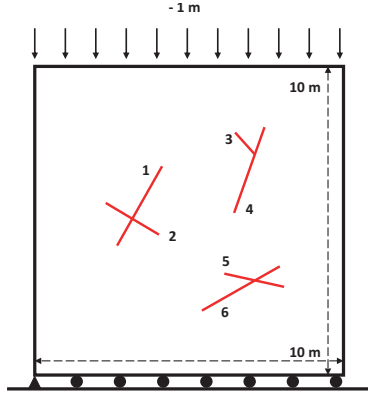


Figure 5.8: Test case 3: illustration of the model setup.

In this test case, two coarsening ratios of  $[5 \times 5]$  and  $[10 \times 10]$  are applied. Thus the coarse mesh resolutions applied are  $[10 \times 10]$  and  $[5 \times 5]$ . For this test case, the preconditioned GMRES tolerance is set as  $10^{-2}$  since there is no question that  $10^{-6}$  will lead to a perfect match of the MS-XFEM results with the fine scale XFEM result. It is important to analyze how MS-XFEM performs for different coarsening ratios. The fine scale XFEM displacement solutions on  $x$  and  $y$  directions are plotted in Fig. 5.9. They will be used as reference solutions. As the XFEM is known to introduce oscillations in the computed slip profile on the structured Cartesian mesh for not-aligned cracks, these plots show a staircase pattern for the displacement profile. This pattern is consistently observed in the subsequent surface plots including displacements plots, error plots and basis functions plots throughout this thesis.

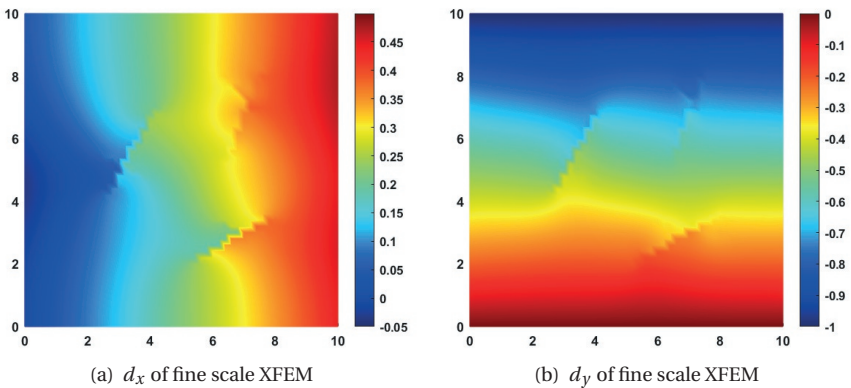


Figure 5.9: Test case 3: displacement fields of (a)  $x$  direction and (b)  $y$  direction computed using fine scale XFEM.

SIMULATION RESULTS WITH COARSE SCALE MESH [10 × 10]

The displacement fields of MS-XFEM using a coarse mesh of [10 × 10] is shown in Fig. 5.10 and they match well with the fine scale XFEM solutions as shown in the error plots in Fig. 5.11. Preconditioned GMRES successfully reduce the errors of final solutions as shown in Fig. 5.11. Note that the simulator converges to the criterion of displacement incremental of Eq. ??.

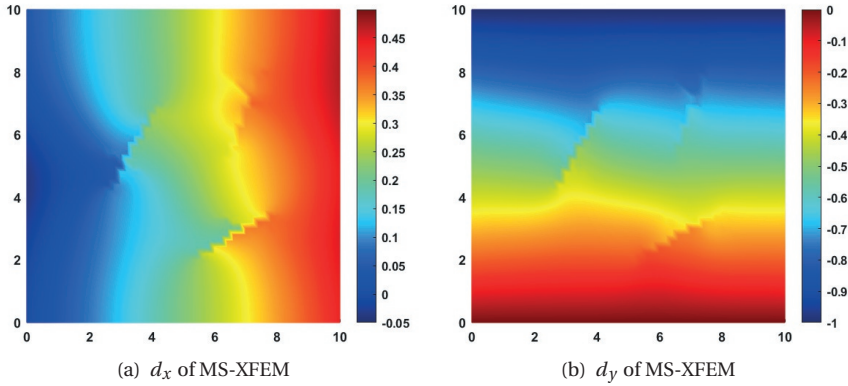


Figure 5.10: Test case 3: displacement field in (a) x direction and (b) y direction computed using MS-XFEM (with GMRES). Coarse scale mesh of 10 × 10.

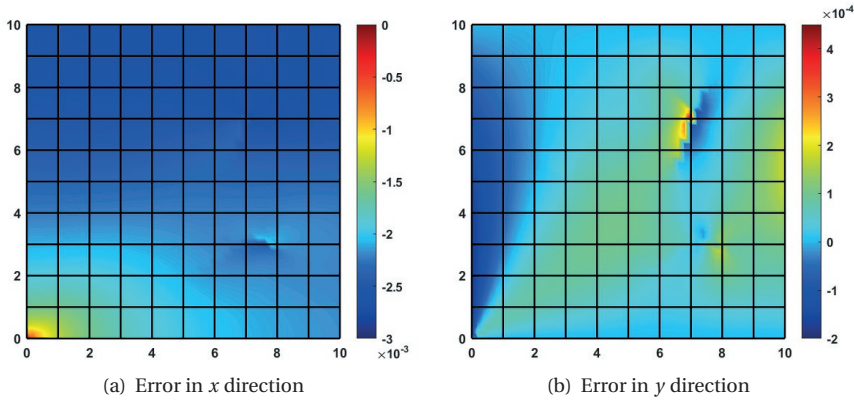


Figure 5.11: Test case 3: Errors in the displacement field along the (a) x direction and (b) y direction are displayed, comparing fine-scale XFEM with MS-XFEM (utilizing GMRES) on a coarse mesh grid of 10 × 10. The black lines represent the coarse mesh grid lines.

The basis function  $P_{yy}$  belonging to coarse mesh node [3, 6] is shown in Fig. 5.12. It is clear that the cross between fracture 1 and 2 is captured well by the basis functions. The preconditioned GMRES convergence history of outer loop [1, 2, 4, 6, 9] is recorded

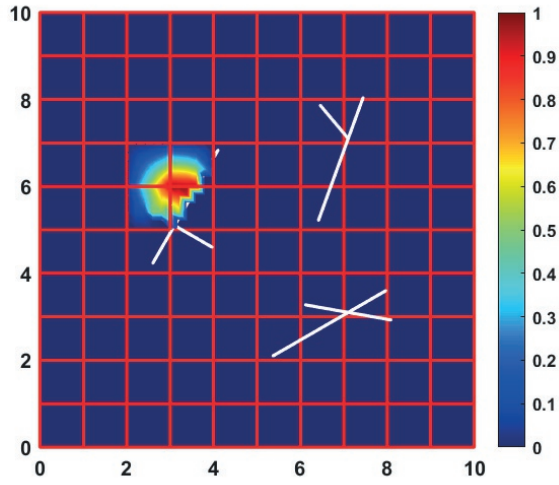


Figure 5.12: Test case 3: basis function  $P_{yy}$  belonging to the coarse node [3,6]. Coarse scale mesh is  $10 \times 10$ . Red lines represent the coarse scale mesh and white segments represent fractures.

and plotted in Fig. 5.13. The summation of all preconditioned GMRES iterations used in all 9 outer loops is 127.

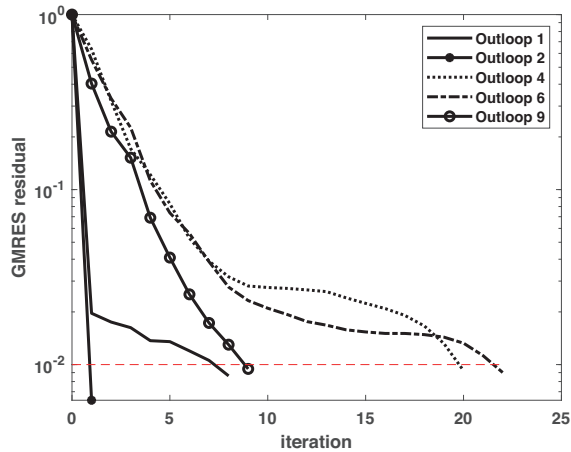


Figure 5.13: Test case 3: convergence history of preconditioned GMRES of outer loop [1,2,4,6,9]. After 9 outer loops the final solution converges. Total amount of iterations using preconditioned GMRES is 127.

SIMULATION RESULTS WITH COARSE SCALE MESH  $[5 \times 5]$

The displacement fields of MS-XFEM using a coarse mesh of  $[5 \times 5]$  are shown in Fig. 5.14. Again, preconditioned GMRES successfully reduces the errors of the final solutions, as it can be seen from the errors plots in Fig. 5.15.

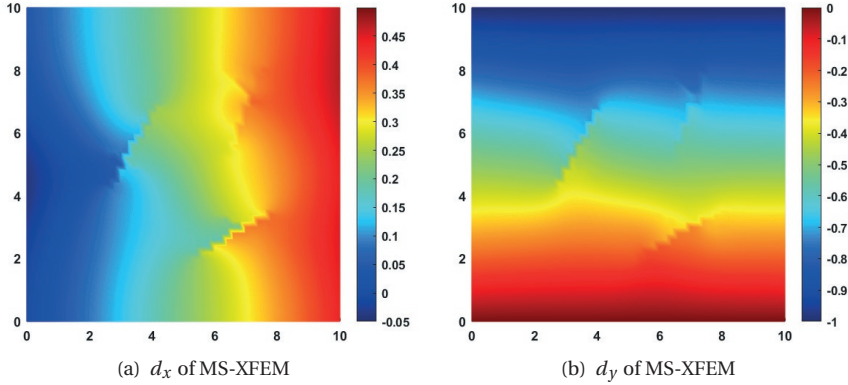


Figure 5.14: Test case 3: displacement field of (a) x direction and (b) y direction computed using MS-XFEM (with GMRES). Coarse scale mesh of  $5 \times 5$ .

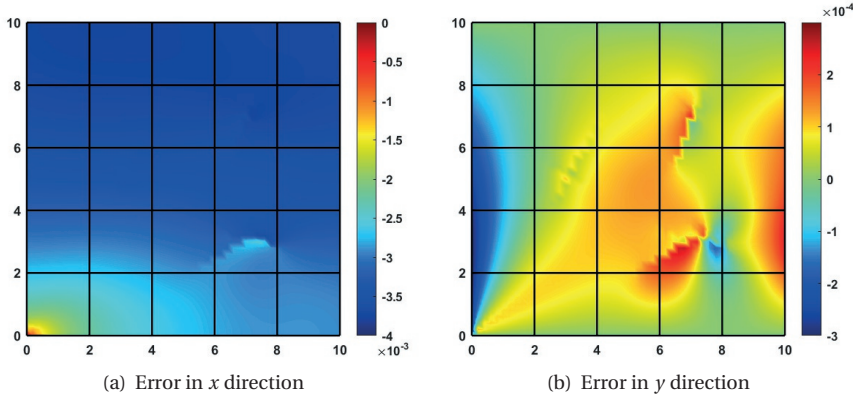


Figure 5.15: Test case 3: errors in the displacement field along the (a) x direction and (b) y direction are displayed, comparing fine-scale XFEM with MS-XFEM (utilizing GMRES) on a coarse mesh grid of  $5 \times 5$ . The black lines represent the coarse mesh grid lines.

The basis functions belonging to the coarse scale mesh node  $[4, 6]$  are shown in Fig. 5.16. As expected, the cross of fracture 1 and 2 is well captured. The preconditioned GMRES convergence history of outer loop  $[2, 4, 6, 8, 10]$  is recorded and plotted in Fig. 5.17. The summation of all preconditioned GMRES iterations of all ten outer loops is 162.

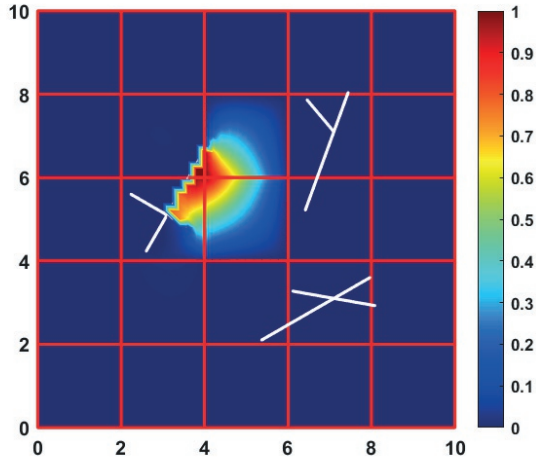


Figure 5.16: Test case 3: basis function  $P_{yy}$  belonging to the coarse scale mesh node [4,6]. Coarse scale mesh is  $5 \times 5$ . Red lines represent the coarse scale mesh and white segments represent fractures.

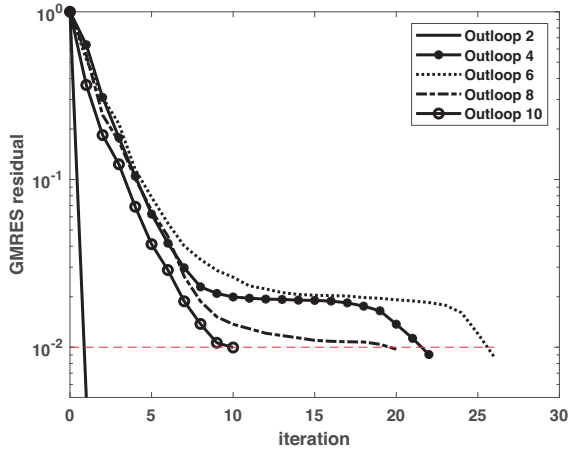


Figure 5.17: Test case 3: convergence history of outer loop [2, 4, 6, 8, 10]. Total amount of iterations using preconditioned GMRES is 162. Coarse scale mesh is  $5 \times 5$ .

#### 5.3.4. TEST 4: FRACTURE NETWORK OF HETEROGENEOUS FORMATION UNDER COMPRESSION

In this test case, a synthetic fracture network under compression is considered. The research domain is a  $80 \text{ [m]} \times 80 \text{ [m]}$  square. Fig. 5.18 provides a visual representation of the synthetic fracture network within this domain. Heterogeneous Young's modulus values, following a Gaussian distribution, are spatially mapped across the entire domain,

as depicted in Fig. 5.19. The Poisson's ratio in the domain is a constant value of  $\nu = 0.2$ . The frictional coefficient reads  $\mu_f = 0.3$ . To prevent penetration, penalty parameters, denoted as  $C_T$  and  $C_N$ , are adjusted for each element due to the varying Young's modulus values in the domain. Specifically, these penalty parameters are set to be 100 times larger than the local Young's modulus of each element.

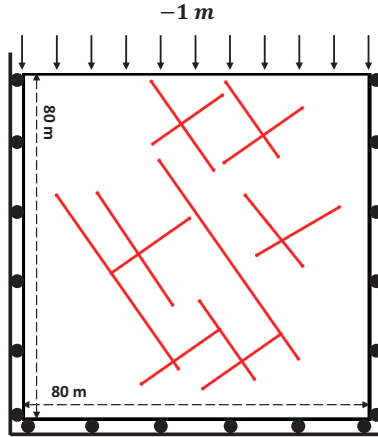


Figure 5.18: Test case 4: illustration of the test case 4 model.

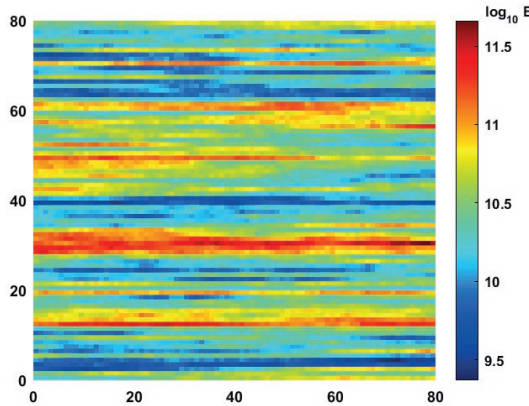


Figure 5.19: Test case 4: illustration of the Gaussian distributed heterogeneous Young's modulus map.

The fine scale mesh is set as  $80 \times 80$  and the coarse mesh is set as  $8 \times 8$ . The bottom boundary is fixed in  $y$  direction while the left and the right boundaries are fixed in  $x$  direction. The top boundary is under displacement controlled compression by 1 [m] downward. For this complicated test case, preconditioned GMRES is paired with MS-XFEM. The tolerance of MS-XFEM is set as  $10^{-2}$ .

The displacements solutions simulated by MS-XFEM are very close to the ones from fine

scale XFEM with in total 640 elements, as shown in Fig.5.20. The error plots shown in Fig. 5.21 also prove this. This means MS-XFEM has the capability to simulate a complicated fracture network accurately.

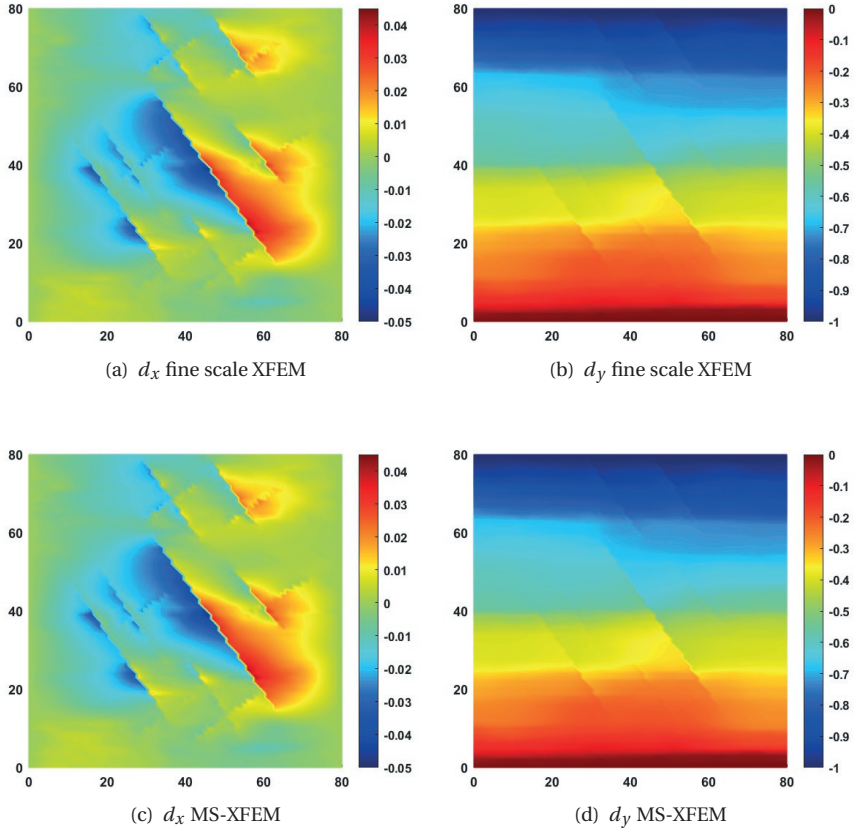


Figure 5.20: Test case 4: comparison between displacements solutions from fine scale XFEM and MS-XFEM. (a) and (b) show displacement fields in  $x$  direction and  $y$  direction, respectively, using fine scale XFEM. (c) and (d) show displacement fields in  $x$  direction and  $y$  direction, respectively, using MS-XFEM.

In this test case, basis functions have to capture heterogeneities and multiple fractures at the same time. The basis functions  $P_{yy}$  belong to the coarse grid points  $[10, 10]$  and  $[30, 30]$  are plotted in Fig. 5.22. It is clear that from Fig. 5.22 (a) basis functions capture the heterogeneities inside the Young's modulus map as it is not a standard bi-linear basis functions. Fig. 5.22 (b) presents how basis functions capture multiple discontinuities.

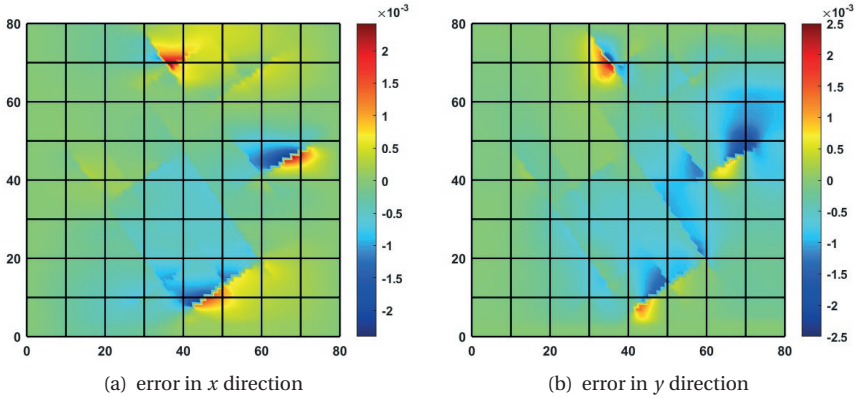


Figure 5.21: Test case 4: errors between solutions from fine scale XFEM and MS-XFEM in (a)  $x$  direction and in (b)  $y$  direction, respectively.

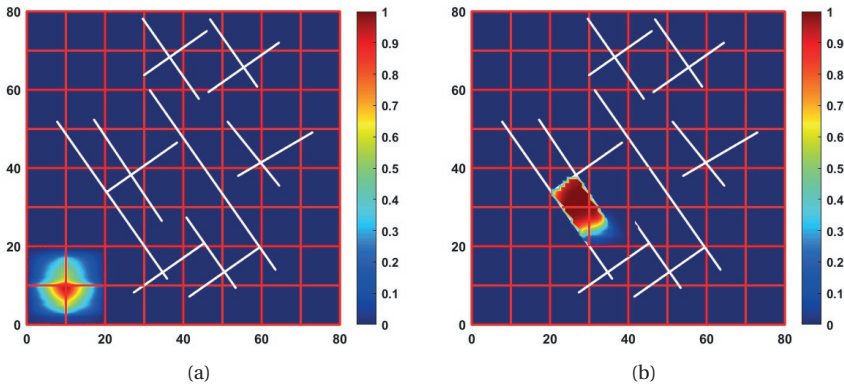


Figure 5.22: Test case 4: basis functions  $P_{yy}$  belong to the coarse scale mesh node (a)  $[10, 10]$  and (b)  $[30, 30]$ . Note that (a) is not a standard bi-linear basis function due to heterogeneities. (b) captures multiple crossing fractures. Red lines represent the coarse mesh and white segments represent fractures.

## 5.4. CONCLUSIONS

This chapter focused on developing MS-XFEM for simulating self-contact and frictional slip within fractures. The penalty method is employed to prevent penetration between of opposing fracture surfaces, and slip-stick conditions are determined using Coulomb's law. In terms of MS-XFEM application, basis functions are constructed using the original stiffness matrix, without the inclusion of a penalty matrix. Four test cases demonstrate the accuracy and suitability of applying MS-XFEM for simulating compressed fractured formations. The first test case validates the correctness of the basis functions construc-

tion method proposed in this chapter. In the second test case, it is essential for future validation to compare the fine-scale slip profile with the analytical slip profile. The numerical slip profile displays noticeable oscillations and a significant error compared to the analytical slip profile; however, these aspects fall outside the primary focus of this thesis. Nevertheless, the favorable comparison between the slip profiles of fine-scale XFEM and MS-XFEM underscores the accuracy of MS-XFEM. In the third test case, the influence of different coarsening ratios on MS-XFEM's performance is investigated. The preconditioned GMRES iterative strategy effectively reduces errors to the desired level, as anticipated. Notably, when using larger size coarse mesh elements, an additional 25 iterations of preconditioned GMRES are needed. This is a reasonable outcome, as larger coarse mesh sizes may introduce more errors before the smoothing process. All test cases underscore the considerable potential of applying MS-XFEM in the complex simulation of fractured formations found in real-world scenarios.

# 6

## MS-XFEM FOR SIMULATING MIXED-MODE FRACTURE PROPAGATION

This chapter extends the applicability of MS-XFEM to simulate fracture growth under compression in mixed mode. It is noteworthy that contact and slip behavior between fracture surfaces can result in the propagation of fractures in mode I, despite the prevailing global compression loading conditions. In real-world subsurface fractured formations, operations such as fluid injection can similarly induce the opening of fractures within highly compressed formations. This unique scenario, characterized by the coexistence of both mode I and mode II fractures, is referred to as 'mixed mode.' To effectively employ MS-XFEM in real-field simulations, it is imperative to ascertain its suitability for accurately modeling mixed-mode fracture propagation.

### 6.1. MIXED MODE FRACTURES PROPAGATION

Fracture propagation under compressive global loading typically involves a mixed-mode failure phenomenon, as depicted in Fig. 6.1. The application of compressive outer boundary loading results in the contact of fracture surfaces, accompanied by non-zero contact forces. Upon activation of these fractures, the dominant behavior along the fracture surfaces manifests as slip, indicative of mode-II shearing behavior. This slip may activate the tip of fractures, initiating their propagation. Notably, the propagated segment of the fracture tends to promptly open due to the slip along the original part of the fracture, characterizing this propagation as, in essence, a local mode-I propagation mechanism.

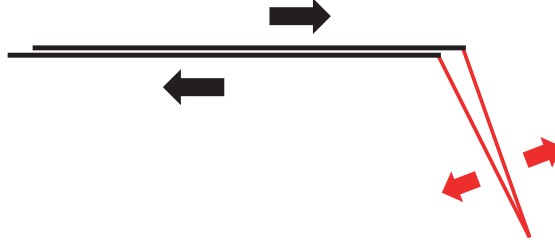


Figure 6.1: Illustration showing the kinked propagation of a fracture due to shearing along the original fracture. The shearing along the initial fracture section (in black color) induces forces causing the kinked propagated part (in red color) to open.

### 6.1.1. CHALLENGES OF KINKED CRACK GROWING PATHS

Simulating mixed-mode fracture propagation through the maximum principle stress criterion using stress intensity factors in Eq. (2.29) can be challenging. In Equation (2.29), the propagation angle computation requires the computation of  $K_I$  and  $K_{II}$  values at the end of each propagation step. However, in embedded methods like XFEM, computational oscillations may manifest during the stress intensity factor calculations. For instance, when simulating the propagation of a wing crack subjected to uniaxial compression loading. Fig. 6.2 (a) demonstrates the oscillatory behavior exhibited by  $K_{II}$  throughout the propagation steps, a phenomenon also documented in [102].

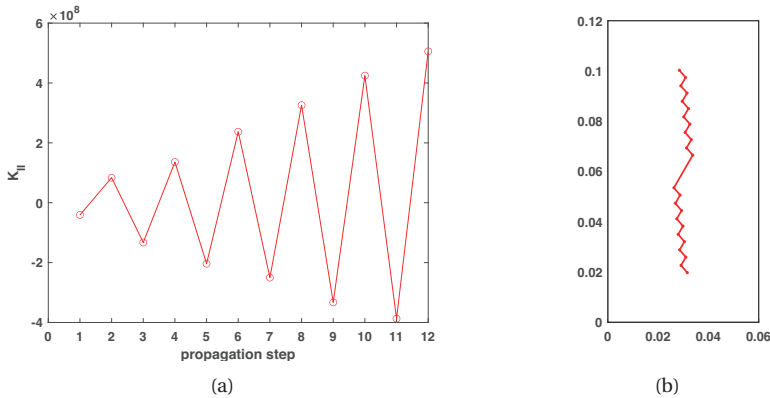


Figure 6.2: (a) Oscillation of stress intensity factor  $K_{II}$  in the simulation of wing crack propagation and (b) oscillation of  $K_{II}$  in the simulation of wing crack propagation.

The oscillations observed in  $K_{II}$  have a significant impact on the resulting crack path, often manifesting as a 'zig-zag' pattern, as illustrated in Fig. 6.2(b). This effect arises from the variation in the computed propagation angle, which relies on the oscillatory values of  $K_{II}$  obtained through Equation (2.29). Thus, in this chapter, the maximum principle stress theory based on the weighted spatial average stress vector, as introduced in

Chapter 2, is applied to determine the propagation angle.

### 6.1.2. PRINCIPLES OF MIXED MODE FRACTURES PROPAGATION

For a multiple fractured medium under compressive loading, a fracture tip is considered to propagate if its surrounding stress values surpass the tensile strength of the material. This is expressed as

$$\sigma_1 > \sigma_t, \quad (6.1)$$

in which  $\sigma_1$  represents the maximum principal tensile stress, and  $\sigma_t$  represents the tensile strength of the material. The propagation speed, or the distance which fractures tips propagate in one time step, is taken as a constant value, which is the same as in Chapter 4. The propagation angle is computed by the weighted spatial average method introduced in section 2.3.

## 6.2. ALGORITHM FOR APPLYING MS-XFEM

The algorithm detailing the application of MS-XFEM for simulating mixed-mode fractures propagation under compression loading is presented in algorithm. 4. This algorithm represents a fusion of the methodologies developed in Chapter 4 and Chapter 5. Still, in the application of MS-XFEM, basis functions are updated locally where fracture geometries change. The convergence conditions within each time step are the same as the two standard convergence conditions introduced in Chapter 5.

---

**Algorithm 4** Algorithm for applying MS-XFEM to the simulation of fractures propagation

---

```

Construct fine scale  $K^h$ 
for  $i = 1 \rightarrow$  final step do
  For iteration  $v$ 
  while  $\frac{\|r^{v+1}\|}{\|r_{i,0}\|} \geq \tau_r$  or  $\frac{\|\Delta d^{v+1}\|}{\|d^v\|} \geq \tau_d$  do
    Update  $K^{p^v} = K^h + K_{con}^v$ 
    Solve using MS-XFEM with preconditioned GMRES until convergence
    Update  $d^{v+1} = d^v + \Delta d^{v+1}$ 
    Update  $r^{v+1} = f^h - f_c - K^h \cdot d^{v+1}$ 
    Update stick and slip conditions along each Gauss point
  end while
  Update fractures and  $K^h$ 
end for

```

---

### 6.3. TEST CASES

In this section, two test cases demonstrating the application of MS-XFEM for simulating fractures under compressive loading are presented. Two convergence tolerance values,  $\tau_r$  and  $\tau_d$ , are set as  $10^{-6}$  and  $10^{-3}$ , respectively.

### 6.3.1. WING CRACK PROPAGATION IN UNI-AXIAL COMPRESSION

In this test case, a rectangular granite sample of size 60 [mm]  $\times$  120 [mm] under uni-axial compression is simulated using MS-XFEM. This test is based on the experimental test performed in the literature [103]. The setup is shown in Fig 6.3. The fracture is in total 6 [mm] long and is rotated by  $\alpha$  degrees with respect to the  $x$ -axis and located at the center of the sample. The material is granite with Young's modulus  $E = 62$  [GPa] and Poisson's ratio is  $\nu = 0.22$ . The tensile strength is 16 [MPa] and the penalty parameters are set as  $C_T = C_N = 62 \times 10^2$  [GPa].

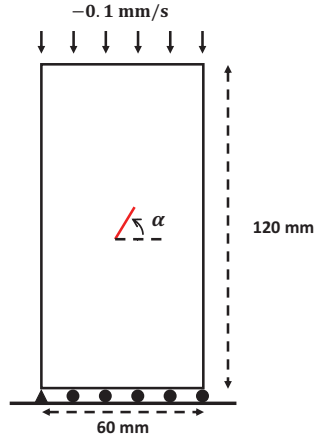


Figure 6.3: Test case 1: illustration of the model setup.

The lower-left corner is fixed in both the  $x$  and  $y$  directions, whereas the remaining nodes along the bottom boundary are restricted solely in  $y$ -direction. On the contrary, at the upper boundary, a controlled downward displacement condition is enforced. This condition dictates a downward displacement at a rate of 0.1 [mm/s]. Lastly, the left and right boundaries are stress-free, which will result in mixed-mode propagation, as the opening along the fracture is not constrained by the left and right boundaries. The entire simulation duration spans 10 [s] and is discretized into 10 equal steps, each lasting 1 [s]. The fine-scale mesh is defined as  $30 \times 60$ , while the coarse-scale mesh is set to  $3 \times 6$ , employing a coarsening ratio of  $[10 \times 10]$ . Within this context, preconditioned GMRES iterations are employed with a tolerance threshold of  $10^{-2}$ .

To evaluate the accuracy of the final result, a direct comparison is conducted between the major wing crack propagation paths simulated using fine-scale XFEM and those obtained in the experimental study from the literature [103]. This comparative analysis involves selecting three different rotation angles, namely  $\alpha = \pi/6, \pi/4, \pi/3$ , consistent with the conditions outlined in [103]. The results are depicted in Fig. 6.4. The red-colored crack paths represent simulations conducted with fine-scale XFEM and are superimposed onto images extracted from the experimental study in [103]. The black-colored paths labeled with 'T' correspond to tensile wing cracks. It is evident that for all three

tests with varying inclination angles, the simulated major wing crack paths closely resemble the experimental observations. Importantly, the crack paths generated using fine-scale XFEM exhibit significantly smoother profiles than those shown in Fig. 6.2 (b).

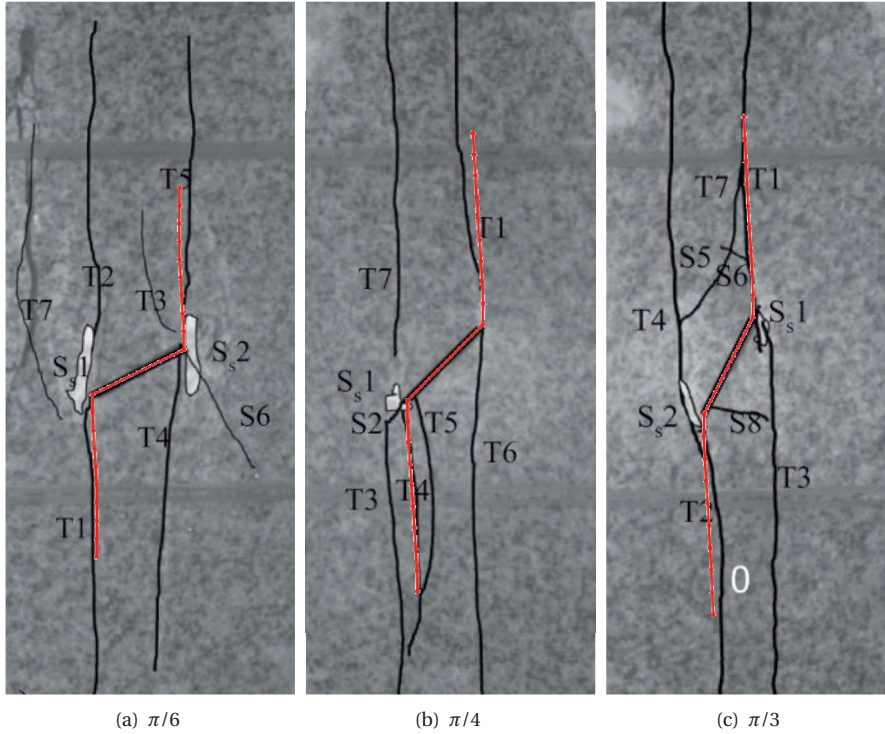


Figure 6.4: Test case 1: crack paths simulated using fine-scale XFEM are compared to experimental crack paths for various inclination angles: (a)  $\pi/6$ , (b)  $\pi/4$ , and (c)  $\pi/3$ . The red lines represent crack paths simulated with fine-scale XFEM, while the black-colored crack paths labeled with "T" on the experimental images denote the major wing cracks. The grey background images are sourced from [103].

If the crack paths simulated using MS-XFEM closely resemble those generated by fine-scale XFEM, it signifies that MS-XFEM can produce sufficiently accurate results. The crack paths simulated with MS-XFEM (utilizing GMRES) for all three inclined angles are compared to the crack paths shown in Fig. 6.4 and are presented in Fig. 6.5. The figure clearly demonstrates a high degree of alignment between the crack paths simulated with MS-XFEM (with GMRES) and those obtained through fine-scale XFEM.

In Fig. 6.6, the  $x$  directional displacement from fine scale XFEM and MS-XFEM with inclination angle of  $\pi/6$  are plotted. The error plot between these two displacements fields is also plotted in Fig. 6.6 (c). Preconditioned GMRES iterations reduce the errors of MS-XFEM results significantly as expected.

The basis functions for the coarse mesh node at coordinates  $[0.02, 0.04]$ , at both step 1 and step 6, are depicted in Fig. 6.7. It is evident that the update of basis functions has been successful in capturing the propagating fracture tip.

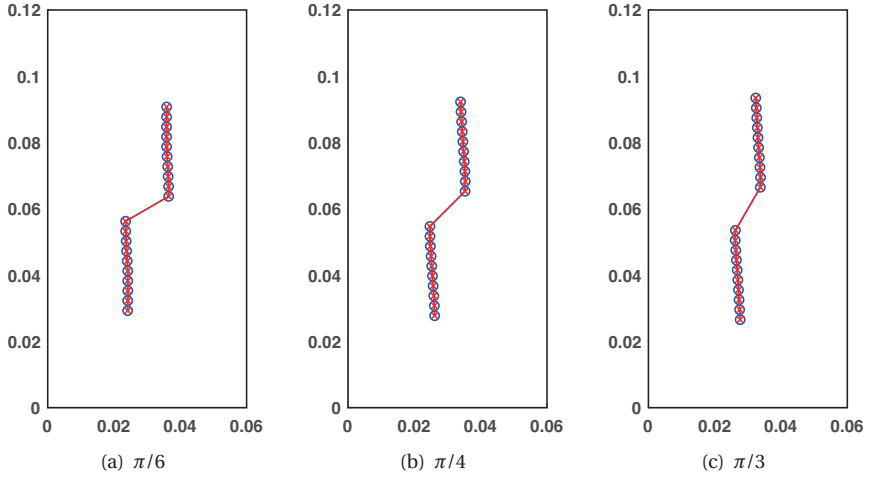


Figure 6.5: Test case 1: Crack paths simulated with MS-XFEM compared to the crack patterns generated by fine-scale XFEM. The inclination angles are (a)  $\pi/6$ , (b)  $\pi/4$ , and (c)  $\pi/3$ . The blue circles represent the crack paths simulated with fine-scale XFEM, while the red lines represent the crack patterns from MS-XFEM.

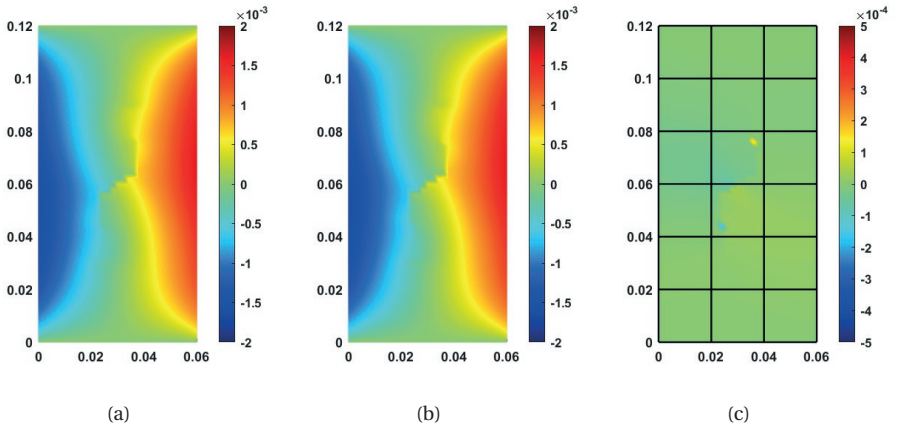


Figure 6.6: Test case 1:  $x$  direction displacement of (a) fine scale XFEM and (b) MS-XFEM. The error plot between these two results is shown in (c).

### 6.3.2. MULTIPLE FRACTURES PROPAGATION UNDER COMPRESSION

In this test, a sandstone sample of size  $10 \text{ [m]} \times 10 \text{ [m]}$  with 9 fractures under compression loading is simulated, as shown in Fig. 6.8. All 9 fractures have the same length of 1 [m]. The coordinates of the fractures are given in Table. 6.1

The material is sandstone with Young's modulus  $E = 25 \text{ [GPa]}$  and Poisson's ratio  $\nu = 0.23$ . The tensile strength is 6 [MPa]. Penalty parameters are set as  $C_T = C_N = 2.5 \times$

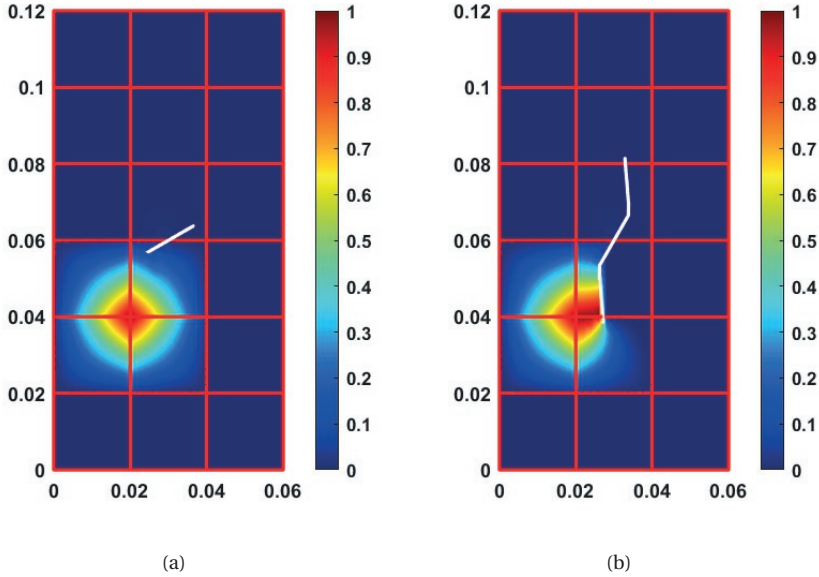


Figure 6.7: Test case 1: basis functions of coarse mesh point  $[0.02, 0.04]$  at step (a) 1 and (b) step 6. Red lines represent the coarse mesh and white segment represents the fracture.

	Left Tip	Right Tip
Fracture 1	[ 2.52 , 2.87 ]	[ 3.48 , 3.13 ]
Fracture 2	[ 4.68 , 3.38 ]	[ 5.32 , 2.62 ]
Fracture 3	[ 6.57 , 2.75 ]	[ 7.43 , 3.25 ]
Fracture 4	[ 2.91 , 5.49 ]	[ 3.09 , 4.51 ]
Fracture 5	[ 4.51 , 4.91 ]	[ 5.49 , 5.09 ]
Fracture 6	[ 6.52 , 5.13 ]	[ 7.48 , 4.87 ]
Fracture 7	[ 2.65 , 6.65 ]	[ 3.35 , 7.35 ]
Fracture 8	[ 4.87 , 7.48 ]	[ 5.13 , 6.52 ]
Fracture 9	[ 6.65 , 6.65 ]	[ 7.35 , 7.35 ]

Table 6.1: Test case 2: illustration of the fractures coordinates.

$10^{12}$  [Pa]. Frictional coefficient is  $\mu_f = 0.577$ . Regarding boundary conditions, the left-bottom corner is completely fixed, while the nodes along the bottom boundary are constrained in vertical direction. On the top boundary, a downward distributed loading  $q$  is applied. The initial value of  $q$  is 10 [MPa], and it increases by 1 [MPa] in each loading step.

The simulation spans a total time of 11 seconds, with each time step lasting 1 second. The fine-scale mesh employed consists of a grid with dimensions of  $50 \times 50$ , while the coarse mesh employs a  $5 \times 5$  grid, resulting in a coarsening ratio of  $10 \times 10$ . Preconditioned GMRES is utilized for the simulation, with a specified tolerance of  $10^{-2}$ . This

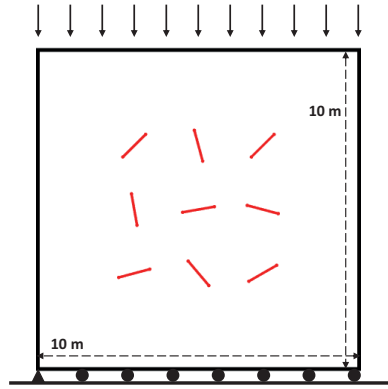


Figure 6.8: Test Case 2: illustration of the model setup.

setup aims to evaluate whether MS-XFEM can accurately simulate crack propagation with only a minimal number of smoothing iterations.

The crack propagation paths at steps 6 and 11 are illustrated in Figure 6.9. The crack paths simulated using MS-XFEM are superimposed upon those simulated with fine-scale XFEM. It is evident from Figure 6.9 that these paths exhibit a close match, validating the accuracy of the MS-XFEM simulations.

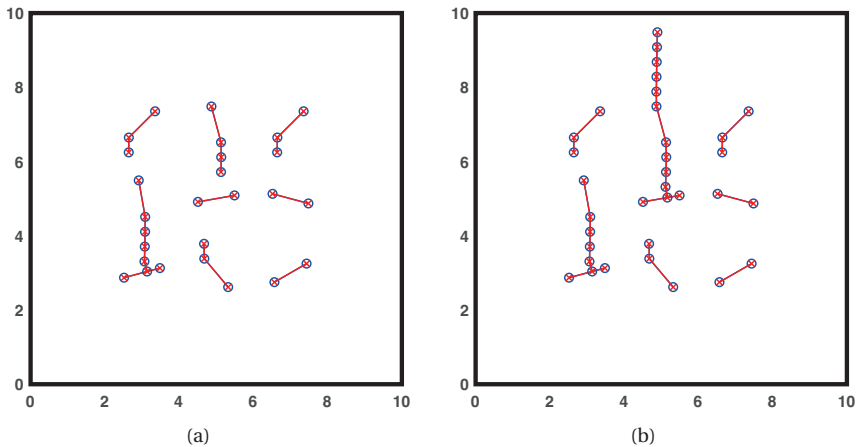


Figure 6.9: Test case 2: crack patterns simulated by fine scale XFEM (blue circle) and MS-XFEM (red cross) at time step (a) 6 and (b) 11.

The displacement fields in the  $x$  and  $y$  directions at final step (step=11) from both fine-scale XFEM and MS-XFEM (with GMRES) are visualized in Figure 6.10. Notably, the results obtained from MS-XFEM closely align with those from fine-scale XFEM. To further

illustrate this agreement, the displacement errors between the two methods are depicted in Figure 6.11. By employing preconditioned GMRES, these errors are effectively reduced to the desired level.

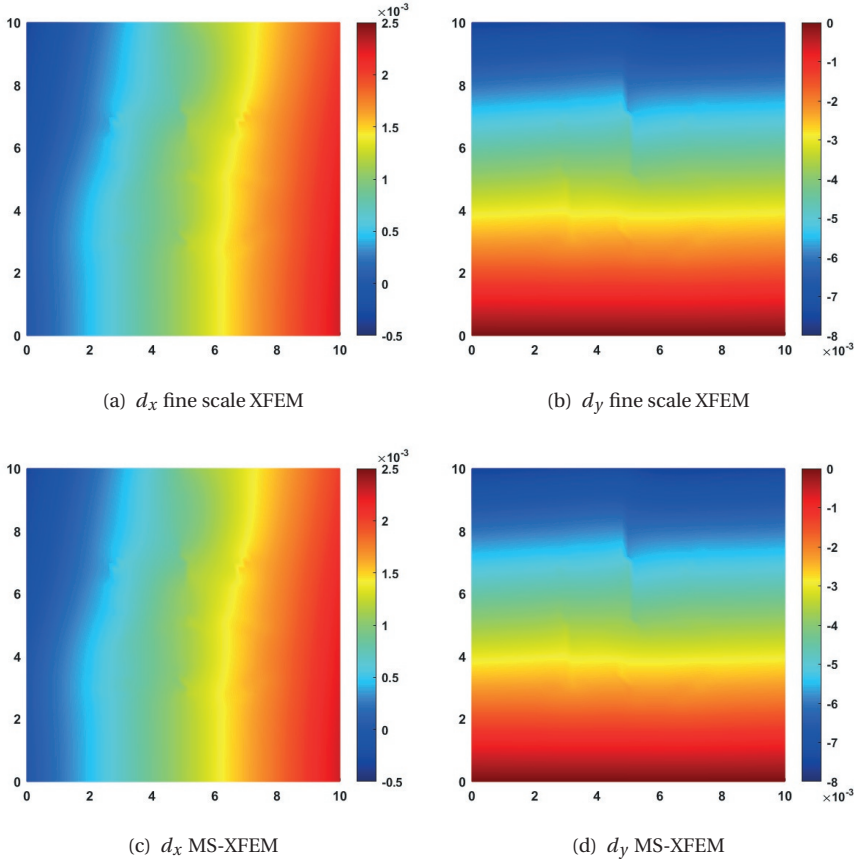


Figure 6.10: Test case 2: displacements fields simulated from fine scale XFEM (first row) and MS-XFEM with preconditioned GMRES iterations using tolerance of  $10^{-2}$  (second row).

The basis functions centered at the coarse mesh point  $[4,6]$  at time steps 8 and 11 are displayed in Fig. 6.12. Clearly, the basis functions update has effectively captured the fracture propagation. Note that the junction between fracture 8 and fracture 5 is perfectly captured by basis functions in 6.12 (b).

### 6.3.3. FRACTURES PROPAGATION DUE TO LATERAL TRACTION FORCES

This test investigates fault slip and propagation within a heterogeneous fractured formation in response to lateral forces, representing a scenario of induced fault sliding and propagation. The fractured formation shown in Fig. 6.13 has a size of  $150 \text{ [m]} \times 40 \text{ [m]}$

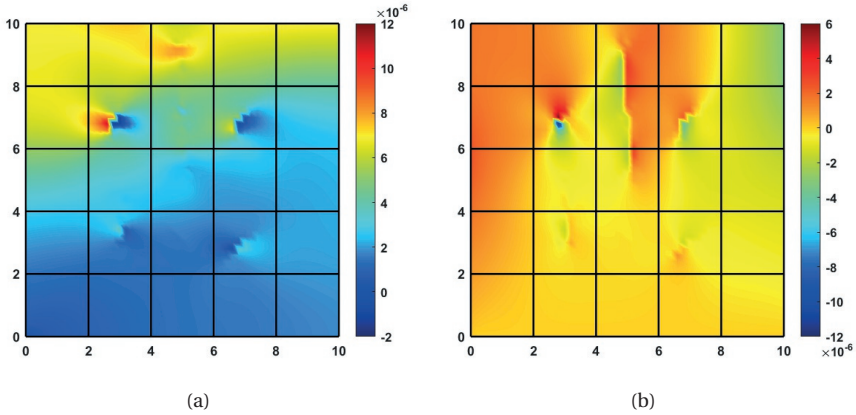


Figure 6.11: Test case 2: Displacement field errors between simulations from fine-scale XFEM and MS-XFEM in (a)  $x$  direction and (b)  $y$  direction. Black lines depict the coarse-scale mesh.

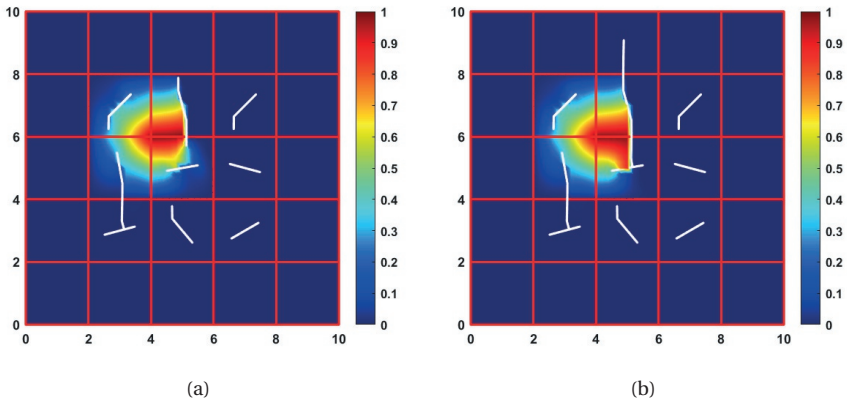


Figure 6.12: Test case 2: Basis functions centered at the coarse mesh point  $[4, 6]$  at time steps 8 and 11. Notably, the updated basis functions in (b) accurately capture the "T"-shaped intersection between fracture 8 and fracture 5. Red lines represent the coarse mesh and white segments represent fractures.

and contains seven fractures. The heterogeneous Young's modulus field is depicted in Figure 6.14. The Poisson's ratio remains constant at  $\nu = 0.2$  throughout the domain, and a frictional angle of 30 degrees corresponds to a frictional coefficient of  $\mu_f = 0.577$ . To account for heterogeneities within the formation, penalty parameters ( $C_T$  and  $C_N$ ) for each element are set as 100 times the local Young's modulus value, a method previously described in Chapter 5, Test Case 4. The tensile strength of this formation is set as 6 [MPa]. Boundary conditions are imposed as follows: displacements in  $x$ -direction are constrained along the left boundary, while displacements in  $y$ -direction are fixed along the bottom boundary. It is assumed that this formation lies at a depth of 500 [m] below the ground

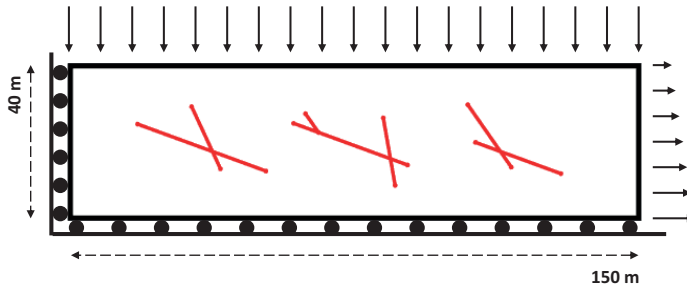


Figure 6.13: Test case 3: illustration of the model setup.

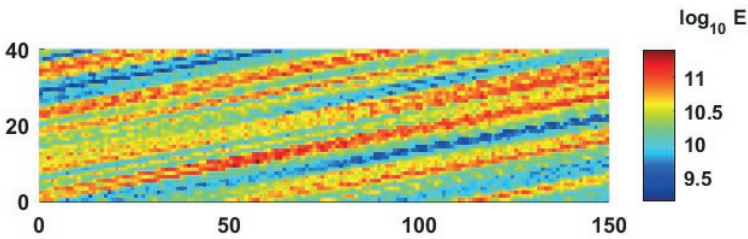


Figure 6.14: Test case 3: illustration of heterogeneous Young's modulus map for test case 3.

surface, with homogeneous sandstone as its overburden. Therefore, the compressive loading distributed along the top boundary has a magnitude of  $1.3 \times 10^7$  [N/m]. Along the right boundary, a linearly distributed tensile loading is introduced to model the traction force resulting from for example the shrinkage of a nearby reservoir. Specifically, at the upper right corner, the tensile loading is set at  $1.3 \times 10^4$  [N/m], while at the lower right corner, it is equal to  $1.4 \times 10^4$  [N/m].

The fine-scale mesh for the fine Scale XFEM is configured as  $150 \times 40$ , while the coarse mesh is established as  $15 \times 4$  for efficient problem simulation. The total simulation time spans five steps, and for each step, the fracture propagation length is set at 1.5 times the element size. In this approach, preconditioned GMRES is utilized, with the tolerance maintained at  $10^{-2}$ .

The final displacement solutions obtained from the fine scale XFEM and MS-XFEM are presented in Figure 6.15. The presence of fracture sliding is clearly evident in the figures, as expected when lateral tensile traction is applied to subsurface formations. Error plots are depicted in Figure 6.16. Notably, it is evident that the simulation results achieved with MS-XFEM closely approximate the fine-scale XFEM solutions.

Fracture patterns simulated using fine scale XFEM and MS-XFEM after final simulation step are compared in Fig. 6.17. The blue circles represent the crack pattern by fine scale XFEM and the red crosses represent the crack pattern by MS-XFEM. It is obvious that the crack path predicted by MS-XFEM is identical to the one from fine scale XFEM. The accurate displacements computation from MS-XFEM normally lead to correct predictions

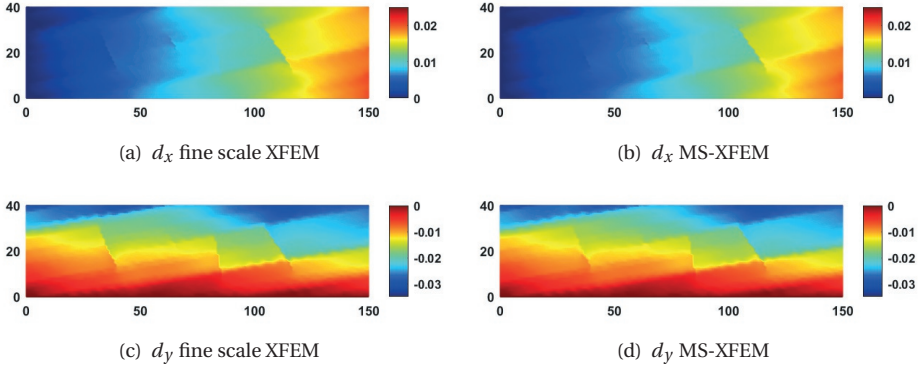


Figure 6.15: Test case 3: comparison between displacements solutions from fine scale XFEM and MS-XFEM. (a) and (c) represent displacements solutions from fine scale XFEM. (b) and (d) represent displacements solutions from MS-XFEM.

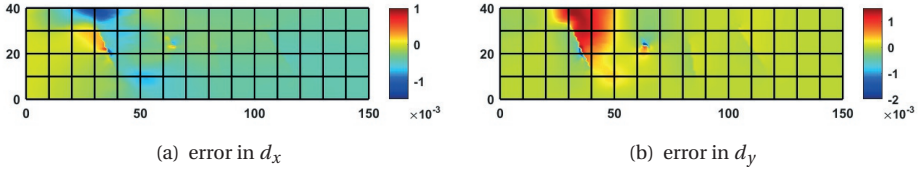


Figure 6.16: Test Case 3: Errors between displacements solutions from fine scale XFEM and MS-XFEM in (a)  $x$  direction and (b)  $y$  direction. Black lines depict the coarse scale mesh.

of fractures propagation paths. This means that MS-XFEM is capable of simulating induced sliding and propagation of heterogeneous subsurface formation.

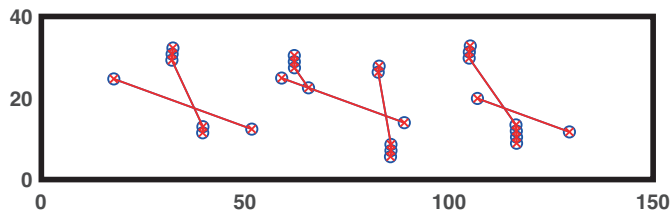


Figure 6.17: Test case 3: crack patterns simulated by fine scale XFEM (blue circle) and MS-XFEM (red cross) at time step 5.

The basis functions belonging to coarse mesh points [120, 10] and [120, 10] at step 1 and step 5 are plotted in Fig. 6.18. From Fig. 6.18 (a) and Fig. 6.18 (b), the growth of the fractures is nicely captured by the basis functions. This demonstrates that the construction and update of basis functions are successful.

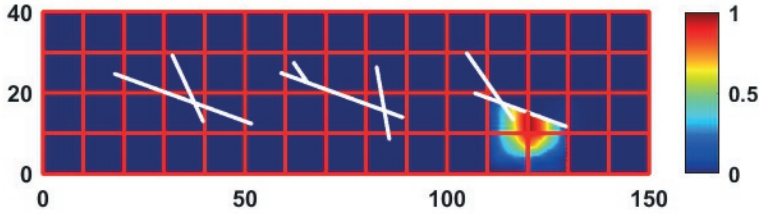
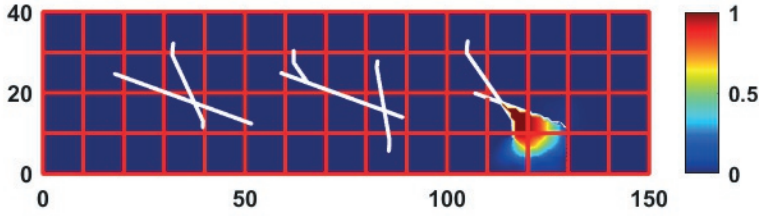
(a)  $P_{yy}$  at step 1(b)  $P_{yy}$  at step 5

Figure 6.18: Test case 3: Basis functions centered at the coarse mesh point  $[120, 10]$  at time steps 1 and 5. Notably, the updated basis functions accurately capture the growth of fracture.

## 6.4. CONCLUSION

In this chapter, the successful application of MS-XFEM to simulate fracture growth under compression in mixed mode is demonstrated. The utilization of the weighted spatial average method, introduced in Chapter 2, ensures the simulation of smooth crack propagation paths. This is proved in the first test case by comparing the numerical crack paths generated by fine-scale XFEM and experimental images. Furthermore, when employing MS-XFEM with preconditioned GMRES, the accuracy of wing crack path simulation closely matches that of fine-scale XFEM. The second test case and final test case show MS-XFEM's capability to simulate the propagation of multiple cracks in mixed mode under compression. The basis functions exhibit outstanding performance in capturing the extension of fractures and the formation of new cross discontinuities. In the final test case, MS-XFEM also shows its capability to simulate heterogeneous formation. These results underscore the significant potential of MS-XFEM for real-world applications, such as simulating hydraulic fracture propagation or induced fractures propagation, where accurate and efficient modeling is crucial.



# 7

## CONCLUDING REMARKS AND FUTURE PERSPECTIVES

Simulation of underground fractured formations is crucial for current worldwide energy supplies including traditional oil and gas energy and the new sustainable applications of environmental protection and energy storage. In this thesis, the multiscale extended finite element method (MS-XFEM) is developed to provide efficient and accurate simulation results. The ultimate goal of using this MS-XFEM is to ensure that it can assist in simulating the contact-frictional behavior of fractures under external compressive loading and fractures propagation due to mixed-mode loading. The whole project is performed in two main stages of developing MS-XFEM for the simulation of fractures under tensile loading and under compressive loading, which are described in the following subsections.

### 7.1. MS-XFEM FOR THE SIMULATION OF FRACTURES UNDER TENSILE LOADING

The primary objective of integrating multiscale methods with XFEM is to ensure the incorporation of all fractures or discontinuities within the basis functions. This guarantees the accurate preservation of these discontinuities in the final fine-scale solutions, which are interpolated from the coarse-scale solutions. Additionally, this approach offers the advantage of eliminating the need for extra degrees of freedom (DOFs) within the coarse-scale system, effectively transforming it into a simplified FEM system. This reduction in DOFs significantly reduces the size of the matrix system, enhancing computational efficiency.

Chapter 3 introduces a novel approach to constructing basis functions for MS-XFEM, known as the local solving method. This method involves computing local XFEM problems within each individual coarse element. In this process, the values of basis functions along the coarse element's boundary are determined by initially solving the re-

duced equilibrium equations. In 2D, to approximate this reduced equilibrium equation, a 1D bar model is employed. If the coarse element boundary is fractured, a 1D XFEM model is solved; otherwise, a 1D FEM model is used. These boundary values are then used as boundary conditions to calculate the values of basis functions within the coarse element.

This construction process can be executed algebraically, directly operating on the fine-scale stiffness matrix, making it a more convenient alternative to the local solving method. In Chapter 4, when applying MS-XFEM to simulate fracture propagation, basis functions can be updated locally. As fractures propagate on the fine-scale level, basis functions associated with the coarse-scale elements, where fracture tips propagate are recomputed and updated. Consequently, a new MS-XFEM displacement solution is computed based on these updated basis functions.

To reduce both high-frequency and low-frequency errors to a desired level, an iterative strategy has been employed. One commonly adopted approach is the two-stage iterative method, comprising a first stage utilizing of the multiscale solver and a second stage applying of the fine-scale smoother  $ILLU(0)$ . Alternatively, an iterative method has been found to be highly effective in reducing high-frequency errors, especially in complex fractured domains. These strategies have demonstrated their efficacy in enhancing the accuracy and convergence of the MS-XFEM methodology, making it a robust tool for simulating fracture propagation in heterogeneous geological formations.

The proposed MS-XFEM method has demonstrated its accuracy and efficiency across various test cases presented in Chapter 3. The MS-XFEM solutions, enhanced by the two-stage iterative method, exhibit close agreement with fine-scale XFEM solutions. Additionally, MS-XFEM has proven its accuracy in handling heterogeneous domains with multiple fractures. The algebraic approach for constructing basis functions has been a success, effectively capturing multiple discontinuities within a single coarse mesh element.

In scalability tests, the experiments with varying numbers of fractures have proved that MS-XFEM is not affected by the number of extra DOFs, highlighting a key advantage of this methodology. While the computational cost of MS-XFEM has not been quantified in terms of CPU time due to its implementation on a non-C++ platform, an operator-based analysis has been employed to assess the cost-efficiency ratio of MS-XFEM relative to fine-scale XFEM. The results of this analysis illustrate that MS-XFEM excels in efficiency, particularly when the number of grids is too large.

MS-XFEM has proven its capability to effectively simulate fracture propagation, provided that the basis functions undergo proper updates. This update process involves the recomputation of local basis functions associated with coarse elements where changes in fracture geometries occur, which are then reassembled into the global basis functions matrix denoted as  $P$ . The utilization of preconditioned GMRES for smoothing out high-frequency errors within the final displacement field ensures the accurate simulation of fracture propagation paths. Chapter 4, in particular, focuses on simulating fracture propagation under tensile stress, with both test cases demonstrating the remarkable accuracy of MS-XFEM in predicting fracture propagation paths when compared to those computed by fine-scale XFEM. The success of these simulations can be attributed to the precise basis function updates, as evidenced in the results presented in Chapter 4.

## 7.2. MS-XFEM FOR THE SIMULATION OF FRACTURES UNDER COMPRESSIVE LOADING

The MS-XFEM is further developed to enable the simulation of fractured formations under compressive loading, a common loading condition in subsurface fractured formations. In contrast to fractures under tensile stress, fractures subjected to compression exhibit contact forces along their surfaces. To prevent penetration between the two sides of fractures, the penalty method is employed at the fine-scale level, as elaborated in Chapter 5. In the penalty method, an artificial high stiffness is introduced to each fractured element, effectively averting penetration between fracture surfaces. Additionally, the slip conditions at fracture interfaces are governed by Coulomb's law. Therefore, when combining the penalty method with XFEM, an auxiliary contact matrix is incorporated into the fine-scale stiffness matrix. This contact matrix is iteratively updated in response to changes in stick-slip conditions across all Gauss points along the fractures.

As for the simulation of contact-frictional behavior using MS-XFEM, the basis functions construction strategy is the same as applied in Chapter 3. The stiffness matrix without contact matrix is used to construct the basis functions in order to avoid unnecessary computational cost as explained in Chapter 5.

The effectiveness of MS-XFEM in simulating the deformation field of fractured formations under compression is well-demonstrated through the test cases in Chapter 5. Being an embedded method, the sensitivity of the slip profile to mesh resolution is evident, as demonstrated in the first test case in Chapter 5. It highlights that finer mesh resolutions yield results closer to the analytical solution. At a given mesh resolution, MS-XFEM demonstrates its capability to closely simulate the slip profile compared to fine-scale XFEM, indicating its accuracy in modeling contact-frictional behavior. Notably, in the completely cracked test case, MS-XFEM proves to be accurate even without the application of preconditioned GMRES. This underscores the success in constructing basis functions that effectively capture contact-frictional behavior along fractures. The final test case in Chapter 5 showcases MS-XFEM's ability to simulate the contact behaviors of multiple fractures within a single domain under compression, with the basis functions, much like in Chapter 3, adeptly capturing multiple discontinuities.

The thesis attains its objective in Chapter 6, where the application of MS-XFEM for simulating crack propagation under compression is expounded. Wing cracks emerge in response to local tensile stress occurrences around fracture tips, often due to kink propagation induced by slip along fracture surfaces. However, the conventional application of maximum principle stress theory utilizing Stress Intensity Factors (SIFs) encounters challenges in this simulation, especially as Mode II SIFs exhibit oscillations during the fracture tip propagation process. In Chapter 6, the direction of propagation is determined by a weighted spatial averaged stress vector based on Gauss points in the finite elements near the fracture tips. Nevertheless, this direction computation still relies on Maximum Principle Stress Theory. The test case presented in Chapter 6 verifies the accuracy of MS-XFEM in simulating wing crack propagation by comparing results to images obtained from experimental studies. Furthermore, Chapter 6 demonstrates the precision of MS-XFEM in simulating the propagation of multiple wing cracks.

### 7.3. FUTURE PERSPECTIVES

While this thesis has introduced an efficient and accurate method for addressing complex subsurface fractured formations, there remain several important aspects that require further investigation. These avenues for future research are essential to enhance the comprehensiveness and applicability of the proposed methodology.

Further validation efforts are imperative to enhance both the fine-scale XFEM simulator and the MS-XFEM framework. While the fine-scale XFEM simulator in this thesis yields high-quality displacement solutions, challenges persist in areas such as slip profile generation. Certain issues within the fine-scale XFEM framework have not been fully resolved in this PhD research. A recommended future improvement involves the application of higher-order shape functions to mitigate oscillations in slip profiles along the discontinuity interface. These enhancements are anticipated to positively impact the quality of MS-XFEM solutions, given the framework's reliance on constructing a fine-scale stiffness matrix. Regarding the MS-XFEM framework, additional validation work is required to further establish its accuracy in simulating deformation and fractures propagation within fractured subsurface formations.

The implementation of adaptive multi-level mesh simulations constitutes a pivotal advancement within the context of MS-XFEM. Extensive research efforts have already explored the domain of adaptive multi-level mesh simulations [68, 69, 93, 104, 105]. This imperative step serves as a prerequisite for the practical application of MS-XFEM in real-field scenarios, such as enhanced geothermal systems (EGS) and carbon capture and storage (CCS). In the simulation of fractured subsurface formations, the focus often centers on the stress field around fracture tips or slip profiles along fracture surfaces, rather than the stress distribution or displacement fields in fracture-free zones. This underscores the suitability of adaptive multi-level simulations, where finer-scale grids are judiciously applied to regions encompassing propagating fracture tips and fracture intersection points. Conversely, coarser-scale grids suffice for areas devoid of fractures. However, the determination of an optimal coarsening ratio for the first level coarse-scale grids requires comprehensive research. Based on the MS-XFEM framework proposed in this thesis, it is anticipated that all coarser-level scale systems restricted from the first level coarse-scale system are finite element systems. Fracture related information resides only within the basis functions mapping the first level coarse-scale mesh to the fine-scale grids. Chapter 3 results illuminate that different coarsening ratios yield varying levels of accuracy, underscoring the significance of selecting the most optimized coarsening ratio for the first level coarse-scale grids.

Besides the incorporation of adaptive multi-level mesh simulation, there are two other crucial aspects essential for practical applications of MS-XFEM method real-world scenarios. The first one is its extension into three-dimensional (3D) domains. Progress in adapting this methodology to 3D contexts is evident from prior research contributions [106, 107]. However, a formidable challenge presents itself in the extension of discontinuities into four-dimensional basis functions. In a 3D domain, these basis functions are functions of  $(x, y, z)$  coordinates, thus necessitating a four-dimensional representation. The integration of 2D fracture planes into these four-dimensional basis functions remains a significant and complex challenge. The second aspect pertains to the integra-

tion of plastic deformation modeling within the MS-XFEM framework, an area that has been explored in recent research efforts [108–110]. It is noteworthy that the present thesis work is grounded in the assumption of a linear elastic constitutive law, which does not align with the material behavior observed in actual subsurface formations. To enhance the practical applicability of MS-XFEM in real-world subsurface applications, further in-depth research and investigation are imperative in this specific domain.

MS-XFEM is capable of simulating the entire global domain of interest, yet it is particularly optimized for application within specific local fractured zones of interest. Within fractured formations, not all fractures hold equal importance. For instance, the propagation of a single micro-fracture within a massive subsurface formation spanning 4 to 5 orders of magnitude in length may have a limited impact on the entire domain. Therefore, an effective strategy involves initially identifying those significant large-scale yet localized zones where peak stresses emerge, such as around major fault lines or within densely interconnected fracture networks. Subsequently, the application of MS-XFEM to simulate these specific zones proves highly efficient. MS-XFEM delivers precise deformation and propagation results, facilitating a deeper comprehension of the behaviors exhibited within the broader context of fractured formations.

Finally, migration of the current MS-XFEM code base onto a C++ platform is necessary for its future development. This transition not only aligns with industry standards but also harnesses the computational efficiency intrinsic to C++. Furthermore, the utilization of parallel computing resources is paramount. A comprehensive evaluation of MS-XFEM's efficiency through real-time CPU performance analysis is indispensable, given the current limitations of MATLAB-based codes in this context. To accommodate the simulation of extensive-scale models essential for real-world applications, parallel computing on clusters emerges as an absolute necessity. This momentous stride is pivotal for the seamless integration of MS-XFEM into authentic field research scenarios.



## REFERENCES

- [1] IEA, “Key world energy statistics 2021.” <https://www.iea.org/reports/key-world-energy-statistics-2021>, 2021.
- [2] L. Hashemi, M. Blunt, and H. Hajibeygi, “Pore-scale modelling and sensitivity analyses of hydrogen-brine multiphase flow in geological porous media,” *Scientific reports*, vol. 11, no. 1, p. 8348, 2021.
- [3] L. Hashemi, M. Boon, W. Glerum, R. Farajzadeh, and H. Hajibeygi, “A comparative study for h [formula omitted]–ch [formula omitted] mixture wettability in sandstone porous rocks relevant to underground hydrogen storage,” 2022.
- [4] M. Boon and H. Hajibeygi, “Experimental characterization of h<sub>2</sub>/water multiphase flow in heterogeneous sandstone rock at the core scale relevant for underground hydrogen storage (uhs),” *Scientific reports*, vol. 12, no. 1, p. 14604, 2022.
- [5] Z. Bo, M. Boon, H. Hajibeygi, and S. Hurter, “Impact of experimentally measured relative permeability hysteresis on reservoir-scale performance of underground hydrogen storage (uhs),” *international journal of hydrogen energy*, vol. 48, no. 36, pp. 13527–13542, 2023.
- [6] W. van Rooijen, L. Hashemi, M. Boon, R. Farajzadeh, and H. Hajibeygi, “Microfluidics-based analysis of dynamic contact angles relevant for underground hydrogen storage,” *Advances in Water Resources*, vol. 164, p. 104221, 2022.
- [7] K. R. Kumar, H. T. Honorio, and H. Hajibeygi, “Simulation of the inelastic deformation of porous reservoirs under cyclic loading relevant for underground hydrogen storage,” *Scientific Reports*, vol. 12, no. 1, p. 21404, 2022.
- [8] Y. Wang, C. Vuik, and H. Hajibeygi, “Co<sub>2</sub> storage in deep saline aquifers: Impacts of fractures on hydrodynamic trapping,” *International Journal of Greenhouse Gas Control*, vol. 113, p. 103552, 2022.
- [9] M. Zhao, Y. Wang, M. Gerritsma, and H. Hajibeygi, “Efficient simulation of co<sub>2</sub> migration dynamics in deep saline aquifers using a multi-task deep learning technique with consistency,” *Advances in Water Resources*, p. 104494, 2023.
- [10] Z. Zhang, Y. Wang, C. Vuik, and H. Hajibeygi, “An efficient simulation approach for long-term assessment of co<sub>2</sub> storage in complex geological formations,” in *SPE Reservoir Characterisation and Simulation Conference and Exhibition*, OnePetro, 2023.

- [11] S. Krevor, H. De Coninck, S. E. Gasda, N. S. Ghaleigh, V. de Gooyert, H. Hajibeygi, R. Juanes, J. Neufeld, J. J. Roberts, and F. Swennenhuis, “Subsurface carbon dioxide and hydrogen storage for a sustainable energy future,” *Nature Reviews Earth & Environment*, vol. 4, no. 2, pp. 102–118, 2023.
- [12] S. Zendejboudi and A. Bahadori, *Shale oil and gas handbook: theory, technologies, and challenges*. Gulf Professional Publishing, 2016.
- [13] J. E. Olson, “Joint pattern development: Effects of subcritical crack growth and mechanical crack interaction,” *Journal of Geophysical Research: Solid Earth*, vol. 98, no. B7, pp. 12251–12265, 1993.
- [14] J. E. Olson, “Predicting fracture swarms—the influence of subcritical crack growth and the crack-tip process zone on joint spacing in rock,” *Geological Society, London, Special Publications*, vol. 231, no. 1, pp. 73–88, 2004.
- [15] J. Olson, “Fracture aperture, length and pattern geometry development under biaxial loading: a numerical study with applications to natural, cross-jointed systems,” *Geological Society, London, Special Publications*, vol. 289, no. 1, pp. 123–142, 2007.
- [16] E. L. Majer, R. Baria, M. Stark, S. Oates, J. Bommer, B. Smith, and H. Asanuma, “Induced seismicity associated with enhanced geothermal systems,” *Geothermics*, vol. 36, no. 3, pp. 185–222, 2007.
- [17] T. Postma and J.-D. Jansen, “The small effect of poroelastic pressure transients on triggering of production-induced earthquakes in the groningen natural gas field,” *Journal of Geophysical Research: Solid Earth*, vol. 123, pp. 401–417, jan 2018.
- [18] S. Krevor, H. de Coninck, S. Gasda, N. S. Ghaleigh, V. de Gooyert, H. Hajibeygi, R. Juanes, J. Neufeld, J. Roberts, and F. Swennenhuis, “Algebraic dynamic multi-level method for compositional flow in heterogeneous porous media,” *Nature Reviews Earth & Environment*, vol. 4, pp. 102–118, 2023.
- [19] F. of the Earth, “Groningen earthquakes: don’t live near gas well, warn locals.” [Photograph], 1997.
- [20] G. Allaire, “Homogenization and two-scale convergence,” *SIAM Journal on Mathematical Analysis*, vol. 23, no. 6, pp. 1482–1518, 1992.
- [21] A. Abdulle and E. Weinan, “Finite difference heterogeneous multi-scale method for homogenization problems,” *Journal of Computational Physics*, vol. 191, no. 1, pp. 18–39, 2003.
- [22] Y. Amanbek, G. Singh, M. F. Wheeler, and H. van Duijn, “Adaptive numerical homogenization for upscaling single phase flow and transport,” *Journal of Computational Physics*, vol. 387, pp. 117–133, 2019.
- [23] U. Hornung, *Homogenization and Porous Media*, vol. 6. Springer Science & Business Media, 1997.

- [24] K. Kumar, T. van Noorden, and I. S. Pop, "Upscaling of reactive flows in domains with moving oscillating boundaries," *Discrete Contin. Dyn. Sys. Ser. S*, vol. 7, pp. 95–111, 2014.
- [25] H.-W. Zhang, J.-K. Wu, J. Lü, and Z.-D. Fu, "Extended multiscale finite element method for mechanical analysis of heterogeneous materials," *Acta mechanica sinica*, vol. 26, no. 6, pp. 899–920, 2010.
- [26] A. Khoei and M. Hajiabadi, "Fully coupled hydromechanical multiscale model with microdynamic effects," *International Journal for Numerical Methods in Engineering*, vol. 115, no. 3, pp. 293–327, 2018.
- [27] R. Patil, B. Mishra, and I. V. Singh, "A new multiscale xfm for the elastic properties evaluation of heterogeneous materials," *International Journal of Mechanical Sciences*, vol. 122, pp. 277–287, 2017.
- [28] H. Hajibeygi, G. Bonfigli, M. A. Hesse, and P. Jenny, "Iterative multiscale finite-volume method," *Journal of Computational Physics*, vol. 227, no. 19, pp. 8604–8621, 2008.
- [29] H. Hajibeygi and P. Jenny, "Multiscale finite-volume method for parabolic problems arising from compressible multiphase flow in porous media," *Journal of Computational Physics*, vol. 228, no. 14, pp. 5129–5147, 2009.
- [30] H. Hajibeygi, M. B. Olivares, M. HosseiniMehr, S. Pop, and M. Wheeler, "A benchmark study of the multiscale and homogenization methods for fully implicit multiphase flow simulations," *Advances in Water Resources*, vol. 143, p. 103674, 2020.
- [31] N. Castelletto, H. Hajibeygi, and H. A. Tchelepi, "Multiscale finite-element method for linear elastic geomechanics," *Journal of Computational Physics*, vol. 331, pp. 337–356, 2017.
- [32] P. Jenny, S. Lee, and H. A. Tchelepi, "Multi-scale finite-volume method for elliptic problems in subsurface flow simulation," *Journal of computational physics*, vol. 187, no. 1, pp. 47–67, 2003.
- [33] M. Cusini, R. Gielisse, H. Groot, C. van Kruijsdijk, and H. Hajibeygi, "Incomplete mixing in porous media: Todd-longstaff upscaling approach versus a dynamic local grid refinement method," *Computational Geosciences*, vol. 23, pp. 373–397, 2019.
- [34] M. Tene, Y. Wang, and H. Hajibeygi, "Adaptive algebraic multiscale solver for compressible flow in heterogeneous porous media," *J. Comp. Phys.*, vol. 300, pp. 679–694, 2015.
- [35] K. R. Kumar and H. Hajibeygi, "Multiscale simulation of inelastic creep deformation for geological rocks," *Journal of Computational Physics*, vol. 440, p. 110439, 2021.

- [36] M. R. Hajiabadi and A. R. Khoei, "A bridge between dual porosity and multiscale models of heterogeneous deformable porous media," *International Journal for Numerical and Analytical Methods in Geomechanics*, vol. 43, no. 1, pp. 212–238, 2019.
- [37] K. Bisdom, B. Gauthier, G. Bertotti, and N. Hardebol, "Calibrating discrete fracture-network models with a carbonate three-dimensional outcrop fracture network: Implications for naturally fractured reservoir modeling," *AAPG bulletin*, vol. 98, no. 7, pp. 1351–1376, 2014.
- [38] M. Rashid, "The arbitrary local mesh replacement method: an alternative to remeshing for crack propagation analysis," *Computer Methods in Applied Mechanics and Engineering*, vol. 154, no. 1-2, pp. 133–150, 1998.
- [39] T. N. Bittencourt, P. A. Wawrzynek, A. R. Ingraffea, and J. Sousa, "Quasi-automatic simulation of crack propagation for 2d lefm problems," *Engineering Fracture Mechanics*, vol. 55, no. 2, pp. 321–334, 1996.
- [40] J. Jiang and R. M. Younis, "Hybrid coupled discrete-fracture/matrix and multicontinuum models for unconventional-reservoir simulation," *SPEJ*, vol. 21, pp. 1009–1027, 2016.
- [41] T. T. Garipov, P. Tomin, R. Rin, D. V. Voskov, and H. A. Tchelepi, "Unified thermo-compositional-mechanical framework for reservoir simulation," *Computational Geosciences*, vol. 22, no. 4, pp. 1039–1057, 2018.
- [42] Y. Wang and M. Shahvali, "Discrete fracture modeling using centroidal voronoi grid for simulation of shale gas plays with coupled nonlinear physics," *Fuel*, vol. 163, pp. 65–73, jan 2016.
- [43] A. Novikov, D. Voskov, M. Khait, H. Hajibeygi, and J. D. Jansen, "A scalable collocated finite volume scheme for simulation of induced fault slip," *Journal of Computational Physics*, vol. 469, p. 111598, 2022.
- [44] H. Dang-Trung, E. Keilegavlen, and I. Berre, "Numerical modeling of wing crack propagation accounting for fracture contact mechanics," *International Journal of Solids and Structures*, vol. 204, pp. 233–247, 2020.
- [45] K. Rege and H. Lemu, "A review of fatigue crack propagation modelling techniques using fem and xfem," in *IOP Conference Series: Materials Science and Engineering*, vol. 276, p. 012027, IOP Publishing, 2017.
- [46] H. Azadi and A. Khoei, "Numerical simulation of multiple crack growth in brittle materials with adaptive remeshing," *International journal for numerical methods in engineering*, vol. 85, no. 8, pp. 1017–1048, 2011.
- [47] H. Hajibeygi, D. Karvounis, and P. Jenny, "A hierarchical fracture model for the iterative multiscale finite volume method," *J. Comput. Phys.*, vol. 230, pp. 8729–8743, 2011.

- [48] S. Shah, O. Møyner, M. Tene, K.-A. Lie, and H. Hajibeygi, “The multiscale restriction smoothed basis method for fractured porous media (f-mrsrb),” *Journal of Computational Physics*, vol. 318, pp. 36–57, 2016.
- [49] T. Praditia, R. Helmig, and H. Hajibeygi, “Multiscale formulation for coupled flow-heat equations arising from single-phase flow in fractured geothermal reservoirs,” *Computational Geosciences*, vol. 22, no. 5, pp. 1305–1322, 2018.
- [50] M. Tene, S. B. Bosma, M. S. A. Kobaisi, and H. Hajibeygi, “Projection-based embedded discrete fracture model (pEDFM),” *Advances in Water Resources*, vol. 105, pp. 205–216, jul 2017.
- [51] Y. Efendiev, J. Galvis, G. Li, and M. Presho, “Generalized multiscale finite element methods. oversampling strategies,” *International Journal for Multiscale Computational Engineering*, vol. 12, no. 6, pp. 465–484, 2014.
- [52] J. Y. Wu and F. Li, “An improved stable XFEM (is-XFEM) with a novel enrichment function for the computational modeling of cohesive cracks,” *Computer Methods in Applied Mechanics and Engineering*, vol. 295, pp. 77–107, oct 2015.
- [53] I. Sokolova, M. G. Bastisya, and H. Hajibeygi, “Multiscale finite volume method for finite-volume-based simulation of poroelasticity,” *Journal of Computational Physics*, vol. 379, pp. 309–324, 2019.
- [54] S. S. Behbahani, H. Hajibeygi, D. Voskov, and J. D. Jansen, “Smoothed embedded finite-volume method (sefvm) for modeling contact mechanics in deformable faulted and fractured porous media,” *Journal of Computational Physics*, vol. 459, p. 111143, 2022.
- [55] M. Cusini, A. A. Lukyanov, J. Natvig, and H. Hajibeygi, “Constrained pressure residual multiscale (cpr-ms) method for fully implicit simulation of multiphase flow in porous media,” *Journal of Computational Physics*, vol. 299, pp. 472–486, 2015.
- [56] J. Melenk and I. Babuška, “The partition of unity finite element method: Basic theory and applications,” *Computer Methods in Applied Mechanics and Engineering*, vol. 139, no. 1, pp. 289 – 314, 1996.
- [57] I. Babuška and J. M. Melenk, “The partition of unity method,” *International journal for numerical methods in engineering*, vol. 40, no. 4, pp. 727–758, 1997.
- [58] T. Belytschko and T. Black, “Elastic crack growth in finite elements with minimal remeshing,” *International Journal for Numerical Methods in Engineering*, vol. 45, no. 5, pp. 601–620, 1999.
- [59] N. Moes, J. Dolbow, and T. Belytschko, “A finite element method for crack growth without remeshing,” *International Journal for Numerical Methods in Engineering*, vol. 46, pp. 131–150, sep 1999.

- [60] A. M. Aragón and A. Simone, “The discontinuity-enriched finite element method,” *International Journal for Numerical Methods in Engineering*, vol. 112, pp. 1589–1613, sep 2017.
- [61] F. P. Meer and L. J. Sluys, “A phantom node formulation with mixed mode cohesive law for splitting in laminates,” *International Journal of Fracture*, vol. 158, pp. 107–124, may 2009.
- [62] G. N. Wells and L. Sluys, “A new method for modelling cohesive cracks using finite elements,” *International Journal for numerical methods in engineering*, vol. 50, no. 12, pp. 2667–2682, 2001.
- [63] K. Amir R, *Extended Finite Element Method: Theory and Applications*. John Wiley & Sons, Incorporated, Feb. 2015.
- [64] A. R. Khoei, *Extended finite element method: theory and applications*. John Wiley & Sons, 2014.
- [65] C. Daux, N. Moës, J. Dolbow, N. Sukumar, and T. Belytschko, “Arbitrary branched and intersecting cracks with the extended finite element method,” *International journal for numerical methods in engineering*, vol. 48, no. 12, pp. 1741–1760, 2000.
- [66] S. Osher and J. A. Sethian, “Fronts propagating with curvature-dependent speed: Algorithms based on hamilton-jacobi formulations,” *Journal of Computational Physics*, vol. 79, pp. 12–49, nov 1988.
- [67] M. Stolarska, D. L. Chopp, N. Moës, and T. Belytschko, “Modelling crack growth by level sets in the extended finite element method,” *International Journal for Numerical Methods in Engineering*, vol. 51, pp. 943–960, jul 2001.
- [68] M. HosseiniMehr, M. Cusini, C. Vuik, and H. Hajibeygi, “Algebraic dynamic multi-level method for embedded discrete fracture model (f-adm),” *Journal of Computational Physics*, vol. 373, pp. 324–345, 2018.
- [69] M. HosseiniMehr, C. Vuik, and H. Hajibeygi, “Adaptive dynamic multilevel simulation of fractured geothermal reservoirs,” *Journal of Computational Physics: X*, vol. 7, p. 100061, 2020.
- [70] Y. Wang, H. Hajibeygi, and H. A. Tchelepi, “Algebraic multiscale solver for flow in heterogeneous porous media,” *Journal of Computational Physics*, vol. 259, pp. 284–303, 2014.
- [71] R. Deb and P. Jenny, “Finite volume-based modeling of flow-induced shear failure along fracture manifolds,” *International Journal for Numerical and Analytical Methods in Geomechanics*, vol. 41, pp. 1922–1942, jul 2017.
- [72] G. Ren, J. Jiang, and R. M. Younis, “A fully coupled xfem-edfm model for multiphase flow and geomechanics in fractured tight gas reservoirs,” *Procedia Computer Science*, vol. 80, pp. 1404–1415, 2016.

- [73] A. Fumagalli and A. Scotti, "An efficient xfem approximation of darcy flows in arbitrarily fractured porous media," *Oil & Gas Science and Technology—Revue d'IFP Energies nouvelles*, vol. 69, no. 4, pp. 555–564, 2014.
- [74] B. Giovanardi, L. Formaggia, A. Scotti, and P. Zunino, "Unfitted fem for modelling the interaction of multiple fractures in a poroelastic medium," pp. 331–352, 2017.
- [75] E. T. Chung, Y. Efendiev, and G. Li, "An adaptive gmsfem for high-contrast flow problems," *Journal of Computational Physics*, vol. 273, pp. 54–76, 2014.
- [76] H. Zhou and H. A. Tchelepi, "Two-stage algebraic multiscale linear solver for highly heterogeneous reservoir models," *SPE Journal*, vol. 17, no. 02, pp. 523–539, 2012.
- [77] S. Loehnert and T. Belytschko, "A multiscale projection method for macro/microcrack simulations," *International Journal for Numerical Methods in Engineering*, vol. 71, no. 12, pp. 1466–1482, 2007.
- [78] M. Holl, S. Loehnert, and P. Wriggers, "An adaptive multiscale method for crack propagation and crack coalescence," *International Journal for Numerical Methods in Engineering*, vol. 93, no. 1, pp. 23–51, 2013.
- [79] Y. Saad and M. H. Schultz, "GMRES: A Generalized Minimal Residual Algorithm for Solving Nonsymmetric Linear Systems," *SIAM J. Sci. Stat. Comput.*, vol. 7, no. 3, pp. 856–869, 1986.
- [80] E. Chow and Y. Saad, "Experimental study of ilu preconditioners for indefinite matrices," *Journal of computational and applied mathematics*, vol. 86, no. 2, pp. 387–414, 1997.
- [81] R. D. Cook *et al.*, *Concepts and applications of finite element analysis*. John Wiley & sons, 2007.
- [82] G. Zi and T. Belytschko, "New crack-tip elements for xfem and applications to cohesive cracks," *International Journal for Numerical Methods in Engineering*, vol. 57, no. 15, pp. 2221–2240, 2003.
- [83] A. A. Griffith, "VI. the phenomena of rupture and flow in solids," *Philosophical Transactions of the Royal Society of London. Series A, Containing Papers of a Mathematical or Physical Character*, vol. 221, pp. 163–198, jan 1921.
- [84] X.-Z. Suo and A. Combescure, "Double virtual crack extension method for crack growth stability assessment," *International journal of fracture*, vol. 57, no. 2, pp. 127–150, 1992.
- [85] É. Budyn, G. Zi, N. Moës, and T. Belytschko, "A method for multiple crack growth in brittle materials without remeshing," *International Journal for Numerical Methods in Engineering*, vol. 61, pp. 1741–1770, sep 2004.

- [86] P. Wriggers and T. A. Laursen, *Computational contact mechanics*, vol. 2. Springer, 2006.
- [87] F. Liu and R. I. Borja, “A contact algorithm for frictional crack propagation with the extended finite element method,” *International Journal for Numerical methods in engineering*, vol. 76, no. 10, pp. 1489–1512, 2008.
- [88] F. Xu, H. Hajibeygi, and L. J. Sluys, “Multiscale extended finite element method for deformable fractured porous media,” *Journal of Computational Physics*, vol. 436, p. 110287, 2021.
- [89] R. J. de Moraes, J. R. Rodrigues, H. Hajibeygi, and J. D. Jansen, “Multiscale gradient computation for flow in heterogeneous porous media,” *Journal of Computational Physics*, vol. 336, pp. 644–663, 2017.
- [90] I. Sneddon, “Fourier transforms. courier corporation,” 1995.
- [91] F. Xu, H. Hajibeygi, and L. J. Sluys, “Adaptive multiscale extended finite element method (ms-xfem) for the simulation of multiple fractures propagation in geological formations,” *Journal of Computational Physics*, vol. 486, p. 112114, 2023.
- [92] H. Hajibeygi and P. Jenny, “Adaptive iterative multiscale finite volume method,” *Journal of Computational Physics*, vol. 230, no. 3, pp. 628–643, 2011.
- [93] M. Cusini, B. Fryer, C. van Kruijsdijk, and H. Hajibeygi, “Algebraic dynamic multi-level method for compositional flow in heterogeneous porous media,” *Journal of Computational Physics*, vol. 354, pp. 593–612, feb 2018.
- [94] D. Huang, B. Li, W. Ma, D. Cen, and Y. Song, “Effects of bedding planes on fracture behavior of sandstone under semi-circular bending test,” *Theoretical and Applied Fracture Mechanics*, vol. 108, p. 102625, aug 2020.
- [95] P. Senseny and T. Pfeifle, *Fracture toughness of sandstones and shales*. 1984.
- [96] H. Tada, P. C. Paris, and G. R. Irwin, “The stress analysis of cracks,” *Handbook, Del Research Corporation*, vol. 34, no. 1973, 1973.
- [97] T. Pin and T. H. Pian, “On the convergence of the finite element method for problems with singularity,” *International Journal of Solids and Structures*, vol. 9, no. 3, pp. 313–321, 1973.
- [98] R. I. Borja, “Assumed enhanced strain and the extended finite element methods: A unification of concepts,” *Computer methods in applied mechanics and engineering*, vol. 197, no. 33-40, pp. 2789–2803, 2008.
- [99] A.-V. Phan, J. Napier, L. Gray, and T. Kaplan, “Symmetric-galerkin bem simulation of fracture with frictional contact,” *International journal for numerical methods in engineering*, vol. 57, no. 6, pp. 835–851, 2003.

- [100] L. Wang, C. Vuik, and H. Hajibeygi, "A stabilized mixed-fe scheme for frictional contact and shear failure analyses in deformable fractured media," *Engineering Fracture Mechanics*, vol. 267, p. 108427, 2022.
- [101] T. Garipov, M. Karimi-Fard, and H. Tchelepi, "Discrete fracture model for coupled flow and geomechanics," *Computational Geosciences*, vol. 20, pp. 149–160, 2016.
- [102] A. Saimoto and H. Nisitani, "Crack propagation criterion and simulation under biaxial loading," *WIT Transactions on Engineering Sciences*, vol. 37, 2002.
- [103] G. Zhang, M. Wang, X. Li, S. Yue, Z. Wen, and S. Han, "Micro- and macrocracking behaviors in granite and molded gypsum containing a single flaw," *Construction and Building Materials*, vol. 292, p. 123452, jul 2021.
- [104] M. Cusini, C. van Kruijsdijk, and H. Hajibeygi, "Algebraic dynamic multilevel (adm) method for fully implicit simulations of multiphase flow in porous media," *Journal of Computational Physics*, vol. 314, pp. 60–79, 2016.
- [105] M. Cusini, *Dynamic Multilevel Methods for Simulation of Multiphase Flow in Heterogeneous Porous Media*. PhD thesis, Delft University of Technology, 2019.
- [106] K. Agathos, E. Chatzi, and S. P. Bordas, "Stable 3d extended finite elements with higher order enrichment for accurate non planar fracture," *Computer Methods in Applied Mechanics and Engineering*, vol. 306, pp. 19–46, 2016.
- [107] K. Agathos, E. Chatzi, and S. P. Bordas, "Multiple crack detection in 3d using a stable xfem and global optimization," *Computational mechanics*, vol. 62, pp. 835–852, 2018.
- [108] K. Ramesh Kumar, A. Makhmutov, C. Spiers, and H. Hajibeygi, "Geomechanical simulation of energy storage in salt formations," *Scientific Reports*, vol. 11, pp. 1–24, 2021.
- [109] K. R. Kumar, H. Honorio, D. Chandra, M. Lesueur, and H. Hajibeygi, "Comprehensive review of geomechanics of underground hydrogen storage in depleted reservoirs and salt caverns," *Journal of Energy Storage*, vol. 73, p. 108912, 2023.
- [110] M. Naderloo, K. R. Kumar, E. Hernandez, H. Hajibeygi, and A. Barnhoorn, "Experimental and numerical investigation of sandstone deformation under cycling loading relevant for underground energy storage," *Journal of Energy Storage*, vol. 64, p. 107198, 2023.



# CURRICULUM VITÆ

## Fanxiang XU

May 26, 1994 Born in Sichuan, China.

### EDUCATION

- 2012 – 2016 BSc. Petroleum Engineering  
China University of Petroleum (Huadong), China  
University of Wyoming, the United States
- 2016 – 2018 MSc. Petroleum Engineering  
Delft University of Technology, the Netherlands
- 2018 – 2024 PhD. Faculty Of Civil Engineering and Geosciences  
Delft University of Technology, the Netherlands  
*Thesis:* Multiscale Extended Finite Element Method for the  
Simulation of Fractured Geological Formations  
*Promotor:* Prof. dr. ir. L. J. Sluys  
*Promotor:* Prof. dr. ir. H. Hajibeygi



# LIST OF PUBLICATIONS

The following is a listing of the journal publications and conference papers authored, along with the talks given during the PhD program, in reverse chronological order.

## JOURNAL PAPERS

**Xu, F.**, Hajibeygi, H., Sluys, L. J. (2024). *Multiscale Extended Finite Element Method (MS-XFEM) For Simulating Fractures Propagation in Mixed-mode Condition Under Compression*. [In preparation]

**Xu, F.**, Hajibeygi, H., Sluys, L. J. (2024). *Multiscale Extended Finite Element Method (MS-XFEM) Analysis of Deformation of Fractured Geological Formations under Compression*. [In preparation]

**Xu, F.**, Hajibeygi, H., Sluys, L. J. (2023). *Adaptive multiscale extended finite element method (MS-XFEM) for the simulation of multiple fractures propagation in geological formations*. [Journal of Computational Physics](#), 486, 112114.

**Xu, F.**, Hajibeygi, H., Sluys, L. J. (2021). *Multiscale extended finite element method for deformable fractured porous media*. [Journal of Computational Physics](#), 436, 110287.

## CONFERENCE PROCEEDINGS AND TALKS

**Xu, F.**, Hajibeygi, H., Sluys, B. (2022, September). *Multiscale Extended Finite Element Method for Modelling Mechanical Deformation in Porous Media with Propagating Fractures*. In [ECMOR 2022 \(Vol. 2022, No. 1, pp. 1-14\)](#). European Association of Geoscientists & Engineers.

**Xu, F.**, Hajibeygi, H., Sluys, B. (2020, September). *Multiscale Extended Finite Element Method for Deformable Fractured Media*. In [ECMOR XVII \(Vol. 2020, No. 1, pp. 1-12\)](#). European Association of Geoscientists & Engineers.





# About the author



Fanxiang Xu was born on May 26, 1994, in Jiangyou, China. He started his bachelor's studies in petroleum engineering at China University of Petroleum (Huadong) and successfully defended his bachelor thesis at the University of Wyoming in 2016. Driven by a passion for academia, Fanxiang pursued a master's degree program in petroleum engineering at Delft University of Technology, where he was accepted. Under the guidance of Prof. Hadi Hajibeygi, he completed his master's thesis and graduated with cum laude in 2018. In October 2018, he embarked

on his PhD journey at the Faculty of Civil Engineering and Geosciences at Delft University of Technology, supervised by Prof. Hadi Hajibeygi and Prof. Bert Sluys.

Beyond his passion for simulation and mathematics, Fanxiang, an avid football fan, cherished the vibrant atmosphere of European football. He frequently played football at the 'X' sports center on Friday nights and visited renowned team stadiums. Moreover, he seized the opportunity to explore many famous sights in Europe, expanding his understanding beyond the confines of history books.

